Università degli Studi di Padova

Dipartimento di Ingegneria Industriale DII

Corso di Laurea Magistrale in Ingegneria Aerospaziale

Numerical Simulation and Parametric Study of a Supersonic Compressor Cascade

Student:
Tommaso Piovesan

Supervisor:
Prof. Ernesto Benini

Co-supervisor:
Eng. Andrea Magrini

Academic year 2018/2019

Ringraziamenti

Questo elaborato di tesi si presenta come il naturale completamento del mio corso di studi magistrali e come il risultato delle competenze da me acquisite durante l'intero ciclo di studi universitari. Desidero pertanto ringraziare mio padre e mia madre per la fiducia, l'incoraggiamento e il supporto economico durante tutta la mia carriera universitaria. Ringrazio cordialmente il mio relatore, il Prof. Ernesto Benini, per la sua costante disponibilità e cortesia. Infine, desidero ringraziare l'Ing. Andrea Magrini per il suo fondamentale aiuto durante lo svolgimento di questa attività di tesi.

Contents

List of Figures

List of Tables

Sommario

Questo elaborato di tesi descrive lo studio parametrico preliminare di una schiera piana di compressore supersonico, denominata ARL-SL19. I dati sperimentali ottenuti in varie gallerie del vento supersoniche per la schiera studiata nel presente elaborato, utili alla validazione di metodi computazionali e solutori numerici per le turbomacchine, sono stati utilizzati per la validazione del modello numerico e lo studio di sensitività della griglia di calcolo. Le simulazioni sono state condotte su un dominio periodico 2D attorno a un singolo profilo, utilizzando il software commerciale ANSYS® Fluent. I principali modelli di turbolenza implementati nel software CFD sono stati impiegati per la validazione e lo studio di sensitività: il modello Spalart-Allmaras, il modello k-ε, nelle sue tre diverse formulazioni disponibili (STD, RNG e REALIZABLE) e il modello Shear Stress Transport (SST) k-ω. Lo studio parametrico della schiera supersonica è stato condotto analizzando l'influenza dei principali parametri fluidodinamici e geometrici, come il numero di Mach in ingresso, il rapporto di pressione statica e la solidità, sull'efficienza della schiera e sulle principali grandezze del flusso in uscita. I risultati ottenuti dallo studio parametrico possono essere utili al design di un compressore supersonico.

Abstract

The thesis describes a parametric study of a supersonic compressor cascade, known as ARL-SL19. The linear supersonic compressor cascade is the two-dimensional equivalent of the annular cascade of a supersonic compressor rotor. A series of experimental data, useful for validating computational methods and numerical solvers for turbomachines, were produced in several wind tunnel facilities and these benchmark data were employed for a preliminary validation and grid sensitivity analysis. A commercial CFD solver, ANSYS® Fluent, was employed for the numerical simulations. The most widely-used turbulence models available in ANSYS® Fluent were tested: the Spalart-Allmaras model, the k-ε model (STD, RNG, and REALIZABLE k-ε model), and the Shear Stress Transport (SST) k-ω model. A large number of two-dimensional simulations were carried out employing a computational domain consisting of a periodic grid around a single airfoil. The parametric study of the ARL-SL19 supersonic compressor cascade was carried out investigating the influence of the main flow variables (inlet Mach number and static pressure ratio) and geometric parameters (cascade solidity) on the overall performance and the exit flow quantities, in terms of mean exit flow angle and exit Mach number. The numerical results obtained from the parametric study can be useful for the design of supersonic compressor rotors.

Introduction

The development of modern aircraft fans and compressors aims to increase pressure ratios and to reduce weights at once. The advantages resulting from this design approach, which leads to a reduced number of stages and compactness, are a lower fuel consumption and an increased overall performance. To design compressors with increased pressure ratios and reduced number of stages, it is necessary to increase the flow velocity relative to the blades up to supersonic. In the modern civil and military aircraft engines, the fan and the first stage of the compressor are transonic. The most common categories of transonic axial compressors and fans are the single-stage fan in civil aero-engines, the multistage fan or low-pressure compressor in military combat engines, and the first stages of the multistage core engine compressors.

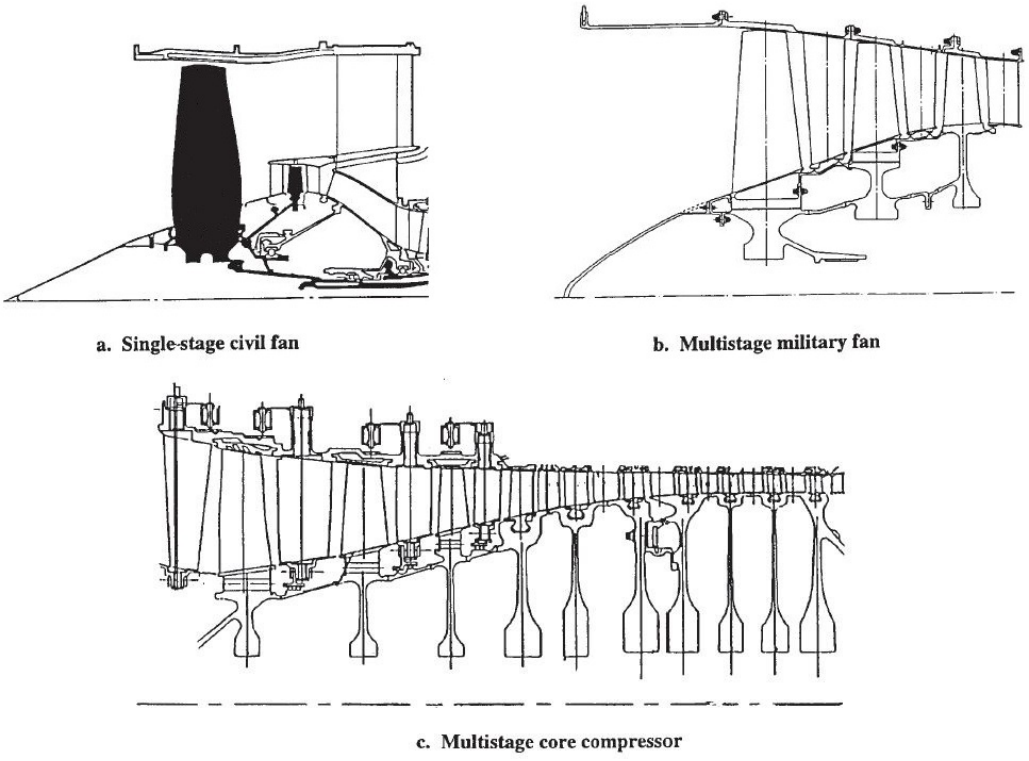

a. Single-stage civil fan

b. Multistage military fan

c. Multistage core compressor

Main types of transonic/supersonic fans and compressors for aircraft engines [3]

In these kinds of aeronautical compressors and fans, the inlet Mach number in the axial direction is subsonic, while the inlet Mach number relative to the rotor-tip section, because of the blade speed, can vary from 1.2 in multistage core compressors up to 1.7 in military combat aircraft compressors, with a value of about 1.5 in single-stage civil fans. At supersonic inlet conditions, compressor performance and efficiency depend on the shock waves in front of and inside the blade passage. In fact, in transonic and supersonic compressors, the static pressure is increased primarily by the shock waves inside the blade passage. However, the strength of the shock waves and their interaction with the boundary layer on the surfaces of the blades deeply influence the overall performance and the direction of the flow into the following stages. Hence, the design of fans and compressors, operating at supersonic inlet flow conditions, requires accurate knowledge of the flow behaviour inside the blade passage peculiar to these operating conditions.

The so-called linear supersonic compressor cascade is a fundamental experimental tool for gaining information about the wave pattern and the overall performance of a supersonic compressor. It consists of a two-dimensional array of a certain number of airfoils equivalent to the compressor blade section and mounted in a wind tunnel. Even if cascade models present clear physical limitations and significant differences compared with the corresponding rotor blade sections, they can provide excellent series of data sets for a large number of operating conditions, with less time and expense than would be necessary to test an entire compressor rotor. A large amount of detailed experimental results, obtained from compressor cascade models tested in supersonic cascade wind tunnel facilities, is available. These experimental data provide a thorough description of the cascade performance and the shock wave pattern and can be used as benchmark results to validate computational methods or for the assessment of numerical solvers for turbomachinery applications. In fact, numerical simulations are a fundamental tool to analyze transonic and supersonic flows in turbomachines and to perform parametric studies during the first steps of the design process.

The aim of the present work is to accurately simulate the supersonic flow in a supersonic compressor cascade and to carry out a parametric study for understanding the influence of the main flow variables and geometric parameters on the overall performance, which is useful for a preliminary design. The cascade, designated as ARL-SL19, was derived from a two-dimensional compressor rotor blade section and was tested in many wind tunnel facilities.

The presentation of the study on the ARL-SL19 cascade carried out hereunder is organized into six chapters. In the first two chapters, the fundamentals equations of compressible aerodynamics and the relations for shock waves are derived and discussed,

since they are the basis of the equations governing the flow in a supersonic cascade. The third chapter is concerned with a wide description of the operating condition peculiar of supersonic cascades, known as "unique incidence". The fundamental equations governing the flow in a supersonic cascade and the characteristic shock wave patterns are presented and widely discussed, along with a brief description of the most common airfoils shapes used for supersonic compressor blade sections. The fourth chapter briefly decribes the turbulence models implemented in the CFD solver and employed in the validation study and the grid sensitivity analysis. In the fifth chapter the validation of the numerical model and the grid sensitivity analysis, fundamental to the choice of the turbulence model and the grid size for the parametric study, are presented. The sixth chapter, which represents the core of this work, is concerned with the parametric study of the cascade, carried out analyzing the influence of the main flow and geometric variables on the overall cascade performance.

Chapter 1

Fundamental Equations of Compressible Aerodynamics

In this chapter, the fundamental equations of compressible aerodynamics are presented. The three fundamental equations (the *continuity equation*, the *momentum equation*, and the *energy equation*) are briefly derived and discussed for the most general case of a *viscous compressible fluid*, that is a fluid in which pressure variations produce significant and not negligible changes in fluid density. These equations are known as the *complete Navier-Stokes equations*. The fundamental equations are then simplified introducing the assumption of *incompressible fluid*. This simplified form of the fundamental equations leads to a less complex system of equations, useful for the subsequent discussions.
For more details, refer to [1], [11], and [21].

1.1 Continuity equation

Consider a fluid moving in streamlines, whose properties, for example density ρ, pressure p, and velocity $\overline{V}$, are functions of both position $\overline{r}$ and time t

$$\rho = \rho(\overline{r}, t) \qquad p = p(\overline{r}, t) \qquad \overline{V} = \overline{V}(\overline{r}, t)$$

For the sake of simplicity, neglect the explicit dependence of these quantities from $\overline{r}$ and t. Consider a fixed in space and non-deformable control volume V surrounded by a closed control surface S, with the fluid moving through it. Let $\overline{n}$ be the unit vector normal to the surface. By convention, $\overline{n}$ is positive when it is oriented outward from the control volume. Let dS and dV denote an infinitesimal area element of the control surface S and an infinitesimal volume element of the control volume V, respectively.

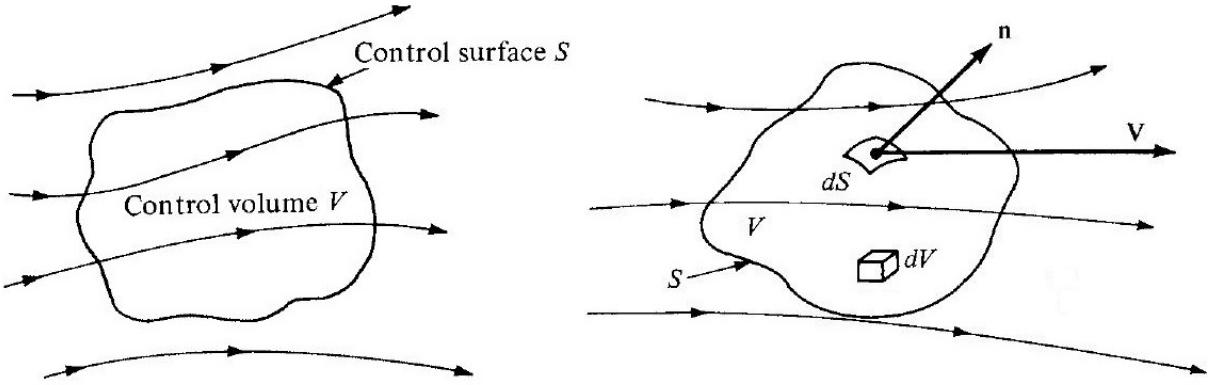

Figure 1.1: Example of control volume for fluid flow analysis

Consider the following simplified notation for the surface integral over the control surface S and for the volume integral over the control volume V

$$\oiint_S \longrightarrow \int_S \qquad \iiint_V \longrightarrow \int_V$$

Using the simplified notation just introduced, the total mass of the fluid inside the control volume V at any istant in time is

$$M_V(t) = \int_V \rho dV \tag{1.1}$$

where ρdV represents the mass of the infinitesimal volume element dV. The time rate of change, that is the time derivative, of the mass inside the control volume V is

$$\frac{dM_V(t)}{dt} = \frac{d}{dt}\int_V \rho dV \tag{1.2}$$

If the mass inside V increases, then the time derivative is positive; in turn, if the mass inside V decreases, then the time derivative is the negative of the above. Let $\overline{V} \cdot \overline{n} dS$ be the volume flow rate and $\rho\overline{V} \cdot \overline{n} dS$ the mass flow rate through the infinitesimal control surface dS. Defining the *mass flux* through dS as the mass flow rate per unit area

$$\rho(\overline{V} \cdot \overline{n})$$

and integrating over the entire control surface, we have the total mass flux through the control surface S

$$\int_S \rho(\overline{V} \cdot \overline{n}) dS$$

Taking a closer look at the expression just written above, it can be noted that if the

product $\overline{V} \cdot \overline{n}$ is positive, then the mass flux is leaving the control volume, that is it is an outflow; in turn, if the product $\overline{V} \cdot \overline{n}$ is negative, then the mass flux is entering the control volume, that is it is an inflow, because $\overline{n}$ has been assumed positive when it points out of the control volume. The *continuity equation* applied to a fixed and non-deformable control volume is

$$\frac{d}{dt}\int_V \rho dV = -\int_S \rho(\overline{V} \cdot \overline{n})dS \tag{1.3}$$

or, collecting all terms on the left-hand side

$$\frac{d}{dt}\int_V \rho dV + \int_S \rho(\overline{V} \cdot \overline{n})dS = 0 \tag{1.4}$$

Equation (1.4), derived by applying the principle of conservation of mass to the control volume, represents the continuity equation in integral form and states that the sum of the time variation of the mass inside the control volume V and the total mass flux throughout the control surface S is zero. Consider now Equation (1.3). Since the control volume used is fixed in space, the time derivative can be placed inside the volume integral, becoming a partial derivative, because the integrand is a function of both position and time

$$\int_V \frac{\partial \rho}{\partial t} dV = -\int_S \rho(\overline{V} \cdot \overline{n})dS \tag{1.5}$$

Applying the *divergence theorem*, which states that for any vector field $\overline{C}$, the following expression is valid

$$\int_S \overline{C} \cdot \overline{n} dS = \int_V \nabla \cdot \overline{C} dV \tag{1.6}$$

the term on the right-hand side of Equation (1.5) can be written as

$$\int_S \rho(\overline{V} \cdot \overline{n})dS = \int_V \nabla \cdot (\rho\overline{V})dV \tag{1.7}$$

Thus, substituting Equation (1.7) into Equation (1.5) and collecting all terms on the left-hand side, we obtain

$$\int_V \frac{\partial \rho}{\partial t} dV + \int_V \nabla \cdot (\rho\overline{V})dV = 0 \tag{1.8}$$

Now, collecting all terms inside the same volume integral, we obtain

$$\int_V \left[\frac{\partial \rho}{\partial t} + \nabla \cdot (\rho\overline{V})\right] dV = 0 \tag{1.9}$$

Since the control volume is also arbitrarly choosen, the previous expression must be valid for any arbitrary control volume V; this statement corresponds to set the integrand equal to zero. Thus, the continuity equation for a compressible flow is

$$\frac{\partial \rho}{\partial t} + \nabla \cdot (\rho \overline{V}) = 0 \tag{1.10}$$

Equation (1.10), in contrast to Equation (1.4), represents the continuity equation in differential form. For a steady flow, $\partial/\partial t = 0$; hence Equation (1.10) reduces to

$$\nabla \cdot (\rho \overline{V}) = 0 \tag{1.11}$$

1.1.1 Continuity equation for an incompressible flow

Expanding the divergence of the product, Equation (1.10) becomes

$$\frac{\partial \rho}{\partial t} + \overline{V} \cdot \nabla \rho + \rho \nabla \cdot \overline{V} = 0 \tag{1.12}$$

Considering the definition of *substantial derivative* in vector notation

$$\frac{D}{Dt} = \frac{\partial}{\partial t} + \overline{V} \cdot \nabla \tag{1.13}$$

Equation (1.12) becomes

$$\frac{D\rho}{Dt} + \rho \nabla \cdot \overline{V} = 0 \tag{1.14}$$

or

$$\frac{D\rho}{Dt} = -\rho \nabla \cdot \overline{V} \tag{1.15}$$

Rearranging the terms, the expression just derived can be written as

$$\nabla \cdot \overline{V} = -\frac{1}{\rho}\frac{D\rho}{Dt} = -v\frac{D1/v}{Dt} = \frac{1}{v}\frac{Dv}{Dt} \tag{1.16}$$

where v is the specific volume, that is the volume of fluid per unit mass, defined as

$$v = \frac{1}{\rho}$$

Thus, $\nabla \cdot \overline{V}$ can be intended as the time rate of change of the volume of a moving fluid portion, per unit volume.

For an *incompressible fluid*, the density is constant

$$\rho(\overline{r}, t) = \rho$$

so, if the fluid volume with a fixed mass has constant density, then the volume is constant. As a consequence, the fluid is said to be *incompressible* when it satisfies the following condition

$$\nabla \cdot \overline{V} = 0 \tag{1.17}$$

Substituting Equation (1.17) into Equation (1.14), we obtain

$$\frac{D\rho}{Dt} = \frac{\partial \rho}{\partial t} + \overline{V} \cdot \nabla \rho = 0 \tag{1.18}$$

Equation (1.18) states that the density of the fluid is constant along the pathlines. If we assume that the density is also *uniform*, that is

$$\rho(\overline{r}, t) = \rho_0(\overline{r}) = \rho$$

then

$$\frac{\partial \rho}{\partial t} = 0 \qquad \nabla \rho = 0 \tag{1.19}$$

and Equation (1.14) becomes

$$\nabla \cdot \overline{V} = 0 \tag{1.20}$$

which represents the continuity equation for an incompressible flow.

1.2 Momentum equation

Consider the fixed in space, non-deformable, and inertial control volume V, previously defined. The momentum of the fluid inside the control volume at any istant in time is

$$\overline{Q}_V(t) = \int_V \rho \overline{V} dV \tag{1.21}$$

where $\rho \overline{V} dV$ is the momentum of the infinitesimal volume element dV. The time derivative of the momentum of the fluid is then

$$\frac{d\overline{Q}_V(t)}{dt} = \frac{d}{dt} \int_V \rho \overline{V} dV = \int_V \frac{\partial}{\partial t} (\rho \overline{V}) dV \tag{1.22}$$

Recalling the definition of mass flux, the *momentum flux* through dS is

$$\rho\overline{V}(\overline{V}\cdot\overline{n})$$

Integrating over the entire control surface, the *momentum equation* for an inertial and non-deformable control volume is

$$\frac{d}{dt}\int_V \rho\overline{V}dV + \int_S \rho\overline{V}(\overline{V}\cdot\overline{n})dS = \overline{F}_V + \overline{F}_S \tag{1.23}$$

Equation (1.23) states that the time variation of the momentum of the fluid inside the control volume and the total momentum flux through the control surface are equal to the forces exerted on the fluid inside the control volume V. Equation (1.23) derives from the application of the second law of motion to the inertial and non-deformable control volume. The forces exerted on the fluid can be *body forces*, acting at a certain distance on the fluid inside V, defined as

$$\overline{F}_V = \int_V \rho\overline{g}dV \tag{1.24}$$

or *surface forces*, which act on the control surface S, such as pressure and shear stress, defined as

$$\overline{F}_S = \int_S \overline{t}dS \tag{1.25}$$

$\overline{g}$ is the net body force per unit mass exerted on the fluid inside the control volume and $\overline{t}$ is the *stress vector*. The stress vector is defined as

$$\overline{t} = \overline{\overline{T}}\cdot\overline{n} \tag{1.26}$$

where $\overline{\overline{T}}$ is the *stress tensor*. Substituting Equations (1.24) and (1.25) into Equation (1.23), we have

$$\frac{d}{dt}\int_V \rho\overline{V}dV + \int_S \rho\overline{V}(\overline{V}\cdot\overline{n})dS = \int_V \rho\overline{g}dV + \int_S \overline{\overline{T}}\cdot\overline{n}dS \tag{1.27}$$

Equation (1.27) expresses the momentum equation in integral form. Now, following the approach used in the previous section, that is placing the time derivative inside the volume integral, applying the divergence theorem to the surface integrals, collecting all terms on the left-hand side under the same volume integral, and setting the integrand equal to zero, the momentum equation for a compressible flow is

$$\frac{\partial}{\partial t}(\rho\overline{V}) + \nabla\cdot(\rho\overline{V}\overline{V}) = \rho\overline{g} + \nabla\cdot\overline{\overline{T}} \tag{1.28}$$

Equation (1.28) represents the momentum equation in differential form.
Now, the stress tensor can be expressed as the sum of two terms, the former due to the pressure and the latter due to the shear stress

$$\overline{\overline{T}} = -p\overline{\overline{I}} + \overline{\overline{\sigma}} \tag{1.29}$$

$\overline{\overline{\sigma}}$ is the *viscous stress tensor* and $\overline{\overline{I}}$ is the identity tensor. Thus, substituting Equation (1.29) into Equation (1.28), we have

$$\frac{\partial}{\partial t}(\rho\overline{V}) + \nabla \cdot (\rho\overline{V}\overline{V}) = \rho\overline{g} + \nabla \cdot (-p\overline{\overline{I}} + \overline{\overline{\sigma}}) \tag{1.30}$$

For a *newtonian fluid*, the viscous stress tensor $\overline{\overline{\sigma}}$ is defined as

$$\overline{\overline{\sigma}} = \mu(\nabla\overline{V} + \nabla\overline{V}^T) + \lambda\nabla \cdot \overline{V}\overline{\overline{I}} = 2\mu\overline{\overline{E}} + \lambda\nabla \cdot \overline{V}\overline{\overline{I}} \tag{1.31}$$

where

$$\overline{\overline{E}} = \left(\frac{\nabla\overline{V} + \nabla\overline{V}^T}{2}\right) \tag{1.32}$$

is the *strain rate tensor*, defined as the symmetric part of the velocity gradient $\nabla\overline{V}$.
μ is the *dynamic viscosity coefficient* and λ is the *second viscosity coefficient*. For a newtonian fluid, the so-called *Stokes' hypothesis* is valid

$$\lambda = -\frac{2}{3}\mu \tag{1.33}$$

Now, Equation (1.30) becomes

$$\frac{\partial}{\partial t}(\rho\overline{V}) + \nabla \cdot (\rho\overline{V}\overline{V}) = \rho\overline{g} + \nabla \cdot [-p\overline{\overline{I}} + \mu(\nabla\overline{V} + \nabla\overline{V}^T) + \lambda\nabla \cdot \overline{V}\overline{\overline{I}}] \tag{1.34}$$

Expanding the divergence of the terms on the right-hand side and using some vector identities, the momentum equation for a viscous compressible flow becomes

$$\frac{\partial}{\partial t}(\rho\overline{V}) + \nabla \cdot (\rho\overline{V}\overline{V}) = \rho\overline{g} - \nabla p + \mu\nabla^2\overline{V} + (\lambda + \mu)\nabla(\nabla \cdot \overline{V}) \tag{1.35}$$

1.2.1 Simplified forms of the momentum equation

By expanding the terms on the left-hand side of the previous equation and using the notation for substantial derivative, the momentum equation can be written as follows

$$\rho\frac{D\overline{V}}{Dt} = \rho\overline{g} - \nabla p + \mu\nabla^2\overline{V} + (\lambda+\mu)\nabla(\nabla\cdot\overline{V}) \tag{1.36}$$

For a *viscous incompressible flow*, since $\nabla\cdot\overline{V} = 0$, the momentum equation becomes

$$\frac{\partial}{\partial t}(\rho\overline{V}) + \nabla(\rho\overline{V}\overline{V}) = \rho\overline{g} - \nabla p + \mu\nabla^2\overline{V} \tag{1.37}$$

or

$$\frac{D\overline{V}}{Dt} = \overline{g} - \frac{1}{\rho}\nabla p + \nu\nabla^2\overline{V} \tag{1.38}$$

where ν is the *kinematic viscosity*. If we consider an *inviscid* fluid, in which the viscosity is equal to zero, then the momentum equation is

$$\frac{\partial}{\partial t}(\rho\overline{V}) + \nabla(\rho\overline{V}\overline{V}) = \rho\overline{g} - \nabla p \tag{1.39}$$

or

$$\frac{D\overline{V}}{Dt} = \overline{g} - \frac{1}{\rho}\nabla p \tag{1.40}$$

1.3 Energy equation

Consider again the fixed in space and non-deformable control volume previously defined. The total energy of the fluid inside the control volume at any instant in time is

$$E_T(t) = \int_V \rho e_T dV = \int_V \rho\left(e + \frac{V^2}{2}\right)dV \tag{1.41}$$

where e is the internal energy per unit mass and $V^2/2$ is the kinetic energy per unit mass. The time rate of change of total energy of the fluid inside the control volume is thus

$$\frac{dE_T(t)}{dt} = \frac{d}{dt}\int_V \rho\left(e + \frac{V^2}{2}\right)dV \tag{1.42}$$

In a similar fashion as previously done, defining the *total energy flux* through dS as

$$\rho\left(e + \frac{V^2}{2}\right)(\overline{V}\cdot\overline{n})$$

the *energy equation* is

$$\frac{d}{dt}\int_V \rho\left(e+\frac{V^2}{2}\right)dV + \int_S \rho\left(e+\frac{V^2}{2}\right)(\overline{V}\cdot\overline{n})dS = \dot{q}+\dot{L} \tag{1.43}$$

Equation (1.43) states that the time rate of change of total energy of the fluid inside the control volume and the total energy flux through the control surface are equal to the rate of heat added to the fluid plus the rate of work done on the fluid. It derives from applying the first law of thermodynamics to the control volume.
The heat added to the fluid derives from two contributions: the former is the volumetric heating (thermal radiation), and the latter is the heat transfer through the surface (thermal conduction). For simplicity, neglect the contibution of volumetric heating to the heat added to the fluid, that is consider that heat is transferred to the fluid just via conduction. Thus, the rate of heat addition is

$$\dot{q} = -\int_S \overline{q}\cdot\overline{n}dS = \int_S (k\nabla T\cdot\overline{n})dS \tag{1.44}$$

q is the heat flux, given by the Fourier's law

$$q = -k\nabla T \tag{1.45}$$

where k is the *thermal conductivity*.
In a similar fashion, the rate of work done on the fluid can be expressed as the sum of two terms: the former representing the rate of work done by body forces and the latter standing for the rate of work done by surface forces, that is

$$\dot{L}_V = \int_V \rho\overline{g}\cdot\overline{V}dV \tag{1.46}$$

and

$$\dot{L}_S = \int_S \overline{t}\cdot\overline{V}dS = \int_S (\overline{\overline{T}}\cdot\overline{n})\cdot\overline{V}dS \tag{1.47}$$

Thus

$$\dot{L} = \dot{L}_V + \dot{L}_S = \int_V \rho\overline{g}\cdot\overline{V}dV + \int_S (\overline{\overline{T}}\cdot\overline{n})\cdot\overline{V}dS \tag{1.48}$$

Substituting Equation (1.44) and Equation (1.48) into Equation (1.43) and following the approach established in Sections 1.1 and 1.2, the energy equation in differential form is

$$\frac{\partial}{\partial t}\left[\rho\left(e+\frac{V^2}{2}\right)\right] + \nabla\cdot\left[\rho\left(e+\frac{V^2}{2}\right)\overline{V}\right] = k\nabla^2 T + \rho\overline{g}\cdot\overline{V} + \nabla\cdot(\overline{\overline{T}}\cdot\overline{V}) \tag{1.49}$$

Considering the stress tensor as defined by Equation (1.29), we have

$$\frac{\partial}{\partial t}\left[\rho\left(e+\frac{V^2}{2}\right)\right]+\nabla\cdot\left[\rho\left(e+\frac{V^2}{2}\right)\overline{V}\right]=k\nabla^2T+\rho\overline{g}\cdot\overline{V}-\nabla\cdot(p\overline{V})+\nabla\cdot(\overline{\overline{\sigma}}\cdot\overline{V}) \quad (1.50)$$

As done previously, the energy equation given in the form of Equation (1.49) can be expressed in terms of the substantial derivative as follows

$$\rho\frac{D}{Dt}\left(e+\frac{V^2}{2}\right)=k\nabla^2T+\rho\overline{g}\cdot\overline{V}+\nabla\cdot(\overline{\overline{T}}\cdot\overline{V}) \quad (1.51)$$

1.4 Navier-Stokes equations

The continuity equation given in the form of Equation (1.10), the momentum equation given in the form of Equation (1.35), and the energy equation given in the form of Equation (1.50) are the so-called *complete Navier-Stokes equations*

$$\frac{\partial\rho}{\partial t}+\nabla\cdot(\rho\overline{V})=0 \quad (1.52a)$$

$$\frac{\partial}{\partial t}(\rho\overline{V})+\nabla\cdot(\rho\overline{V}\overline{V})=\rho\overline{g}-\nabla p+\mu\nabla^2\overline{V}+(\lambda+\mu)\nabla(\nabla\cdot\overline{V}) \quad (1.52b)$$

$$\frac{\partial}{\partial t}\left[\rho\left(e+\frac{V^2}{2}\right)\right]+\nabla\cdot\left[\rho\left(e+\frac{V^2}{2}\right)\overline{V}\right]=k\nabla^2T+\rho\overline{g}\cdot\overline{V}-\nabla\cdot(p\overline{V})+\nabla\cdot(\overline{\overline{\sigma}}\cdot\overline{V}) \quad (1.52c)$$

The continuity equation, the momentum equation, and the energy equation give a system of five equations with five unknowns, which are the velocity components, density and pressure. This system of equations, with the proper set of boundary conditions, represents the complete mathematical model which describes the motion of a viscous compressible flow.

In the case of a viscous incompressible flow, the system of equation written above becomes simpler

$$\nabla\cdot\overline{V}=0 \quad (1.53a)$$

$$\frac{D\overline{V}}{Dt}=\overline{g}-\frac{1}{\rho}\nabla p+\nu\nabla^2\overline{V} \quad (1.53b)$$

where the continuity equation is in the form given by Equation (1.20) and the momentum equation is in the form expressed by Equation (1.38). For the study of the motion of a viscous incompressible fluid, the continuity equation and the momentum equation give a system of four equations with four unknowns and are sufficient to describe the problem. This simplified system of equations will be employed later in the next chapters.

Chapter 2

Shock-expansion waves phenomenology

In this chapter a brief discussion of the shock-wave theory is presented. By using the fundamental equations for compressible flows derived in the previous chapter, the relations for the determination of the flow properties across a wave (*normal shock-wave*, *oblique shock-wave*, and *expansion wave*) are derived. By using the results from the oblique shock-wave theory, valid for any kind of discontinuity, the key equation for an expansion wave, that is the *Prandtl-Meyer relation*, is derived. This equation represents the fundamental equation at the basis of the operating condition of supersonic cascades.
For more details, which are beyond the scope of this work, refer to [1].

2.1 Speed of sound and Mach number

To begin with, it is useful to briefly define two important quantities for the study of compressible flows: the *speed of sound* and the *Mach number*.
The speed of sound is defined as

$$a = \sqrt{\gamma RT} \tag{2.1}$$

which, for an ideal gas, is a function of its temperature T and composition.
The Mach number is a dimensionless quantity defined as the ratio of the flow velocity to the local speed of sound

$$M = \frac{V}{a} \tag{2.2}$$

The definition of Mach number allows us to distinguish several regimes of flow:

- *subsonic flows*, when the fluid velocity is lower than the speed of sound ($M < 1$). Typically a flow is considered as subsonic if Mach number is in the range of 0-0.8;
- *supersonic flows*, when the fluid velocity is greater than the speed of sound ($M > 1$).

Supersonic flows are frequently characterized by the presence of propagating disturbances, called *shock waves*, across which the flow properties, such as velocity, pressure, density, and temperature, change abruptly. These discontinuities are due to the presence in the flow of a body, such as an airfoil or a blade;

- *transonic flows*, when Mach number is in the range $0.8 < M < 1.2$. Transonic flows around airfoils are characterized by mixed subsonic-supersonic regions;
- *hypersonic flows*, when Mach number is $M \gg 1$, typically $M > 5$.

Different analytical theories valid for an inviscid compressible flow are used to describe the behaviour of an airfoil in each regime. Transonic flows lack of an analytical theory because of their complex mixed nature of subsonic and supersonic flows; so the behaviour of an airfoil in that regime can be described just qualitatively and, for that reason, they are more difficult to solve numerically. In fact, while the solution of one-dimensional transonic flows does not create particular difficulties, the solution of two-dimensional and three-dimensional flows in turbomachinery or around wings and single airfoils is quite problematic, since these flows request solution methods completely different, because of their mixed nature. Transonic flows and supersonic flows around airfoils in turbomachinery will be discussed in detail later. Anyway, a more in-depth mathematical analysis of the theory concerning compressible flows is beyond the scope of this work; therefore, no further details will be given here.

2.2 Total conditions

For the analysis of compressible flows, it is useful to define the so-called *total quantities*. *Total enthalpy* and *total temperature* are defined as the enthalpy and the temperature that the flow would have if we slowed it to zero velocity *adiabatically*.
The total enthalpy h_0 is defined as

$$h_0 = h + \frac{V^2}{2} \tag{2.3}$$

For an ideal gas, $h = c_p T$; thus

$$c_p T_0 = c_p T + \frac{V^2}{2} \tag{2.4}$$

Hence, the total temperature T_0 can be defined as

$$T_0 = T + \frac{V^2}{2c_p} \tag{2.5}$$

Similarly, *total pressure* p_0 and *total density* ρ_0 are defined as the pressure and the density that the flow would have if we slowed it to zero velocity *isentropically*.
The ratio of total properties to static properties can be expressed as a function of Mach number by the following equations

$$\frac{T_0}{T} = 1 + \frac{\gamma - 1}{2} M^2 \tag{2.6a}$$

$$\frac{p_0}{p} = \left(1 + \frac{\gamma - 1}{2} M^2\right)^{\frac{\gamma}{\gamma - 1}} \tag{2.6b}$$

$$\frac{\rho_0}{\rho} = \left(1 + \frac{\gamma - 1}{2} M^2\right)^{\frac{1}{\gamma - 1}} \tag{2.6c}$$

2.2.1 Energy equation in terms of total enthalpy

For the subsequent discussion, it is useful to write the energy equation in terms of total enthalpy, in three equivalent forms. These simplified versions of the energy equation are valid under some specific assumptions, which will be properly defined.
Consider the energy equation in the form

$$\rho \frac{D}{Dt}\left(e + \frac{V^2}{2}\right) = k\nabla^2 T + \rho \overline{g} \cdot \overline{V} + \nabla \cdot (\overline{\overline{\sigma}} \cdot \overline{V}) - \nabla \cdot (p\overline{V}) \tag{2.7}$$

By using the following vector identity to expand the last term on the right-hand side of the previous equation

$$\nabla \cdot (p\overline{V}) = p\nabla \cdot \overline{V} + \overline{V} \cdot \nabla p \tag{2.8}$$

and considering the continuity equation in the form

$$\nabla \cdot \overline{V} = -\frac{1}{\rho}\frac{D\rho}{Dt} \tag{2.9}$$

we obtain

$$\nabla \cdot (p\overline{V}) = -\frac{p}{\rho}\frac{D\rho}{Dt} + \overline{V} \cdot \nabla p \tag{2.10}$$

Consider now the following vector identity

$$\nabla \cdot (p\overline{V}) = \rho \frac{D(p/\rho)}{Dt} - \frac{\partial p}{\partial t} \tag{2.11}$$

Substituting the previous equation into Equation (2.7), we have

$$\rho\frac{D}{Dt}\left(e+\frac{V^2}{2}\right)=-\rho\frac{D(p/\rho)}{Dt}+\frac{\partial p}{\partial t}+k\nabla^2T+\rho\overline{g}\cdot\overline{V}+\nabla\cdot(\overline{\overline{\sigma}}\cdot\overline{V}) \tag{2.12}$$

Thus

$$\rho\frac{D}{Dt}\left(e+\frac{V^2}{2}+\frac{p}{\rho}\right)=\frac{\partial p}{\partial t}+k\nabla^2T+\rho\overline{g}\cdot\overline{V}+\nabla\cdot(\overline{\overline{\sigma}}\cdot\overline{V}) \tag{2.13}$$

Considering the definition of enthalpy

$$h=e+\frac{p}{\rho} \tag{2.14}$$

the equation of energy written in the so-called enthalpic form is

$$\rho\frac{D}{Dt}\left(h+\frac{V^2}{2}\right)=\frac{\partial p}{\partial t}+k\nabla^2T+\rho\overline{g}\cdot\overline{V}+\nabla\cdot(\overline{\overline{\sigma}}\cdot\overline{V}) \tag{2.15}$$

Consider now the assumptions of steady, adiabatic, and inviscid flow. Thus, the previous equation can be written in a simplified form as follows

$$\rho\frac{D}{Dt}\left(h+\frac{V^2}{2}\right)=0 \tag{2.16}$$

Recalling now the definition of total enthalpy, that is Equation (2.3), we have

$$\rho\frac{Dh_0}{Dt}=0 \tag{2.17}$$

Hence

$$h_0=cost \tag{2.18}$$

that is, total enthalpy is constant in the entire flow. This statement is valid for a uniform, steady, inviscid, and adiabatic flow. For an ideal gas $h=c_pT$; hence, the energy equation can be written in three equivalent forms

$$h+\frac{u^2}{2}=const \tag{2.19a}$$

$$h_0=const \tag{2.19b}$$

$$T_0=const \tag{2.19c}$$

These equations, valid under the assumptions listed above, can be used in place of the more complex Equation (1.49) and will be employed for the subsequent analysis.

2.3 Normal shocks

Shock waves perpendicular to the flow direction are called *normal shock waves*. Consider the normal shock wave sketched in Figure 2.1, adapted from [1]. The uniform flow upstream of the shock wave is identified as region 1 (on the left), and all the corresponding variables (pressure, density, temperature, Mach number, velocity, total pressure, total enthalpy, and total temperature) are denoted by subscript 1. The uniform flow downstream of the shock is indicated as region 2 (on the right), and all the corresponding variables are denoted by subscript 2. Consider the control volume bordered by the dashed lines.

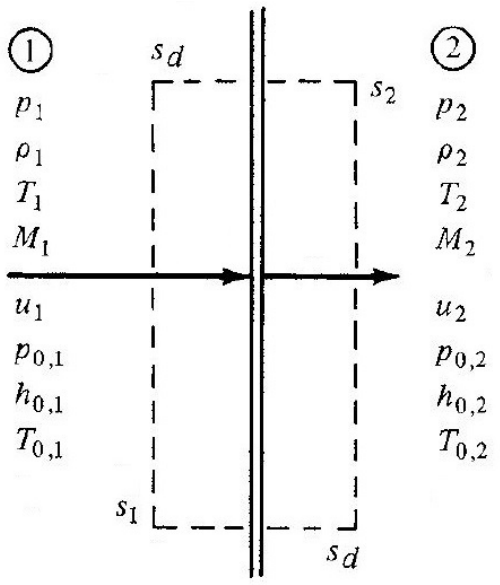

Figure 2.1: Normal shock-wave and control surface

Consider the following simplifying assumptions:

- the flow is steady
- the flow is adiabatic
- viscous effects and body forces are negligible

Consider the continuity equation in the form of Equation (1.10)

$$\frac{\partial \rho}{\partial t} + \nabla \cdot (\rho \overline{V}) = 0 \tag{2.20}$$

For the assumptions listed above, the previous equation simplifies as follows

$$\nabla \cdot (\rho \overline{V}) = 0 \tag{2.21}$$

Integrating over the entire control volume, we have

$$\int_V \nabla \cdot (\rho \overline{V}) dV = 0 \tag{2.22}$$

Applying now the divergence theorem, that is Equation (1.6), we obtain

$$\int_{s_1} \rho \overline{V} \cdot \overline{n} dS + \int_{s_2} \rho \overline{V} \cdot \overline{n} dS + \int_{s_d} \rho \overline{V} \cdot \overline{n} dS \tag{2.23}$$

where

$$\int_{s_d} \rho \overline{V} \cdot \overline{n} dS = 0 \tag{2.24}$$

is null for geometrical construction. Evaluating the integrals, we have

$$-\rho_1 u_1 s_1 + \rho_2 u_2 s_2 = 0 \tag{2.25}$$

Since $s_1 = s_2$, we obtain

$$\rho_2 u_2 = \rho_1 u_1 \tag{2.26}$$

Consider the momentum equation in the form of Equation (1.30)

$$\frac{\partial}{\partial t}(\rho \overline{V}) + \nabla \cdot (\rho \overline{V V}) = \rho \overline{g} + \nabla \cdot (-p \overline{\overline{I}} + \overline{\overline{\sigma}}) \tag{2.27}$$

For the assumptions listed above, the previous equation simplifies as follows

$$\nabla \cdot (\rho \overline{V V}) = \nabla \cdot (-p \overline{\overline{I}}) \tag{2.28}$$

Integrating over the entire control volume, we have

$$\int_V \nabla \cdot (\rho \overline{V V}) dV = \int_V \nabla \cdot (-p \overline{\overline{I}}) dV \tag{2.29}$$

Applying the divergence theorem, we obtain

$$\int_{s_1} \rho \overline{V} (\overline{V} \cdot \overline{n}) dS + \int_{s_2} \rho \overline{V} (\overline{V} \cdot \overline{n}) dS + \int_{s_d} \rho \overline{V} (\overline{V} \cdot \overline{n}) dS = - \int_{s_1} p \overline{n} dS - \int_{s_2} p \overline{n} dS - \int_{s_d} p \overline{n} dS \tag{2.30}$$

Evaluating the surface integrals in the horizontal direction, we have

$$-\rho_1 u_1^2 s_1 + \rho_2 u_2^2 s_2 = p_1 s_1 - p_2 s_2 \tag{2.31}$$

Since $s_1 = s_2$, we obtain

$$\rho_2 u_2^2 + p_2 = \rho_1 u_1^2 + p_1 \tag{2.32}$$

Lastly, consider the energy equation in one of the three equivalent forms previously derived, valid under the assumptions above

$$h_1 + \frac{u_1^2}{2} = h_2 + \frac{u_2^2}{2} \tag{2.33a}$$

$$h_{01} = h_{02} \tag{2.33b}$$

$$T_{01} = T_{02} \tag{2.33c}$$

and the equation of state $p = \rho RT$. Thus, the flow properties downstream of the shock wave can be calculated from the properties upstream of the shock wave by using the following equations

$$\rho_2 u_2 = \rho_1 u_1 \tag{2.34a}$$

$$\rho_2 u_2^2 + p_2 = \rho_1 u_1^2 + p_1 \tag{2.34b}$$

$$h_2 + \frac{u_2^2}{2} = h_1 + \frac{u_1^2}{2} \tag{2.34c}$$

$$h_2 = c_p T_2 \tag{2.34d}$$

$$\rho_2 = \frac{p_2}{RT_2} \tag{2.34e}$$

These equations are called the *Rankine-Hugoniot relations* and describe the relationship between the properties across a shock wave.
It can be shown that the relation between the Mach number upstream of the shock wave and the Mach number downstream of the shock wave is

$$M_2^2 = \frac{1 + (\gamma - 1)/2 M_1^2}{\gamma M_1^2 - (\gamma - 1)/2} \tag{2.35}$$

Furthermore, the ratio of the properties downstream the shock wave to the properties upstream can be expressed as a function of the upstream Mach number M_1 as follows

$$\frac{\rho_2}{\rho_1} = \frac{(\gamma + 1) M_1^2}{2 + (\gamma - 1) M_1^2} \tag{2.36a}$$

$$\frac{p_2}{p_1} = 1 + \frac{2\gamma}{\gamma + 1}(M_1^2 - 1) \tag{2.36b}$$

$$\frac{T_2}{T_1} = \left[1 + \frac{2\gamma}{\gamma + 1}(M_1^2 - 1)\right] \frac{(\gamma + 1) M_1^2}{2 + (\gamma - 1) M_1^2} \tag{2.36c}$$

2.4 Oblique shocks

In many real cases, when a supersonic flow is deflected and turned into itself, for example because of the presence of a body such as a wedge or an airfoil, an *oblique shock wave* is generated. An oblique shock wave is defined as a shock wave which forms an angle with the upstream uniform flow direction, called *wave angle* β. Consider the oblique shock wave sketched in Figure 2.2, adapted from [1], and the control volume identified by the dashed lines.

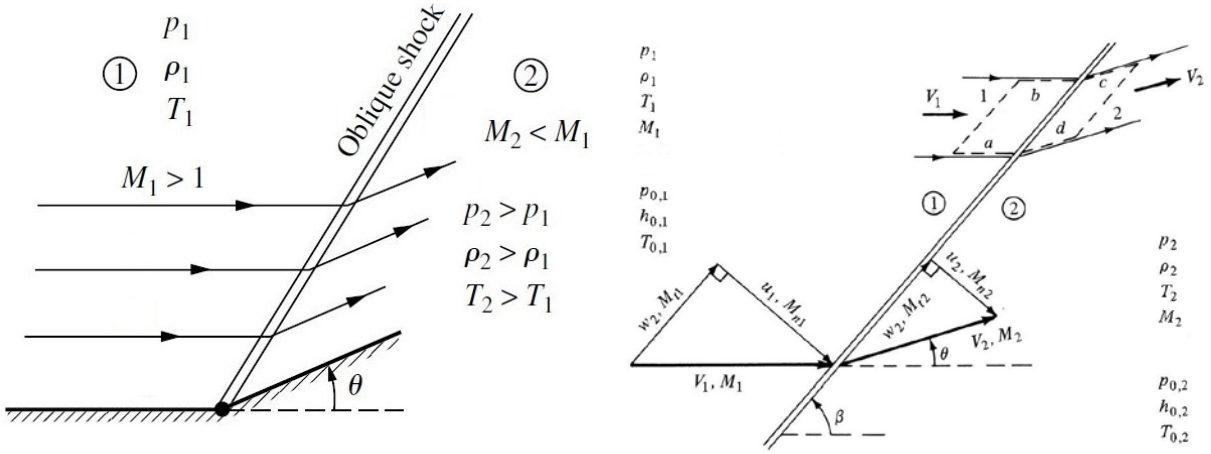

Figure 2.2: Oblique shock wave and control surface

Surface s_1 and surface s_2 are parallel to the shock wave. In turn, surfaces s_a e s_b and surfaces s_c e s_d are in the direction of the upstream flow and in the direction of the downstream flow, respectively. Consider again the simplifying assumptions of steady, inviscid, and adiabatic flow with no body forces. Consider the continuity equation in the form of Equation (1.10)

$$\frac{\partial \rho}{\partial t} + \nabla \cdot (\rho \overline{V}) = 0 \tag{2.37}$$

which, under the previous assumptions, simplifies as follows

$$\nabla \cdot (\rho \overline{V}) = 0 \tag{2.38}$$

Integrating over the entire control volume, we have

$$\int_V \nabla \cdot (\rho \overline{V}) dV = 0 \tag{2.39}$$

Applying the divergence theorem, that is Equation (1.6), we obtain

$$\int_{s_1} \rho\overline{V} \cdot \overline{n} dS + \int_{s_2} \rho\overline{V} \cdot \overline{n} dS + \int_{s_a+s_b+s_c+s_d} \rho\overline{V} \cdot \overline{n} dS = 0 \tag{2.40}$$

where

$$\int_{s_a+s_b+s_c+s_d} \rho\overline{V} \cdot \overline{n} dS = 0 \tag{2.41}$$

Evaluating the surface integrals, since $s_1 = s_2$, we have

$$\rho_2 u_2 = \rho_1 u_1 \tag{2.42}$$

Consider now the momentum equation in the form of Equation (1.30)

$$\frac{\partial \rho\overline{V}}{\partial t} + \nabla \cdot (\rho\overline{VV}) = \nabla \cdot (-p\overline{\overline{I}} + \overline{\overline{\sigma}}) \tag{2.43}$$

which under the assumptions listed above simplifies as follows

$$\nabla \cdot (\rho\overline{VV}) = \nabla \cdot (-p\overline{\overline{I}}) \tag{2.44}$$

Integrating over the entire control volume, we have

$$\int_V \nabla \cdot (\rho\overline{VV}) dV = \int_V \nabla \cdot (-p\overline{\overline{I}}) dV \tag{2.45}$$

Now, applying the divergence theorem we obtain

$$\int_{s_1} \rho\overline{V}(\overline{V} \cdot \overline{n}) dS + \int_{s_2} \rho\overline{V}(\overline{V} \cdot \overline{n}) dS + \int_{s_a+s_b+s_c+s_d} \rho\overline{V}(\overline{V} \cdot \overline{n}) dS = - \int_{s_1} p\overline{n} dS - \int_{s_2} p\overline{n} dS - \int_{s_a+s_b+s_c+s_d} p\overline{n} dS \tag{2.46}$$

Evaluating the surface integrals in the direction *normal* to the shock wave, we have

$$-\rho_1 u_1^2 s_1 + \rho_2 u_2^2 s_2 = p_1 s_1 - p_2 s_2 \tag{2.47}$$

Since $s_1 = s_2$, the previous equation leads to the following result

$$\rho_2 u_2^2 + p_2 = \rho_1 u_1^2 + p_1 \tag{2.48}$$

Similarly, evaluating the surface integrals in the direction *tangential* to the shock wave,

we have

$$-\rho_1 w_1 u_1 s_1 + \rho_2 w_2 u_2 s_2 = 0 \tag{2.49}$$

Thus

$$\rho_2 w_2 u_2 = \rho_1 w_1 u_1 \tag{2.50}$$

Dividing Equation (2.50) by Equation (2.42), we have

$$w_2 = w_1 \tag{2.51}$$

Equation (2.51) states that the tangential component of the flow velocity remains constant across an oblique shock.

Finally, consider the energy equation in the form of Equation (2.19a)

$$h_1 + \frac{V_1^2}{2} = h_2 + \frac{V_2^2}{2} \tag{2.52}$$

Since

$$V^2 = u^2 + w^2 \tag{2.53}$$

we have

$$h_1 + \frac{u_1^2 + w_1^2}{2} = h_2 + \frac{u_2^2 + w_2^2}{2} \tag{2.54}$$

From Equation (2.51), we know that $w_2 = w_1$. Hence

$$h_1 + \frac{u_1^2}{2} = h_2 + \frac{u_2^2}{2} \tag{2.55}$$

Equations (2.42), (2.48), and (2.55) are the continuity equation, the momentum equation, and the energy equation for an oblique shock wave. As can be noted, in these equations written for an oblique shock wave, only the normal component of the velocity appears, so these equations are the same as those written for a normal shock wave. Thus, the changes of the flow properties across an oblique shock wave can be calculated from the normal shock relations previously derived simply by considering the upstream Mach number normal to the shock wave

$$M_{n1} = \frac{u_1}{c_1} = \frac{v_1 \sin\beta}{c_1} = M_1 \sin\beta \tag{2.56}$$

Thus

$$M_{n2}^2 = \frac{1 + [(\gamma - 1)/2] M_{n1}^2}{\gamma M_{n1}^2 - (\gamma - 1)/2} \tag{2.57}$$

It is important to highlight that across a normal shock wave $M_2 < 1$, so the flow is always

subsonic, while across an oblique shock wave $M_{n2} < 1$, but it could be $M_2 > 1$. Hence, the flow could be supersonic even downstream of an oblique shock wave.

Without giving any further details for the sake of brevity, the so-called θ-β-M *relation* relates the deflection angle θ, induced for example by a wedge, the wave angle β, and the Mach number M_1 upstream of the shock wave

$$\tan\theta = 2\cot\beta \frac{M_1^2 \sin^2(\beta) - 1}{2 + M_1^2[\gamma + \cos(2\beta)]} \tag{2.58}$$

The most important result which can be derived by a more in-depth analysis of Equation (2.58), omitted here for the sake of brevity, needs to be highlighted because it is fundamental to better understand some aspects discussed below. This brief consideration can be visualized in Figure 2.3, taken and adapted from [1].

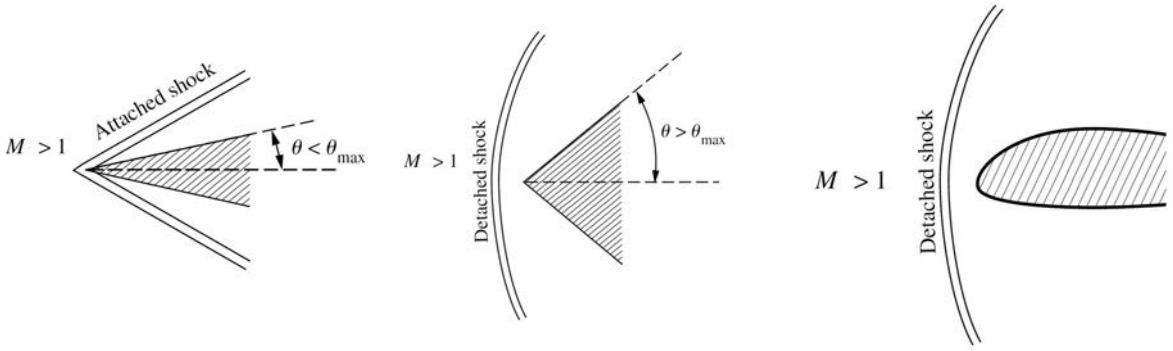

Figure 2.3: Examples of shock waves of interest

For any given upstream Mach number M_1, there is a maximum deflection angle for which the shock wave is straight and attached to the wedge. If the deflection angle θ induced by the geometry is greater than the maximum admissible deflection angle, for example if the nose of the wedge is too large or if the airfoil has a blunt nose, that is a finite thickness, as it occurs in reality, a detached curved shock, called *bow-shock*, originates at a certain distance from the body (detachment distance).

In reality, oblique shock waves does not extend to infinity. In fact, shock waves can impinge somewhere on a surface and interact with the boundary layer or can intersect other waves, both shocks and expansion waves. These wave intersections, reflections and interactions are important for the design process of turbomachines, wings or engines which have to deal with supersonic flows. The related theoretical description of these phenomena is vast and quite elaborate and a more in-depth analysis is beyond the scope of this work.

2.5 Expansion waves

A supersonic flow turned away from itself generates an *expansion wave*, or an *expansion fan*, as shown in Figure 2.4. The expansion fan is a flow region which can be conceptualized as a continuous expansion made of an infinite number of infinitesimal isentropic disturbances, called *Mach waves*, each of which forms an angle μ with the flow direction. Consider an infinitesimal expansion wave forming an angle μ with the upstream supersonic flow, as skecthed in Figure 2.4, adapted from [1].

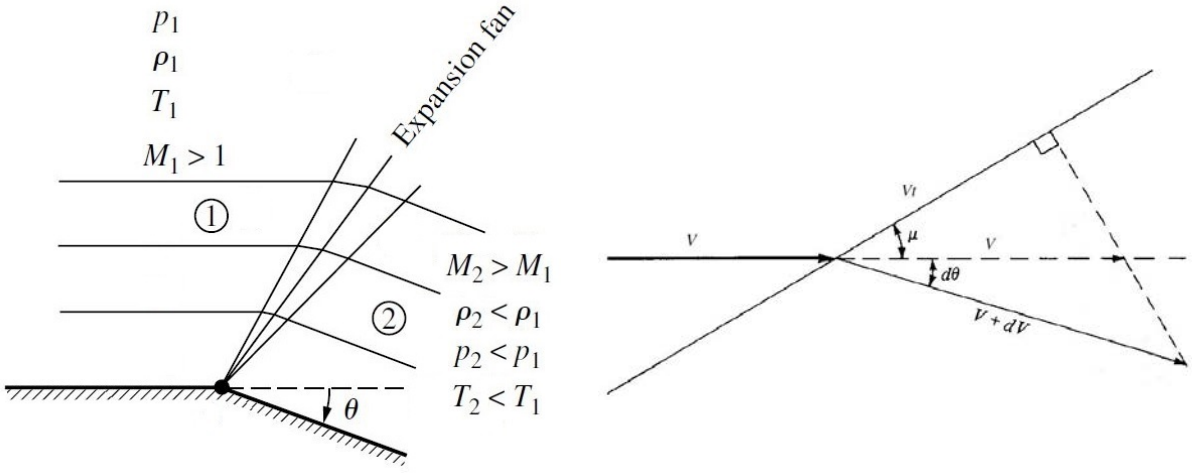

Figure 2.4: Expansion fan and Mach wave

Since an expansion wave is very weak, it produces an infinitesimally small flow deflection $d\theta$. Since the flow is deflected of the infinitesimal angle $d\theta$, as a consequence the velocity is increased of the infinitesimal quantity dV. Thus, the flow velocity downstream of the wave is $V + dV$ and it is inclined of the angle $d\theta$. The jump relations for an oblique shock wave can be applied to any kind of discontinuity of any intensity, either compression waves or expansion waves. So, it can be affirmed from previous statements that any change in velocity across a wave involves only the normal component, while the tangential component remains unchanged across the wave. Hence, we can write

$$V_t = V\cos\mu = (V + dV)\cos(\mu + d\theta) = (V + dV)_t \tag{2.59}$$

Hence

$$\frac{V + dV}{V} = \frac{\cos\mu}{\cos(\mu + d\theta)} = \frac{\cos\mu}{\cos\mu\cos d\theta - \sin\mu\sin d\theta} \tag{2.60}$$

Since the deflection angle $d\theta$ is infinitesimally small, we have

$$\cos d\theta \simeq 1 \quad \sin d\theta \simeq d\theta$$

and as a consequence

$$\frac{V + dV}{V} \simeq \frac{\cos \mu}{\cos \mu - \sin \mu d\theta} \tag{2.61}$$

Now divide the previous equation by $\cos \mu$

$$\frac{V + dV}{V} \simeq \frac{1}{1 - \tan \mu d\theta} \simeq 1 + \tan \mu d\theta \tag{2.62}$$

Thus, we obtain

$$1 + \frac{dV}{V} = 1 + \tan \mu d\theta \tag{2.63}$$

Simplifying properly, we have

$$\frac{dV}{V} = \tan \mu d\theta \tag{2.64}$$

Now, the following expression is valid for a Mach wave propagating through a flow

$$\sin \mu = \frac{a}{V} = \frac{1}{M} \tag{2.65}$$

Thus, we have

$$\cos^2 \mu = 1 - \sin^2 \mu = 1 - \frac{1}{M^2} = \frac{M^2 - 1}{M^2} \tag{2.66}$$

and

$$\tan^2 \mu = \frac{1}{M^2} \frac{M^2}{M^2 - 1} \tag{2.67}$$

Thus, we obtain

$$\tan \mu = \frac{1}{\sqrt{M^2 - 1}} \tag{2.68}$$

Now, consider the definition of Mach number $M = V/a$, from which we have $V = Ma$. Considering the logarithms, we have

$$\ln V = \ln M + \ln a \tag{2.69}$$

Differentiating the previous equation, we obtain

$$\frac{dV}{V} = \frac{dM}{M} + \frac{da}{a} \tag{2.70}$$

From Equation (2.1) and Equation (2.6a) we have

$$\frac{a_0^2}{a^2} = \frac{\gamma R T_0}{\gamma R T} = \frac{T_0}{T} = 1 + \frac{\gamma - 1}{2} M^2 \tag{2.71}$$

where a_0 is the total speed of sound. Solving for a we obtain

$$a = a_0 \left(1 + \frac{\gamma - 1}{2} M^2 \right)^{-\frac{1}{2}} \tag{2.72}$$

Differentiating Equation (2.72), we have

$$\frac{da}{a} = \frac{da_0}{a_0} - \frac{1}{2} \frac{d\left(1 + \dfrac{\gamma - 1}{2} M^2 \right)}{1 + \dfrac{\gamma - 1}{2} M^2} \tag{2.73}$$

Since the term da_0/a_0 is zero for an adiabatic flow, expanding the differential on the right-hand side, we have

$$\frac{da}{a} = -\frac{[(\gamma - 1)/2] M dM}{1 + [(\gamma - 1)/2] M^2} \tag{2.74}$$

Multiplying and dividing by M, we obtain

$$\frac{da}{a} = -\frac{[(\gamma - 1)/2] M^2}{1 + [(\gamma - 1)/2] M^2} \frac{dM}{M} \tag{2.75}$$

Substituting Equation (2.75) into Equation (2.70), we have

$$\frac{dV}{V} = \frac{dM}{M} \left(\frac{1}{1 + [(\gamma - 1)/2] M^2} \right) \tag{2.76}$$

Thus, substituting Equation (2.76) into Equation (2.64), written in the form

$$d\theta = \frac{1}{\tan \mu} \frac{dV}{V} \tag{2.77}$$

we obtain

$$d\theta = \frac{1}{\tan \mu} \frac{dV}{V} = \frac{\sqrt{M^2 - 1}}{1 + [(\gamma - 1)/2] M^2} \frac{dM}{M} \tag{2.78}$$

Equation (2.78) can be integrated from region 1 upstream of the expansion fan to region 2 downstream of the expansion fan, that is for a finite number of Mach waves which produce

a finite deflection θ and an increase in Mach number from M_1 up to M_2. Thus

$$\int_0^{\theta} d\theta = \int_{M_1}^{M_2} \frac{\sqrt{M^2-1}}{1+[(\gamma-1)/2]M^2}\frac{dM}{M} \tag{2.79}$$

and

$$\theta = \nu(M_2) - \nu(M_1) \tag{2.80}$$

Equation (2.80), with the given M_1 and the corresponding value of $\nu(M_1)$, allows to obtain, using the known value of θ, the value of $\nu(M_2)$ and the corresponding value of M_2.
Carrying out the integration

$$\nu(M) = \int \frac{\sqrt{M^2-1}}{1+[(\gamma-1)/2]M^2}\frac{dM}{M} \tag{2.81}$$

we obtain the so-called *Prandtl-Meyer function*

$$\nu(M) = \sqrt{\frac{\gamma+1}{\gamma-1}}\tan^{-1}\left[\frac{\gamma-1}{\gamma+1}(M^2-1)\right] - \tan^{-1}(\sqrt{M^2-1}) \tag{2.82}$$

The Prandtl-Meyer function and Equation (2.80) just derived represent the end point of this chapter and the most important result we need for the subsequent discussion. In fact, they are the main equations which govern the flow in supersonic cascades, as will be explained in detail later.

Chapter 3

Supersonic compressor cascades

In this chapter, the main characteristics of supersonic compressor cascades are described. The most important geometric and performance parameters of a supersonic compressor cascade are briefly listed and explained. The most common shapes of the airfoils used in supersonic cascades are presented, along with a qualitative description of the common shock-wave pattern inside the blade passage. Moreover, by using the equations derived in the previous chapters, the operating condition of supersonic cascades, referred as *unique incidence*, is analyzed.

3.1 Blade and cascade geometric parameters

A typical example of a supersonic compressor airfoil is sketched below in Figure 3.1.

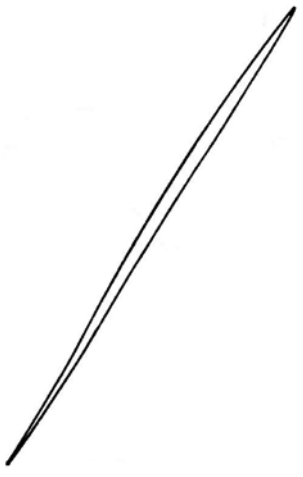

Figure 3.1: Example of supersonic compressor airfoil

The geometry of an airfoil or a blade section is described with a variety of terms, the most important of which need to be briefly listed and properly defined:

- the *leading edge* is the point at the front of the airfoil and the *trailing edge* is defined as the point at the rear of the airfoil;
- the *chord line* c, or simply *chord*, is the straight line which connects leading edge and trailing edge. It is used as the reference dimension of the airfoil;
- the *suction surface*, or *suction side*, can be simply defined as the upper surface of the airfoil. The *pressure surface*, or *pressure side*, is defined as the lower surface of the airfoil.
- the *camber line* is defined as the curve that is halfway between the suction side and the pressure side of the airfoil.

An example of cascade is sketched in Figure 3.2. A linear cascade can be simply defined as a two-dimensional array of profiles, which represent the geometric and aerodynamic equivalent of an axial compressor rotor blade section. The following design parameters are used in the geometric description of a two-dimensional axial compressor cascade:

- ξ is defined as the coordinate in cascade axial direction and η is defined as the coordinate in cascade tangential direction;
- the *pitch* s is defined as the spacing between two consecutive blades;
- the angle between the axial direction and the chord is defined as the *stagger angle* β_s;
- the projection of the chord on the axial direction is the *axial blade chord* c_{ax};
- the *thickness chord ratio* t/c is defined as the ratio of the maximum thickness to blade chord;
- the blade *solidity* is defined as the ratio of blade chord length to pitch

$$\sigma = \frac{c}{s} \tag{3.1}$$

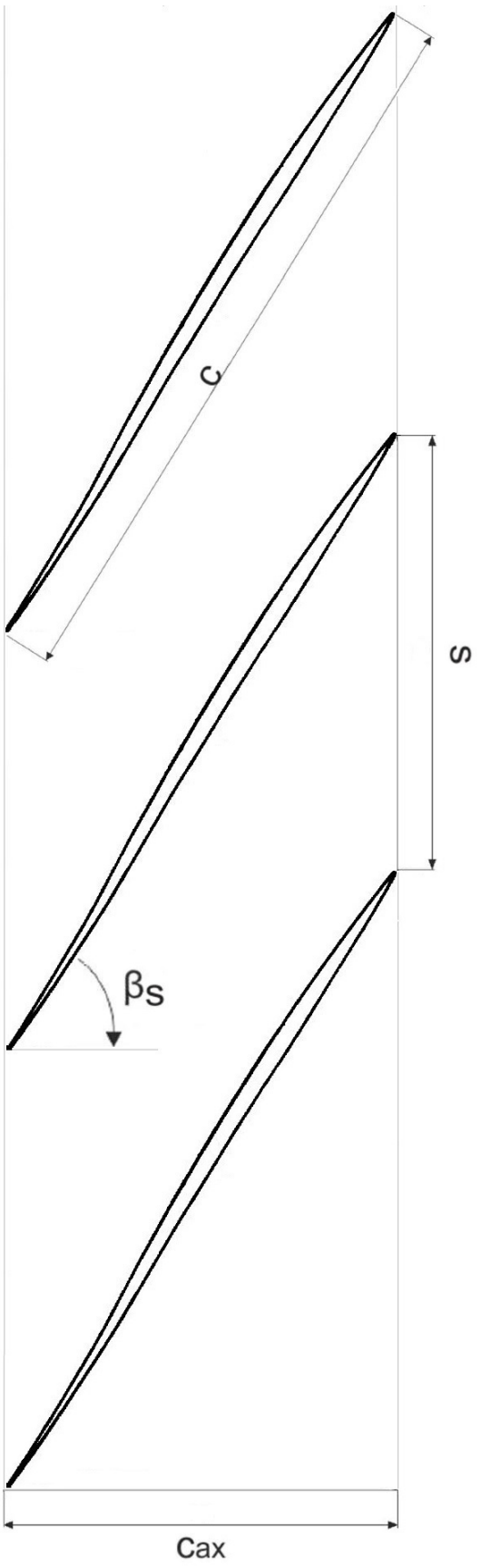

Figure 3.2: Example of supersonic compressor cascade

3.2 Cascade performance parameters

The main parameters generally used to describe the performance of a cascade are the *axial velocity-density ratio* (AVDR), the *total-pressure loss coefficient* ω, and the *isentropic Mach number* M_{is}.

The axial velocity-density ratio (AVDR) is a parameter used to check if a flow through a cascade is two-dimensional. It is defined as the ratio of the product of axial velocity and density at cascade exit to the product of axial velocity and density at cascade inlet

$$AVDR = \frac{\rho_2 u_2}{\rho_1 u_1} \tag{3.2}$$

Generally speaking, the flow through a cascade is two-dimensional when the axial velocity density ratio (AVDR) is unity. However, in reality, a cascade has a three-dimensional flow behaviour, because of the developing of secondary flows. In a CFD simulation of a periodic two-dimensional cascade model, the AVDR is always unity and a 2D solver solves a pure two-dimensional flow through the cascade. The AVDR has a strong influence on the cascade performance, the mean flow exit angle, and the shock pattern.

The total-pressure loss coefficient ω is defined as the ratio of the difference between the total pressure at cascade inlet and the total pressure at cascade exit to the difference between the total pressure and the static pressure at cascade inlet

$$\omega = \frac{p_{01} - p_{02}}{p_{01} - p_1} \tag{3.3}$$

The total-pressure loss coefficient is an important performance parameter, which gives the loss in total pressure in a non-isentropic flow. In a supersonic compressor cascade, the total pressure losses are due to viscous losses, resulting from the shock wave-boundary layer interaction and the related separation of the boundary layer, and to shock losses, caused by the shocks inside the blade passage and the detached bow shock in front of the blade leading-edge. The total-pressure loss coefficient is often used instead of the cascade efficiency

$$\eta = \frac{1 - \left(\frac{p_2}{p_{02}}\right)^{\frac{\gamma-1}{\gamma}}}{1 - \left(\frac{p_2}{p_{01}}\right)^{\frac{\gamma-1}{\gamma}}} \tag{3.4}$$

The isentropic Mach number is defined as the Mach number without losses in the flow and is often plotted for turbomachinery blades. The isentropic Mach number can be computed from the isentropic flow relations using Equation (2.6b):

$$M_{is} = \sqrt{\frac{2}{\gamma - 1}\left[\left(\frac{p_{01}}{p}\right)^{\frac{\gamma-1}{\gamma}} - 1\right]} \tag{3.5}$$

where p_{01} is the inlet total pressure, p_1 is the local static pressure, and γ is the ratio of specific heats, for air 1.4.

3.3 Supersonic airfoils for axial compressors

Airfoils for supersonic axial compressors differ significantly from those adopted for subsonic axial compressors. The difference in shape is due to the supersonic entry flow, which requires the airfoil to have particular characteristics, such as a sharp leading edge, a thickness as thinner as possible, and a small curvature. For that reason, much effort has been made in the past to design airfoils able to efficiently operating at supersonic inlet conditions. Without going into too much detail, the main types of supersonic compressor airfoils are the DCA (Double Circular Arc), the MCA (Multiple Circular Arc), the CW (Circular-wedge), and the S-shape profiles. Generally speaking, supersonic/transonic compressor cascades are characterized by airfoils with high stagger angle ($> 50°$-$60°$), small thickness ($t/c \simeq 2\%$), and minimum flow deflection angle. Moreover, the overall performance of the cascade is considerably influenced by the shock pattern inside the passage, which is deeply connected to the shape of the blade. In fact, the shock pattern in a supersonic compressor cascade varies significantly according to blade geometry, cascade geometry, and operating conditions. The operating range varies according to blade geometry as well. In fact, it varies from a maximum inlet Mach number around 1.3 for the MCA profiles to an inlet Mach number even higher than 1.6 for the S-shape profiles. A sketch of the main supersonic compressor cascade blade shapes is reported in the Figures below, adapted from [16]. In Figure 3.3 a sketch of a DCA-cascade is reported. This class of airfoils is characterized by both the suction side and the pressure side made of circular arcs. The flow, passing through the cascade, is accelerated until a normal shock occurs at the passage entrance and then it is decelerated to subsonic velocity in the rearmost part of the passage. The DCA airfoil presents the disadvantage of a large increase in entropy across the shock ahead of the leading-edge, which becomes considerable at higher Mach numbers. This fact extremely limits the range of Mach numbers at which the cascade can operate.

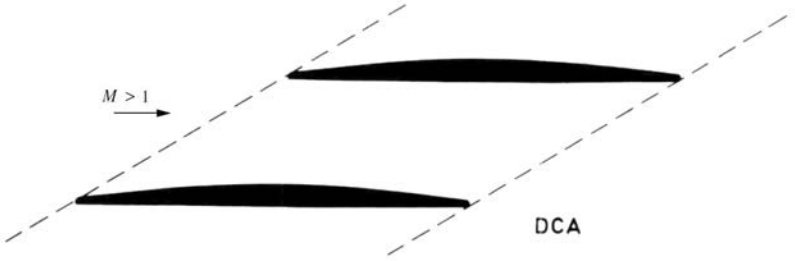

Figure 3.3: DCA-cascade

The development of MCA airfoils, sketched in Figure 3.4, reduced the shock losses in the entrance region of the cascade. This class of airfoils is characterized by a suction side made of several circular arcs of different curvature and by a lower camber. Compared to the MCA airfoils, the CW profiles, shown in Figure 3.5, are characterized by a reduction in the curvature of the suction side at the entrance region up to zero, which guarantees a further reduction in total pressure losses related to shock waves ahead of the leading-edge.

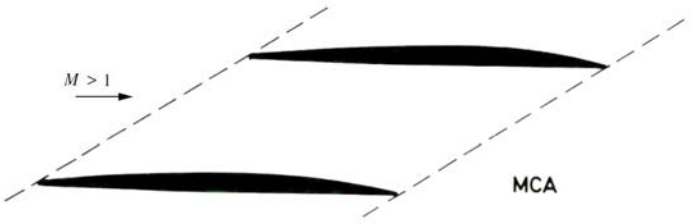

Figure 3.4: MCA-cascade

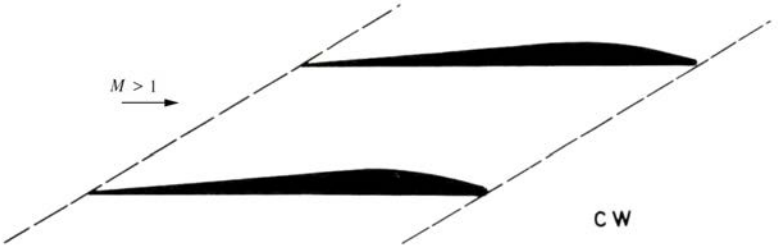

Figure 3.5: CW-cascade

However, if the Mach number of the incoming flow is increased to high supersonic values, typically in the range 1.3-1.6, the rise in entropy becomes too high and the efficiency of the cascade is considerably reduced, because of the strong shock wave at the passage entrance. In order to extend the range of inlet Mach numbers at which a cascade and, as a consequence, the related compressor rotor in an aircraft engine can operate, a new class of profiles, called external compression profiles, or precompression airfoils, or just S-shape airfoils, was designed. In Figure 3.6 a generic S-shape airfoils cascade is reported. This class of airfoils allows to reach quite high supersonic Mach numbers, making the cascade capable to operate in supersonic regime and not just at transonic inlet conditions.

Figure 3.6: S-shape supersonic cascade

Instead of obtain the desired compression through the cascade by using one strong normal shock at the passage entrance, in a cascade made of S-shape airfoils this is realized by a series of oblique shocks out of the covered passage. This "compression fan" reduces the average Mach number at the passage entrance to a value lower than the inlet Mach number, reducing in this way the shock losses and the viscous losses caused by the strong shock wave-boundary layer interaction on the surfaces of the profile. A very thin leading-edge further minimizes the shock losses caused by the detached bow shock ahead of the airfoil. However, the shock pattern inside the blade passage becomes more complicated. In fact, it is characterized by oblique shocks which impinge on the surfaces of the airfoil and are reflected throughout the passage, giving rise to a complex shock wave-boundary layer interaction.

3.3.1 Specification of axial compressor airfoils geometry

In order to define the shape of a compressor blade profile, such as those reported in the Figures above, the section camber line and the section thickness distribution must be described mathematically by equations. Once the two main geometric parameters have been properly specified, the coordinates of the points of the blade surfaces, that is suction side and pressure side, and the section properties useful for structural analysis and manufacturing process can be determined. Without going into too much detail, a brief overview of the method used for designing axial compressor blade sections is presented below. The simplified overview carried out here takes as its starting point the mathematical analysis developed in [10].

The camber line is described by an equation of the form $y = f(x)$, where x varies from 0 at the leading edge to 1 at the trailing edge. The x coordinate is usually defined in the cascade plane axial direction and not in the direction of the airfoil chord line. To obtain a camber line suitable for an S-shape airfoil, it has been proved that it is convenient to write an expression defining a fourth order polynomial camber line or an exponential camber line. Moreover, the general approach adopted for obtaining an equation for the camber line of an S-shape airfoil is to write an expression for the second derivative and integrate twice. The second derivative of a fourth order polynomial can be written in the form of a parabola

$$(x - h)^2 = 4a(y'' - k) \tag{3.6}$$

or

$$y'' = \frac{1}{4a}(x - h)^2 + k \tag{3.7}$$

where h is the point on x-axis where the second derivative is maximum and k is the value of the second derivative in that point. Integrating twice, we obtain an expression for a fourth order polynomial camber line

$$y = \frac{1}{48a}(x - h)^4 + \frac{k}{2}x^2 + bx + c \tag{3.8}$$

The coefficients in the previous equation can be determined by applying a proper set of conditions. Five conditions are necessary

$$x = 0: \quad y = 0 \tag{3.9a}$$

$$y' = \tan\alpha_1 \tag{3.9b}$$

$$y'' = P(y'')_{max} \tag{3.9c}$$

$$x = 1: \quad y' = \tan\alpha_2 \tag{3.9d}$$

$$y'' = Q(y'')_{max} \tag{3.9e}$$

The conditions above are written in the most general form. The first condition fixes a point in the coordinate system; the second condition and the fourth condition define the slope at the leading edge and at the trailing edge, respectively; the third condition and the fifth condition are imposed on the ratio of the second derivative at the leading edge and at the trailing edge, respectively, to the point where the value of the second derivative is maximum. The conditions imposed on the second derivative allow to specify a negative, null or slightly positive camber at the leading edge and to avoid high curvatures at the trailing edge, which determine large deviation angles and high losses. The application of the conditions above leads to the following results

$$a = \frac{1}{4(\tan\alpha_1 - \tan\alpha_2)}\left[\frac{P}{1-P}h^2 + h - \frac{1}{3}\right] \tag{3.10a}$$

$$b = \frac{h^3}{12a} + \tan\alpha_1 \tag{3.10b}$$

$$c = -\frac{h^4}{48a} \tag{3.10c}$$

$$k = -\frac{h^2}{4a(1-P)} \tag{3.10d}$$

$$h = \frac{1}{1 + \sqrt{\dfrac{1-Q}{1-P}}} \tag{3.10e}$$

where $Q = 0.5$ and $P = 0$, typically.

In order to obtain an S-shape airfoil satisfying specific design and performance characteristics, it is necessary to specify the inflection point s of the camber line, that is the point where the camber line changes in curvature. The exponential camber line allows to specify that point, which can be collocated anywhere on the camber line and can assume any value. The second derivative for an exponential camber line can be written in the

following form

$$y'' = b(x-s)e^{a(x-s)} \tag{3.11}$$

Integrating twice, we have

$$y = \frac{b}{a^3}e^{a(x-s)}[a(x-s)-2] + c(x-s) + d \tag{3.12}$$

Two sets of conditions must be applied for determining the coefficients in the previous equation: one set from 0 to s and another set from s to 1, that is from the leading edge to the inflection point and from the inflection point to the trailing edge, respectively. Thus, eight coefficients must be determined. Moreover, it is necessary to add another condition to the set written above

$$x = s: \quad y' = \tan\alpha_s \tag{3.13}$$

which allows to have a smooth transition across the inflection point between the forward and the rearmost portion of the camber line. Considering that the maximum value of the second derivative is

$$y''_{max} = -\frac{b}{ea} \tag{3.14}$$

which occurs where $y''' = 0$, that is at

$$x = s - \frac{1}{a} \tag{3.15}$$

and applying the following conditions for the forward portion of the camber line

$$\begin{aligned} x = 0: &\quad y = 0 \\ &\quad y' = \tan\alpha_1 \\ &\quad y'' = P(y'')_{max} \\ x = s: &\quad y' = \tan\alpha_s \end{aligned} \tag{3.16a}$$

and the following conditions for the rearmost part

$$\begin{aligned} x = s: &\quad y' = \tan\alpha_s \\ &\quad y_2 = y_1 \\ x = 1: &\quad y' = \tan\alpha_2 \\ &\quad y'' = Q(y'')_{max} \end{aligned} \tag{3.17a}$$

the eight coefficients a_1, a_2, b_1, b_2, c_1, c_2, d_1, and d_2 can be determined (calculation steps have been omitted for the sake of brevity, since they are quite complicated).
In order to obtain a double-circular-arc (DCA) airfoil or a multiple-circular-arc (MCA) airfoil, useful for a wide range of applications in turbomachinery, a circular arc camber line can be considered. The equation of this camber line is of the form

$$(x - x_O)^2 + (y - y_O)^2 = R^2 \tag{3.18}$$

where (x_O,y_O) and R are the center and the radius of the circle of which the camber line is a circular arc. Considering a proper set of conditions, that is neglecting those involving the second derivative, it is possible to define uniquely a circular-arc camber line for a DCA or a MCA airfoil.

Once the camber line has been defined, the thickness distribution can be expressed in equation form too. A supersonic compressor airfoil, as stated before, must satisfy some particular features, so the thickness distribution must be properly defined. In particular, the thickness distribution equation for an S-shape airfoil must allow to collocate the maximum thickness at any point on the rearmost half part of the airfoil and must allow to specify any value for the maximum thickness. Moreover, it must avoid any discontinuity in curvature and must allow to have a leading edge as thinner as possible. The standard method for defining the thickness distribution of an S-shape airfoil is to specify it with two third-order equations, one from the leading edge to the point of maximum thickness Z on the camber line and the other from that point to the trailing edge

$$y = a_1 x^3 + b_1 x^2 + c_1 x + d_1 \tag{3.19}$$

$$y = a_2 (x - Z)^3 + b_2 (x - Z)^2 + c_2 (x - Z) + d_2 \tag{3.20}$$

Applying the following conditions for the forward half part, that is from the leading edge to the point of maximum thickness

$$\begin{aligned} x = 0: \quad & y = y_0 \\ & y'' = 0 \\ x = Z: \quad & y = T/2 \\ & y' = 0 \end{aligned} \tag{3.21a}$$

and the following conditions for the rearmost half part, that is from the point of maximum

thickness to the trailing edge

$$\begin{aligned} x = Z: \quad & y = T/2 \\ & y' = 0 \\ & y'' = y''_{(LEportion)} \\ x = 1: \quad & y = y_1 \end{aligned} \tag{3.22a}$$

where T is the maximum thickness, the coefficients of the two equations can be determined. The conditions listed above allow to specify independently the thickness at the leading edge and at the trailing edge. Moreover, the airfoil is closed at the leading edge with a circular arc, which can be defined specifying a leading edge radius. Usually, the airfoil is closed at the trailing edge connecting the pressure side and the suction side end points with a straight line. The conditions imposed on the first and second derivatives allow to have a continuous thickness distribution.
To specify a thickness distribution for a DCA airfoil or for a MCA airfoil is quite complicated, because it requires to use polar coordinates. Moreover, the thickness of the airfoil must be defined as the difference between the mathematical expression of two arcs representing the upper and the lower surfaces of the airfoil. For further details refer to [10].

3.4 Typical shock wave pattern in supersonic cascades

As stated before, the shock pattern in a supersonic compressor cascade is quite complex. On the basis of a wide range of experimental results, the shock wave pattern characteristic of a supersonic compressor cascade at design operating conditions is similar to the one sketched in Figure 3.7, taken and adapted from [18] and [28].

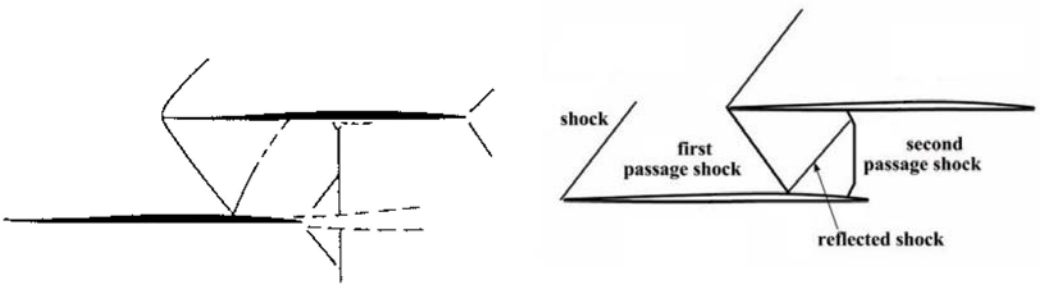

Figure 3.7: Typical shock wave pattern of a supersonic cascade at design operating condition

Obviously, the shock wave pattern varies according to the blade geometry, the cascade geometry, and the cascade operating conditions. Anyway, generally speaking, for supersonic compressor cascades operating at the design condition, the typical shock wave pattern is characterized by two shocks in the passage: the former at the entrance of the cascade and the latter located near the exit of the passage. The finite thickness of the leading edge develops a detached bow shock, which branches off into two parts. The upper branch, which is the weaker one, extends into the upstream region of the flow field, while the lower branch, which is the stronger one, runs into the blade passage. The oblique branch of the bow shock running into the passage is usually referred as first-passage shock; the quasi-normal shock near the passage exit is usually called second-passage shock. The detached bow shock in front of the airfoil is weak, since the leading edge is thin. The precompression shock, which originates from the coalescence of the compression shocks in the foremost part of the suction side, intersects the bow shock of the adjacent blade. The first passage shock is generally reflected at the suction side of the adjacent blade, giving rise to a series of reflected shocks and to a strong shock-boundary layer interaction. The reflected shock can intersect the pressure side of the adjacent blade or the second passage shock, causing loss in total pressure. In many cases, the first passage shock may not be reflected by the suction side of the adjacent blade, since it can be a normal shock or can degenerate in a lambda shock, because of the interaction with the boundary layer. The so-called lambda shock is an important and very common phenomenon inside supersonic turbomachines. This particular shock-wave pattern occurs when a shock wave hits a surface and interacts with the boundary layer. When a straight shock approaches a wall, it becomes curved at the wall, impinging on the boundary layer. The interaction between the shock wave and the boundary layer can cause the detachment of the boundary layer with a potential subsequent reattachment (depending on the strength of the incident shock wave), giving rise to a very complex system of shock-waves and expansion waves. The second passage shock, when present, is located at the exit of the blade passage and presents lambda shock structures at both ends near the surfaces of the two blades between which it is included, which form because of the strong shock wave-boundary layer interaction.

When the static backpressure is increased, that is at off-design operating conditions, the qualitative nature of the shock wave pattern inside the passage changes, as sketched in Figure 3.8, taken and adapted from [18] and [28]. As we can see, the flow pattern is completely different. The first passage shock intersects the suction side of the adjacent blade near the blade passage entrance, giving rise to a lambda-shock with a quasi-normal shock part and a strong complete boundary layer separation. In this case, the second passage shock tends to disappear as the static back pressure increases. While the lambda

shocks lead to a reduction of the shock wave strength and, as a consequence, of the shock losses, the strong separation of the boundary layer causes an increase in the viscous losses and in the overall total pressure losses.

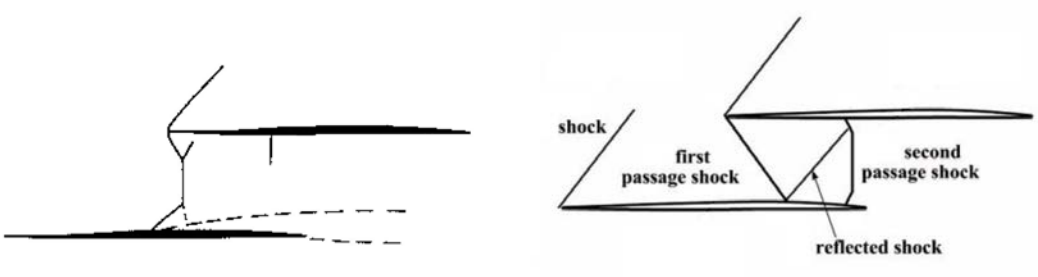

Figure 3.8: Typical shock wave pattern of a supersonic cascade at off-design operating conditions

3.5 Supersonic inlet flows

In a supersonic compressor cascade, as the name suggests, the approaching flow is supersonic. When the Mach number is supersonic, a complex shock pattern occurs in front of the leading-edge of the blades and inside the blade passage, as was shown. In a supersonic compressor cascade, various flow configurations are possible, as can be seen in Figure 3.9, taken from [19].

Let M_1 denote the Mach number at cascade inlet and M_2 the Mach number at cascade exit, in a reference frame relative to the cascade. Consider the inlet flow angle β_1 and the axial component of the inlet Mach number $M_{1ax} = M_1 \cos\beta_1$. Consider the case of supersonic cascade in which $M_1 > 1$ and $M_2 < 1$. In this operating condition, if $M_{1ax} < 1$, the axial flow at cascade inlet is subsonic and there are two possible flow configurations:

- the *started condition*, sketched in Figure 3.9a, which is characterized by shock waves and/or expansion waves ahead of the cascade and inside the blade passage, according to the positive or negative incidence of the inlet flow. In started supersonic cascade flow, the approaching flow Mach number and the inlet flow angle are dependent of each other. The cascade operation is possible only at one particular incidence, known as *unique incidence*, which establishes a particular relationship between the inlet Mach number M_1 and the inlet flow angle β_1, stating that it is not possible to change M_1 without affecting β_1 at once. In this condition, the mass flow is choked and the exit Mach number and the exit flow angle are determined by the back pressure, whereas the upstream flow is not influenced;

- the *unstarted condition*, reported in Figure 3.9b, characterized by a detached bow shock in front of the leading-edge.

The case of a supersonic cascade in which $M_{1ax} > 1$, sketched in Figure 3.9c, is not of practical interest. For that reason and for the sake of brevity, the following analysis is dedicated just to supersonic cascades operating in started condition with subsonic axial Mach number, because of their importance for transonic/supersonic compressor rotor applications. For further details concerning cascade flows, refer to [14] and [19].

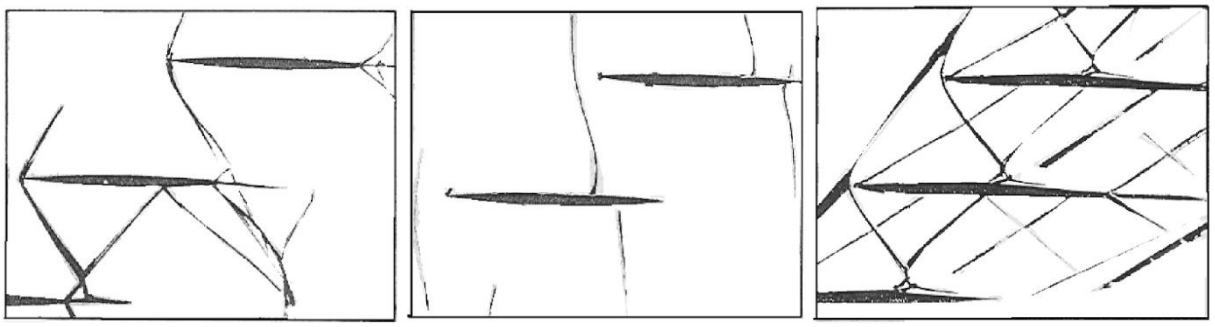

(a) (b) (c)

Figure 3.9: Different inlet flow conditions for a supersonic cascade

3.6 Unique incidence condition

A wide and very detailed explanation of the unique incidence operating condition for supersonic cascades is reported in [17]. For the sake of brevity, just a brief qualitative description is reported below.

Consider a semi-infinite flat-plate cascade with a stagger angle β_s, sketched in Figure 3.10, taken and adapted from [29]. Consider an approaching supersonic flow with Mach number M_∞ and inlet angle β_∞, different than the stagger angle ($\beta_\infty \neq \beta_s$). Since the blades of the cascade are flat-plates, their thickness and camber are negligible. Consider the lowest blade as the first blade approached by the flow. Thus, the first blade sees the inlet flow approaching with an angle β_∞. Two different wave patterns occur depending on the incidence, positive or negative, of the approaching flow over the first blade, that is according to the sign of β_∞.

Figure 3.10: Semi-infinite flat-plate cascade

Consider a semi-infinite flat plate cascade in a uniform supersonic flow with $\beta_\infty > 0$ (or $\beta_\infty > \beta_s$), that is at *positive incidence*, as sketched in Figure 3.11, taken and adapted from [29]. In this case, a series of Prandtl-Meyer expansion waves, depicted by the dashed lines, develops from the leading edge in the upper region in front of the cascade. The expansion fan accelerates the flow up to M_1 and turnes it into the flat plate direction, that is it turns the flow of an angle $\beta_1 = \beta_s$, as sketched in Figure 3.11. Since the axial Mach number is subsonic, the expansion fan affects the flow ahead of all the other blades. Thus, the incoming flow approaching all the other blades is characterized by a Mach number M_1 and an incidence angle $\beta_1 = \beta_s$, that is it approaches all the other blades with null incidence.

Consider the same semi-infinite flat plate cascade in a uniform supersonic flow with $\beta_\infty < 0$ (or $\beta_\infty < \beta_s$), that is at *negative incidence*, as sketched in Figure 3.12, taken and adapted from [29]. In this case, a compression shock wave, depicted by the solid line, develops in the upper region. The shock decelerates the flow up to M_1 and turns it of an angle $\beta_1 = \beta_s$.

Thus, in a semi-infinite cascade with an approaching flow with both positive and negative incidence, the first blade sees an incoming flow with Mach number M_∞ and flow angle β_∞ and sets the incoming flow conditions for all the other blades of the cascade, which see an approaching flow with Mach number M_1 and flow angle $\beta_1 = \beta_s$. All the blades except the first one, experience a periodic inlet flow with null incidence, regardless of the Mach number M_∞ and the flow angle β_∞ of the undisturbed upstream flow.

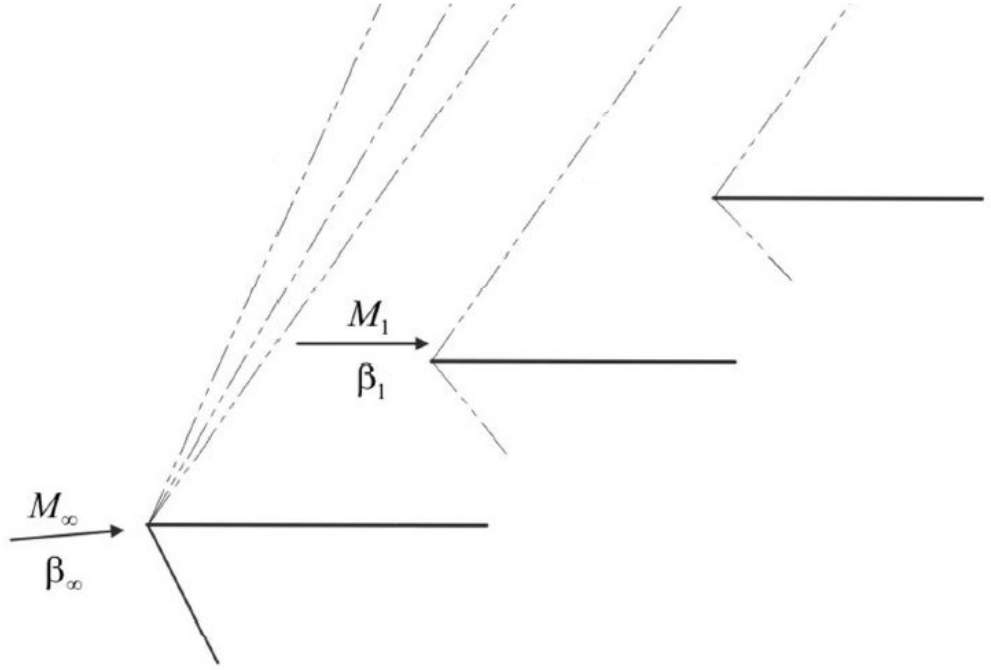

Figure 3.11: Semi-infinite flat-plate cascade at positive incidence

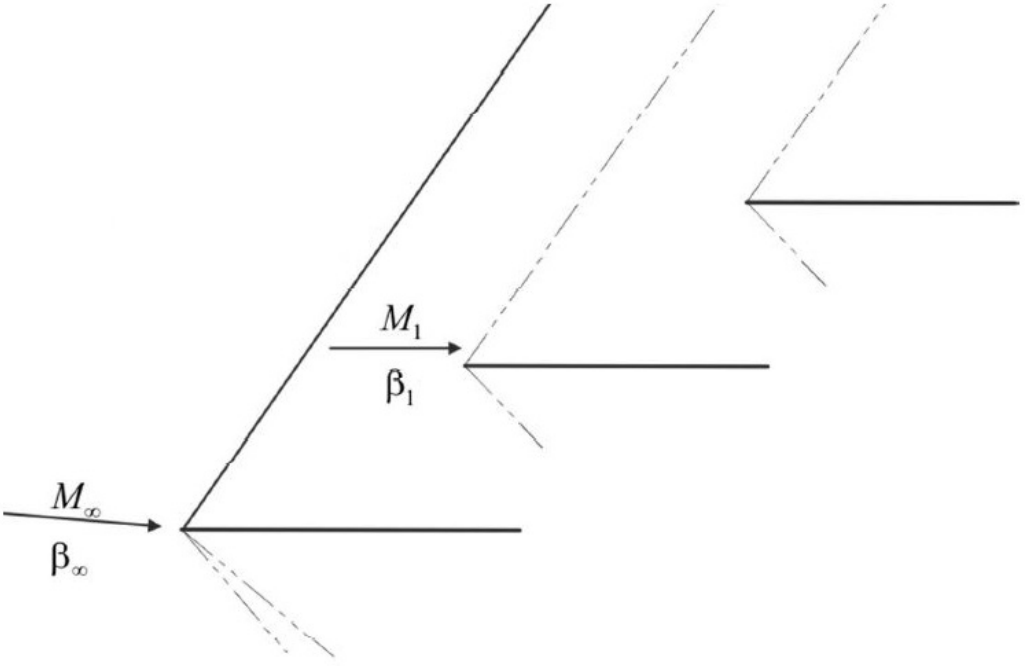

Figure 3.12: Semi-infinite flat-plate cascade at negative incidence

To further clarify, in a semi-infinite flat-plate cascade sorrounded by a uniform supersonic flow (M_∞,β_∞), with an inlet angle larger or smaller than the stagger angle β_s, a wave pattern occurs at the leading-edge of the first blade, which can be identified as the lowest blade in the pictures above. Depending on the incidence of the inlet flow relative to the cascade, the wave pattern at the leading-edge can be a Prandtl-Meyer expansion or a shock wave. If we consider a semi-infinite flat plate cascade introduced into a supersonic flow with positive incidence, the Prandtl-Meyer expansion accelarates the flow up to M_1 and turnes it of an angle equal to the blade direction, that is equal to the stagger angle ($\beta_1 = \beta_s$). Therefore, the flow in front of the second blade is no longer uniform, but satisfies the following condition (M_1,β_1). Since β_1 is equal to the direction of the flat-plate, that is the blade stagger angle, the flow is not deviated by the second blade and remains unchanged in direction. The result is that all the other blades see an approaching flow with an inlet angle β_1 and an inlet Mach number M_1. It can be noted that the first blade can be approached by an inlet flow with different incidence angles β_∞, while the other blades can be approached by a flow with only one inlet flow angle β_1, even if the uniform flow approaching the cascade can have any direction relative to the cascade. Hence, for all the blades except the first one, only the inlet flow Mach number M_1 can be varied, while the inlet flow angle remains the same.

Consider now an infinite flat-plate cascade, sketched in Figure 3.13, taken and adapted from [29]. In such a case, it is not possible to identify a first blade, so in this case only $\beta_\infty = \beta_1 = \beta_s$ and $M_\infty = M_1$ are possible. Thus, given the geometry of the cascade, for any given inlet Mach number, only one possible incidence can exist for the inlet flow, which in this case corresponds to the null incidence. In fact, the condition $\beta_1 = \beta_s$ is valid only for flat-plate blade profiles.

Finally, consider a supersonic cascade in a transonic/supersonic compressor rotor. An infinite cascade is the equivalent of the periodic annular cascade of an axial compressor. However, for the real case of a periodic cascade with finite thickness and camber in an axial supersonic compressor, the analysis is more complicated, but the conclusions are similar. In fact, given the geometry of the cascade, only one possible incidence can exist for any given supersonic inlet Mach number, and it is referred as *unique incidence*. In unique incidence operating condition, the cascade is choked. In fact, just one specific value of the mass flow corresponds to a given upstream Mach number, that is to each point (M,β) of the so-called *unique incidence curve*, which is a diagram reporting all the admissible inlet-flow conditions for a supersonic cascade.

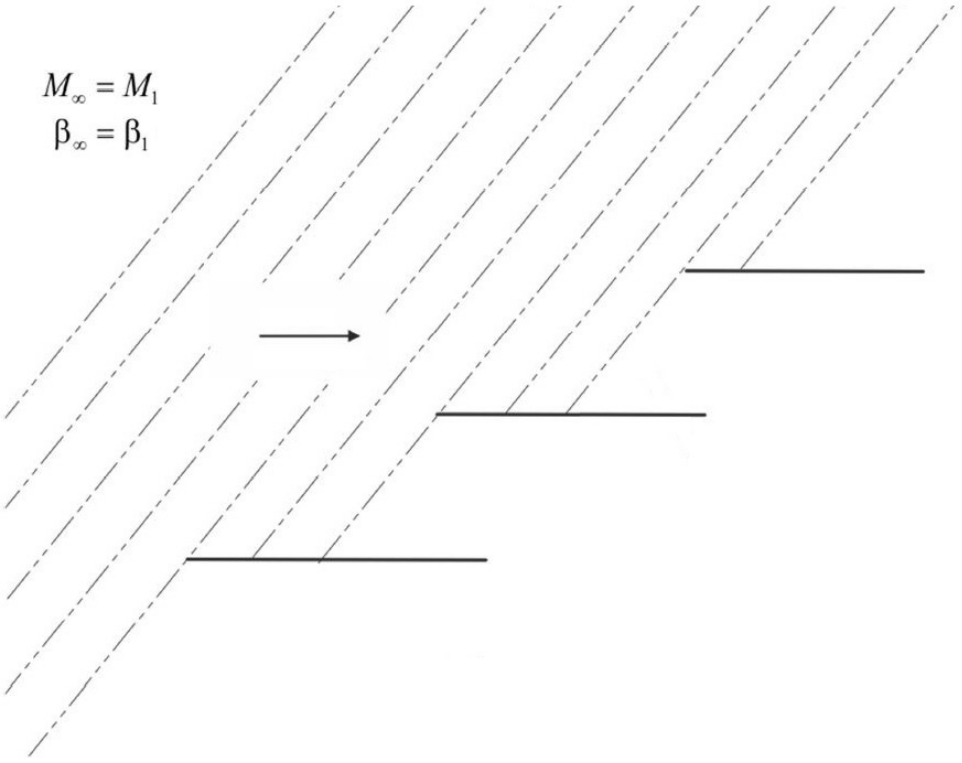

Figure 3.13: Infinite flat-plate cascade

Obviously, all the considerations above have been made without any specification concerning the blade passage, the blade thickness, and the blade curvature. These parameters deeply influence the inlet flow configuration in the region upstream of the cascade, the mass flow rate through the blade passage, and the shape of the unique incidence curve.

As stated at the beginning of this section, a wide qualitative analysis of the supersonic inlet flow for a cascade is reported in [17]. Different inlet flow conditions are described for cascades with both straight and cambered suction sides, that is for a flat-plate cascade and for cascades of cambered profiles with sharp leading edge, such as circular arc and pre-compression (or external compression) blade cascades. The cascade inlet-flow behaviour, as stated before, is reported in a diagram in which the inlet flow angle β_∞ is plotted as a function of the inlet flow Mach number M_∞. The shape of the unique incidence curve for an infinite flat-plate cascade is sketched in Figure 3.14, taken from [17].

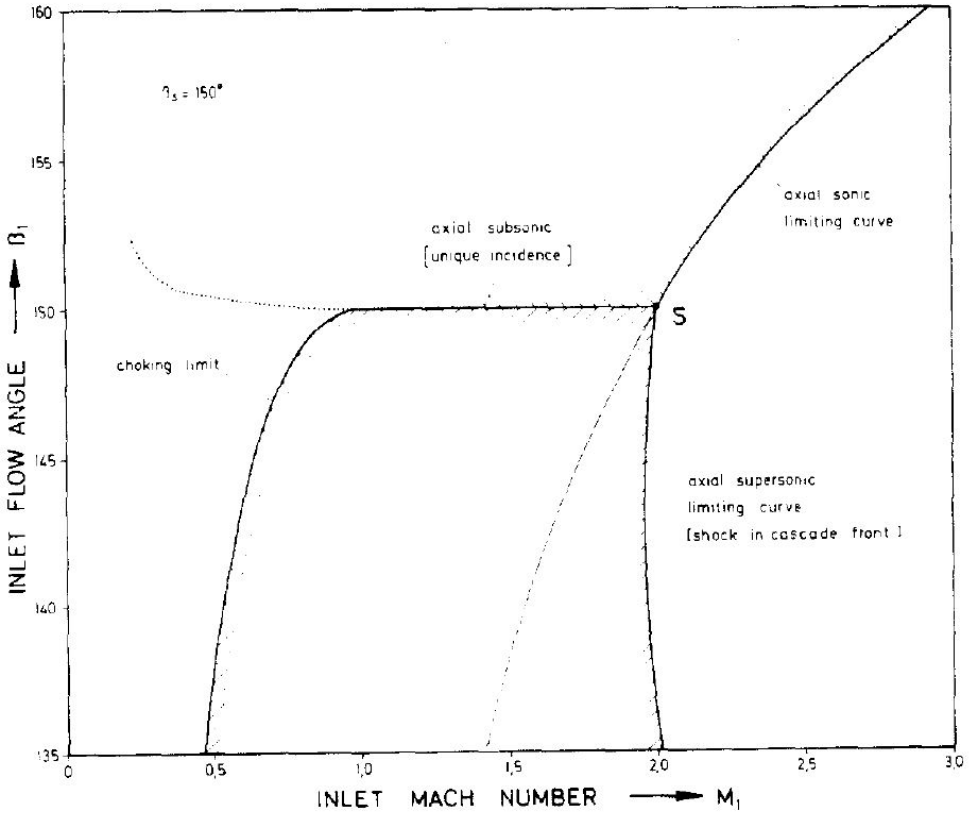

Figure 3.14: Unique incidence curve for a flat-plate cascade

The shape of the unique incidence curve for a real supersonic cascade, that is for a cascade of cambered profiles with sharp leading edge, is similar to the ones sketched in Figure 3.15 and in Figure 3.16, taken from [17]. In Figure 3.15 is depicted the unique incidence curve characteristic of a circular arc profiles cascade; in Figure 3.16 is reported the shape of the unique incidence curve for a cascade made of profiles with concave suction sides (S-shape airfoils). As can be noted, the shape of the cascade airfoils deeply influences the shape of the unique incidence curve. This difference is due to the different inlet flow in the region upstream of the cascade. In fact, the blunt leading edge gives rise to a detached bow shock in front of the blade, which extends both inside the blade passage and out in front of the cascade, affecting the incoming flow upstream of the other blades, since the cascade is periodic. In a precompression airfoils cascade, as described before, the concave portion of the suction side in the forward part, produces a series of compression waves. The coalescence of these compression waves forms a precompression shock which intersects the detached bow shock of the adjacent blade. Moreover, an expansion fan occurs between the detached bow shock at the leading edge and the compression waves. The phenomena just described, which characterize the inlet flow in the upstream region of the cascade, cause the difference in shape between the unique incidence curve for a flat-plate cascade and the unique incidence curve for a cascade of real profiles. The most important result which derives from the difference in the shape between the unique incidence curve for a flat-plate cascade and the unique incidence curve for a real cascade is that for a flat-plate cascade the unique incidence condition allows to vary the inlet Mach number and, as consequence, the mass flow rate without affecting the incidence of the approaching flow, while in a real cascade changing the inlet Mach number affects also the inlet flow angle. Thus, the elaborated mass flow rate can be changed only by modifying both the inlet Mach number and the inlet flow angle. Further detailed qualitative explanations of the unique incidence condition for a supersonic cascade are available in other references, such as [5], [14], and [19].

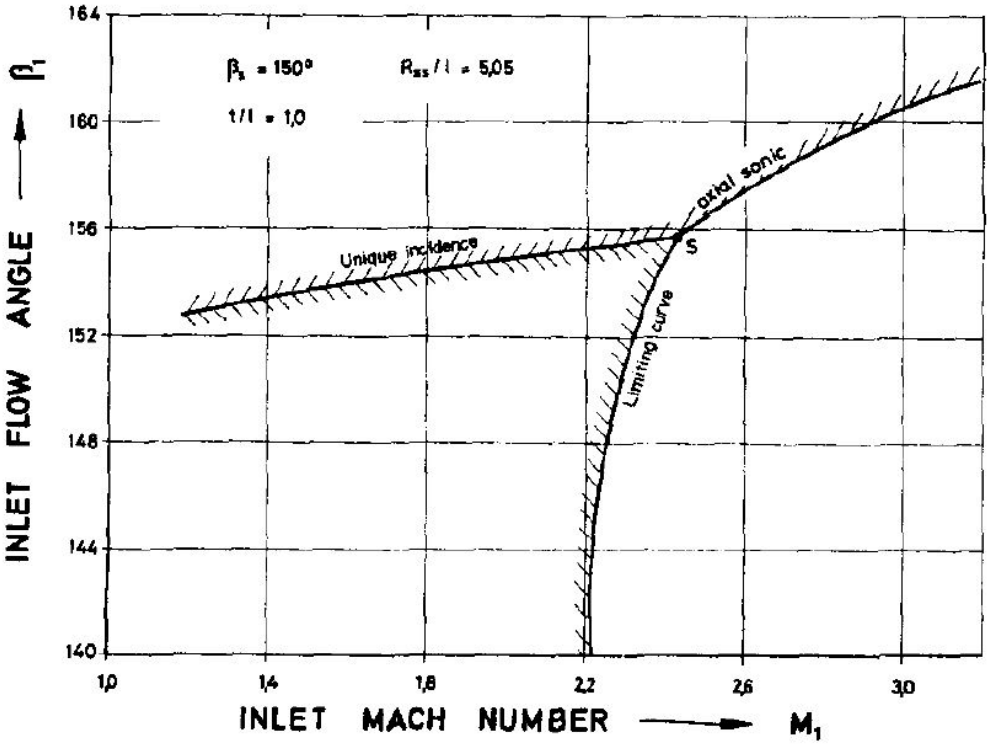

Figure 3.15: Unique incidence curve for a circular arc profiles cascade

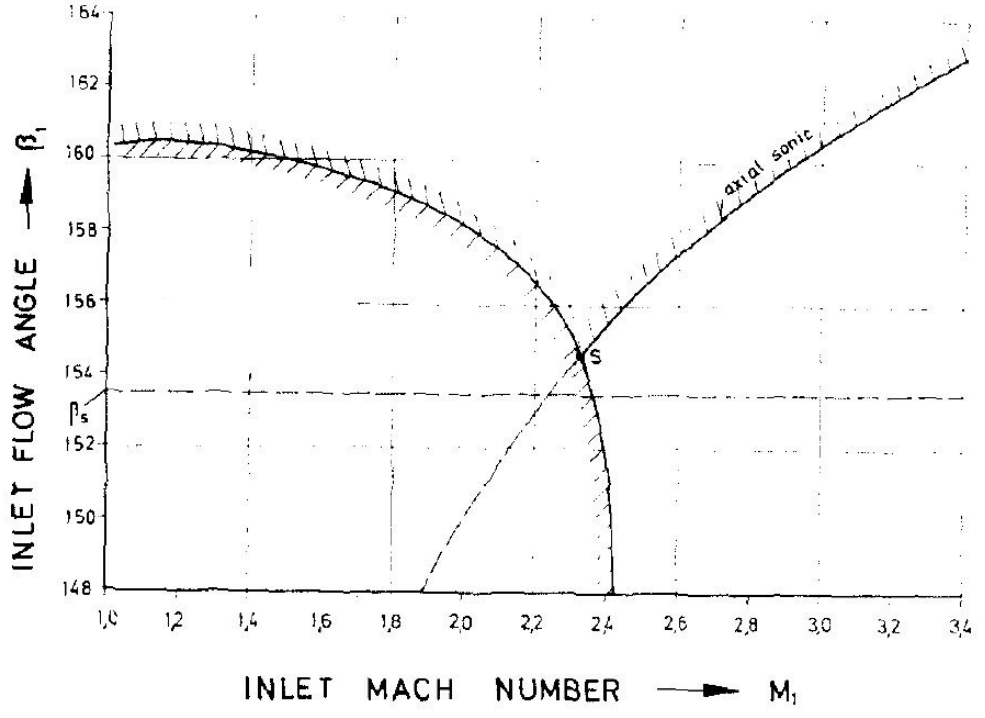

Figure 3.16: Unique incidence curve for a precompression airfoils cascade

3.6.1 Unique incidence determination

A rigorous mathematical derivation of the equations governing the unique incidence operating condition for a supersonic compressor cascade is far beyond the scope of this work. However, by using the equations derived in the previous chapters and adopting a proper set of simplifying assumptions, a brief description of the main relations at the basis of this particular operating condition, peculiar to supersonic compressor cascades, can be carried out. The literature concerning the unique incidence condition for a supersonic cascade is wide and exhaustive. For example, the development of an analytical model, usually referred as "simple wave model", for determining the inlet flow condition in a supersonic cascade can be found in [15] and in [17]. The approximate solution obtained through this method is valid for profiles with sharp leading edge and attached shocks. In [33], an inviscid method, neglecting the boundary layer and viscous effects, is developed for analyzing the flow in the entrance region of a cascade. In contrast to the previous method, it is valid for both attached and detached shocks. Other papers also provide semi-empirical models to investigate the supersonic inlet flow approaching a cascade. The analysis developed hereunder takes as its starting point the analytical method developed in [15] and reported in [14] and [17]. For a mathematical discussion of the unique incidence condition under a different point of view, refer to [5].

The problem that must be solved, known as the *entrance problem*, consists on the determination of the incidence of the supersonic undisturbed flow with axial subsonic component approaching a cascade, given the upstream Mach number M_∞, the cascade geometry, and a suitable static pressure ratio p_2/p_1. Consider an infinite linear supersonic compressor cascade, representing the annular cascade of a supersonic compressor rotor, that is equivalent to the two-dimensional array of compressor rotor blade sections. Consider the cascade introduced into a uniform supersonic flow with subsonic axial Mach number, approaching with positive incidence, as sketched in Figure 3.17 (taken and modified from [19]). The geometry of the cascade is given in terms of the stagger angle β_s, the solidity $\sigma = c/s$, the cascade pitch s, and the shape of the profiles $y = f(x)$. As stated before, for a flat-plate cascade, sketched on the left in Figure 3.17, an expansion fan occurs in the region in front of the cascade, which turns the flow into the flat plate direction. In other words, the flow is turned by the expansion waves of an angle equal to the stagger angle, $\beta_1 = \beta_s$.

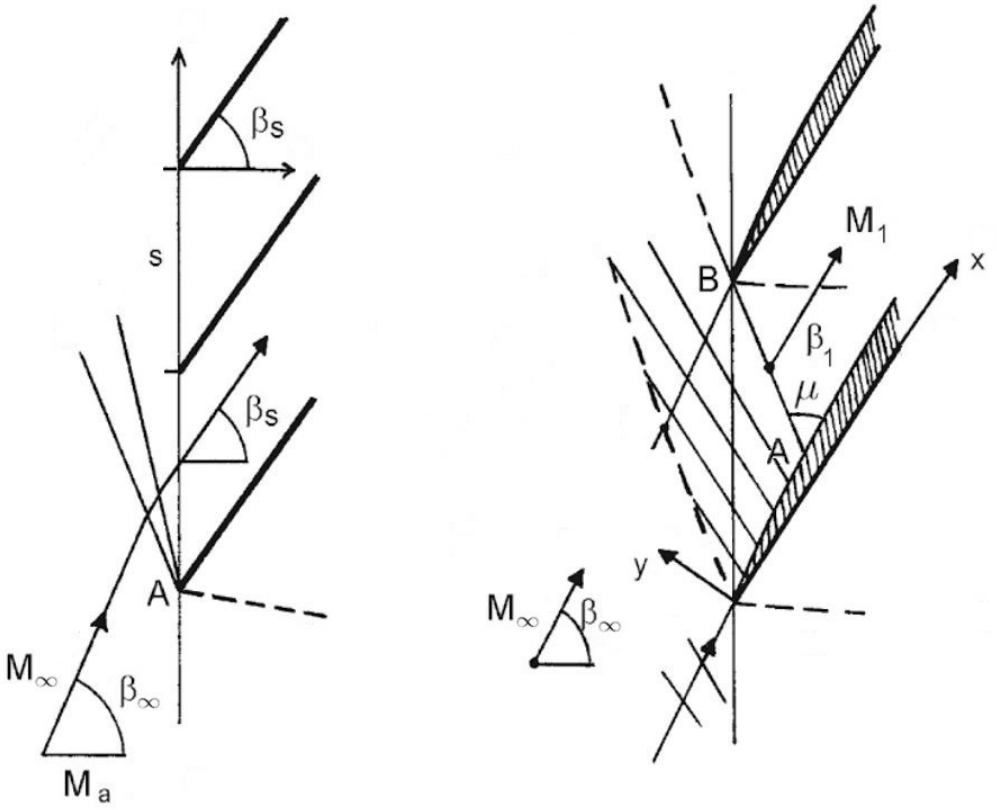

Figure 3.17: Inlet flow in unique incidence condition: flat-plate cascade and real cascade with generic airfoils

Conversely, for a cascade of an axial compressor, sketched on the right in Figure 3.17, the finite thickness of the leading edge and the camber of the suction side give rise to a detached bow shock in front of the profile. In order to simplify the subsequent discussion, consider the leading edge sharp enough in such a way that the shock wave is attached and sufficiently weak. Hence, the oblique bow shock in front of the leading-edge may be neglected. Adopting this simplification, the region downstream of the bow shock can be described by Equation (2.80) and the Prandtl-Meyer relation, that is Equation (2.82), as if it were characterized only by an expansion fan

$$\nu(M) + \beta = const \tag{3.23}$$

$$\nu(M) = \sqrt{\frac{\gamma+1}{\gamma-1}} tan^{-1}\left[\frac{\gamma-1}{\gamma+1}(M^2-1)\right] - tan^{-1}(\sqrt{M^2-1}) \tag{3.24}$$

Consider the line AB as a reference section for describing the conditions at the passage entrance. The line AB corresponds to the Mach wave departing from the suction side of the lower blade (point A) and intersecting the adjacent blade at the leading-edge (point B), forming a wave angle μ. Refer to the upstream conditions at infinity with subscript

∞, and to the conditions along the line AB, that is just ahead the blade passage, with subscript 1. Thus, the Mach number and the angle of the undisturbed flow are M_∞ and β_∞, respectively. The inlet Mach number M_∞ is known, as stated before. Initially, the point A (x_A,y_A) on the suction side and, as a consequence, the associated Mach wave departing from it, can be arbitrarly estimated. The Mach number M_1 at the passage entrance is assumed to be constant along the line AB and the flow direction can be assumed parallel to the surface of the profile, that is inclined as the slope of the suction side in point A. By geometric relations, the flow direction β_1 along the line AB and the wave angle μ can be determined, since the geometry of the blade is given. Moreover, the Mach number M_1 along the line AB can be easily calculated, since it is related to μ by the following relation

$$\sin\mu = \frac{1}{M_1} \tag{3.25}$$

which is valid for a Mach wave propagating inside the flow. Once an initial value of M_1 is estimated, the procedure for the calculation of the inlet flow angle β_∞ is as follows.
The Prandtl-Meyer relation, also known as the Riemann invariant, must be valid between the upstream flow region at infinity and the region at the entrance of the cascade passage

$$\nu(M_\infty) + \beta_\infty = \nu(M_1) + \beta_1 \tag{3.26}$$

where β_1 is the flow direction at the passage entrance along the line AB, parallel to the suction side, and ν is the Prandtl-Meyer function given by Equation (3.24). Now, β_1 is known from the geometry of the blade and $\nu(M_1)$ is known once M_1 has been calculated; so the unknowns in Equation (3.26) are M_∞ and β_∞. Thus a further equation for the calculation of the unknowns must be written. Together with the Prandtl-Meyer relation, the mass flow conservation must be satisfied in the region between upstream and the line AB. Therefore, consider the mass flow continuity equation

$$\rho_\infty u_\infty A_\infty = \rho_1 u_1 A_1 \tag{3.27}$$

where

$$A_\infty = s\cos\beta_\infty \tag{3.28}$$

is the area of the section normal to the upstream flow and

$$A_1 = l\sin\mu \tag{3.29}$$

is the area of the section normal to the mean flow inside the passage. l is the length of

the line AB, that is the distance between point A and the leading edge of the adjacent blade. The value of l can be determined from the cascade geometry and the coordinates of the point A (x_A,y_A)

$$l^2 = (s\cos\beta_s - y_A)^2 + (-s\sin\beta_s - x_A)^2 \tag{3.30}$$

Since the flow is assumed to be isentropic, the continuity equation can be written in the following form, derived from one-dimensional gasdynamics [4]

$$F = \frac{\dot{m}}{A} = \sqrt{\frac{\gamma}{RT_0}}p_0 \frac{M}{\sqrt{\left(1+\frac{\gamma-1}{2}M^2\right)^{\frac{\gamma+1}{\gamma-1}}}} \tag{3.31}$$

Thus, the continuity equation is of the form

$$\frac{A_\infty}{A_1} = \frac{F(M_1)}{F(M_\infty)} \tag{3.32}$$

Moreover, since the flow can be considered adiabatic and isentropic, because the shocks are assumed to be weak and friction is neglected, the total temperature T_o is constant and the total pressure p_o is almost constant. Thus, the continuity equation, expanding both the left-hand side and the right-hand side and simplifying, is

$$\frac{M_\infty\cos\beta_\infty}{\sqrt{\left(1+\frac{\gamma-1}{2}M_\infty^2\right)^{\frac{\gamma+1}{\gamma-1}}}} = \frac{l}{s}\frac{M_1\sin\mu}{\sqrt{\left(1+\frac{\gamma-1}{2}M_1^2\right)^{\frac{\gamma+1}{\gamma-1}}}} \tag{3.33}$$

where

$$\frac{l}{s} = \sqrt{\left(\cos\beta_s - \frac{y_A}{s}\right)^2 + \left(-\sin\beta_s - \frac{x_A}{s}\right)^2} \tag{3.34}$$

The equations that must be satisfied from infinitely far upstream to the cascade entrance region are then Equation (3.26) and Equation (3.33). M_∞ and β_∞ can be determined solving Equation (3.26) and Equation (3.33), beginning with an initial estimation of point A, since the values of β_s and s are known from the cascade geometry, μ and M_1 are assumed known at the entrance location once the point A has been choosen, l depends on the coordinates of the point A and is determined by Equation (3.30), and A_1 is known once l has been calculated. If the computed inlet Mach number is not equal to the given Mach number M_∞, fixed by the inlet conditions, a new point A and, as a consequence, a

new value of M_1 and β_1 must be choosen. Thus, if M_1 is assumed known and M_∞ is fixed by the inlet conditions, only one value of β_∞ satisfies simultaneously the Prandtl-Meyer relation and the mass flow continuity equation. For that reason, the incidence is unique

$$\beta_\infty = f(M_\infty, M_1, \beta_1, \beta_s, s) \tag{3.35}$$

As it can be seen, the inlet flow angle is expressed as a function of: the inlet Mach number M_∞, that must be choosen within a range of Mach numbers admissible for the cascade; the geometry of the cascade through β_s and s; the geometry of the profiles; the flow field from dowstream of the bow shock at the leading-edge to the covered passage entrance, by the Mach wave departing from the point A. Since Equation (3.26) and Equation (3.33) are two independent equations for one unknown, that is β_∞, these equations can only be satisfied for a particular value of β_∞ once M_∞ is given, that is for only one particular combination of (M_∞,β_∞). In this sense the incidence is unique, because only one value of β_∞ is related to a given Mach number M_∞, once the cascade geometry is fixed. The combination of values (M_∞,β_∞) is determined iteratively through the procedure just described. The flow chart in Figure 3.18 summarizes the logical process which leads to the determination of the unique incidence condition.

As has been seen, in a real cascade the inlet flow angle depends on the stagger angle β_s, the blade curvature and thickness, and the cascade pitch s. All the considerations above have been made neglecting any influence of viscosity and considering cascade blades with a sharp leading-edge, that is supposing the shock waves ahead of the blades attached and sufficiently weak, even if in a real cascade the shocks are curved and detached and the leading-edge of the blade section is blunt. Moreover, the above analysis has been carried out taking into account only the shrinking of the blade passage due to the finite thickness of the blade, and not the reduction of the passage due to the thickness of the boundary layer on the blade surfaces. The particular pair of values (M_∞,β_∞), which satisfies Equation (3.26) and Equation (3.33), determines a specific value of the mass flow rate. By the continuity equation, the mass flow rate through a section normal to the flow at infinity must corresponds to the mass flow rate elaborated by the cascade passage: thus, for a given upstream Mach number M_∞, this occurs only for a particular value of β_∞. Hence, in unique incidence operating conditions, the flow is choked: the mass flow rate is maximum and depends on the blade passage area. The mass flow rate is fixed, since the incidence cannot change without affecting the inlet Mach number or viceversa, and a specific value of the mass flow rate corresponds to each point of the unique incidence curve, that is to each combination of values (M_∞,β_∞) within the operating range of the cascade.

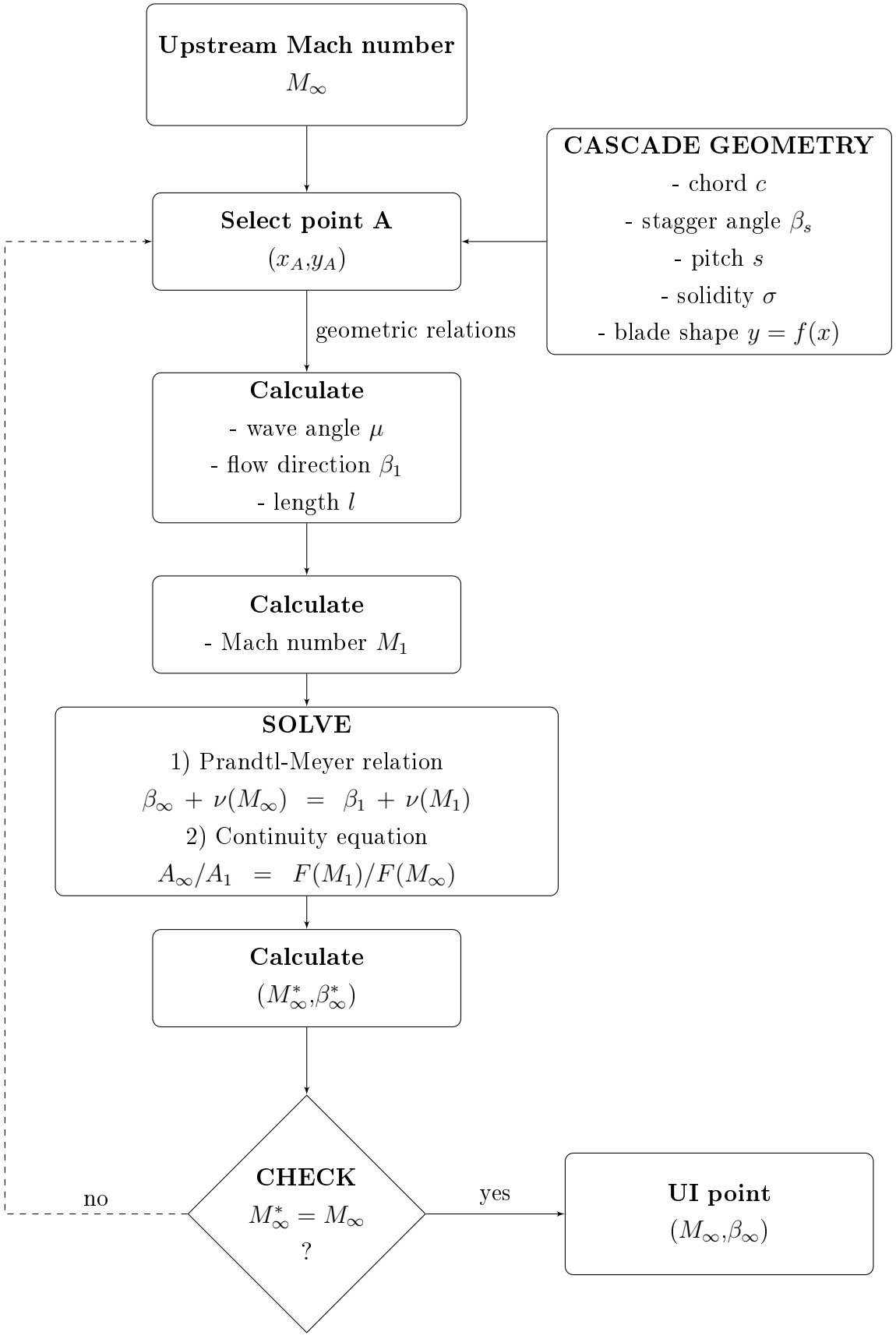

Figure 3.18: Flow chart for the analytical determination of the unique incidence condition

In unique incidence conditions, the upstream flow is not influenced by the presence of the cascade or by the downstream region, that is by any change in static backpressure. In fact, any change in static backpressure affects only the shock pattern inside the blade passage, while the upstream flow field is not influenced, as stated before. In unique incidence operating condition, the exit flow, in terms of exit flow angle and exit Mach number, depends on the backpressure. An increase in static backpressure forces the shock waves inside the blade passage to move towards the passage entrance. The condition in which a quasi-normal shock occurs exactly at the passage entrance represents the highest static pressure ratio obtainable for a supersonic compressor cascade operating in unique incidence at a given inlet Mach number.
If the static backpressure raises over the highest allowable static pressure ratio, a detached shock in front of the leading-edge occurs. This condition is referred as *unstarted* or *spill condition*. In this case, the unique incidence is no longer valid and a new relation between inlet Mach number and inlet flow angle is established, which is parametric with the static backpressure

$$\beta_\infty = f(p_2/p_1) \tag{3.36}$$

In this condition, small changes of inlet flow incidence can be pursued in order to change the mass flow rate, since a small subsonic region in front of the leading edge allows the flow field to adapt to the geometry of the passage. However, transonic and supersonic cascades can whitstand only modest regulations in incidence, before the stall occurs, and the mass flow rate depends on the passage area. Moreover, in transonic regime, small variations in geometry cause great changes in the flow field: the thickening of the boundary layer, due to the strong shock wave-boundary layer interaction, determines a reduction of the effective area of the passage and, as a consequence, of the maximum mass flow rate.

Chapter 4

Fundamentals of CFD and turbulence models

In this chapter a brief description of the turbulence models employed in computational fluid dynamics (CFD) to solve turbulent flows for engineering problems is presented. This chapter focuses on a brief derivation of the equations employed in the numerical solution of turbulent flows, known as the *Reynolds Averaged Navier-Stokes (RANS) Equations*, and on the four main turbulence models implemented in the commercial solver ANSYS® Fluent, highlighting some of their major characteristics, which will be useful for the subsequent discussions. The turbulence models described below are presented in order of increasing complexity. For the implementation peculiarities and further theoretical backgrounds of the turbulence models available in ANSYS® Fluent, refer to the ANSYS® Fluent Theory Guide [7]. For the complete theory of turbulence, refer to [20] instead.

4.1 Turbulent flows and Reynolds number

Turbulence is defined as an unsteady and chaotic motion of a fluid, characterized by vortices of various sizes, referred as turbulent structures. Giving no further details for the sake of brevity, the majority of engineering flows are turbulent and an important dimensionless quantity used to determine whether a flow is turbulent, is the *Reynolds number*, defined as follows

$$Re = \frac{\rho u L}{\mu} = \frac{u L}{\nu} \tag{4.1}$$

where

- ρ is the density of the fluid $[kg/m^3]$

- u is the velocity of the flow $[m/s]$
- L is a characteristic dimension $[m]$ (in this case the chord of the airfoil)
- μ is the dynamic viscosity $[Ns/m^2]$
- ν is the kinematic viscosity $[m^2/s]$

Generally speaking, the Reynolds number of a supersonic flow in a wind tunnel facility test is typically of the order of 10^6, based on the airfoil chord and the inlet air velocity.

4.2 Numerical simulations of turbulent flows

To numerically solve turbulent flows, three approaches are available:

- DNS (Direct Numerical Simulation). This method consists of solving directly the complete Navier-Stokes equations for the problem considered. This means that the whole range of turbulent structures, from the smallest to the largest ones, must be solved. It can be demonstrated that for a three-dimensional problem the number of mesh points must be

$$N_p^3 \geq Re^{9/4} \tag{4.2}$$

and the number of time steps must be

$$N_{\Delta t} \sim Re^{1/2} \tag{4.3}$$

Hence, the computational cost of DNS is huge and can be estimated growing as Re^3. Since the computational cost is too prohibitive, direct numerical simulation is not useful for industrial and engineering applications.

- RANS (Reynolds Averaged Navier-Stokes). This technique solves a time-averaged form of the Navier-Stokes equations, called RANS, reducing in this way the overall computational cost. This is the most widely used approach for engineering problems. However, it requires additional models to solve the so-called "problem of closure", related to the mathematical derivation of the RANS equations, which will be briefly described below.

- LES (Large Eddy Simulation). This method solve a filtered form of the Navier-Stokes equations, considering the largest turbulent structures and ignoring the smallest ones, whose numerical solution is the most computationally expensive.

4.3 Reynolds Averaged Navier-Stokes (RANS) Equations

The Navier-Stokes equations for an incompressible flow can be written in vector notation as follows

$$\nabla \cdot \overline{v} = 0 \tag{4.4a}$$

$$\frac{D}{Dt}\overline{v} = -\frac{1}{\rho}\nabla p + \nabla \cdot (2\nu\overline{\overline{e}}) \tag{4.4b}$$

where $\overline{\overline{e}}$ is the strain rate tensor

$$\overline{\overline{e}} = \frac{1}{2}(\nabla\overline{v} + \nabla\overline{v}^T) \tag{4.5}$$

Velocity can be decomposed as the sum of two terms

$$\overline{v}(\overline{r},t) = \langle\overline{v}(\overline{r},t)\rangle + \overline{v}'(\overline{r},t) \tag{4.6}$$

where $\langle\overline{v}(\overline{r},t)\rangle$, or $\overline{V}(\overline{r},t)$, is the mean velocity, which describes the mean flow field and is independent of time, and $\overline{v}'(\overline{r},t)$ the fluctuating part, which depends on time and is related to the instantaneous variations of the flow field. This decomposition is called the *Reynolds decomposition*. The average velocity is defined by the *ensamble average*

$$\overline{V}(x) = \langle v(r,t)\rangle = \lim_{N\to\infty}\frac{1}{N}\sum_{n=1}^{N} v^{(n)}(r,t) \tag{4.7}$$

where n denotes the nth repetition of a turbulent-flow experiment, or by the *time average*

$$\overline{V}(x) = \langle v(r,t)\rangle = \lim_{T\to\infty}\frac{1}{T}\int_T v(r,t)dt \tag{4.8}$$

For a steady omogeneous turbulent flow, the previous definitions are coincident. It can be demonstrated that the continuity equation and the momentum equation become

$$\nabla \cdot \overline{V} = 0 \tag{4.9a}$$

$$\frac{D}{Dt}\overline{V} = -\frac{1}{\rho}\nabla p + 2\nu\nabla\cdot\overline{\overline{E}} - \nabla\cdot\langle\overline{v}'\overline{v}'\rangle \tag{4.9b}$$

where $\overline{\overline{E}}$ is the mean strain rate tensor. These equations are called the *Reynolds Averaged Navier-Stokes (RANS) Equations*. For simplicity, the rigorous mathematical derivation of these equations has been omitted. The term $\langle\overline{v}'\overline{v}'\rangle$ on the right-hand side of the momentum

equation, is the *Reynolds stress tensor*. The RANS equations form a system of four equations, that is the continuity equation and the three scalar equations for momentum, with ten unknowns, that is p, $\overline{V}$, and six components of the Reynolds stress tensor

$$\langle \overline{v}'\overline{v}' \rangle = \begin{bmatrix} \langle \overline{u}'^2 \rangle & \langle \overline{u}'\overline{v}' \rangle & \langle \overline{u}'\overline{w}' \rangle \\ \langle \overline{u}'\overline{v}' \rangle & \langle \overline{v}'^2 \rangle & \langle \overline{v}'\overline{w}' \rangle \\ \langle \overline{u}'\overline{w}' \rangle & \langle \overline{v}'\overline{w}' \rangle & \langle \overline{w}'^2 \rangle \end{bmatrix} \tag{4.10}$$

which is a symmetric tensor. So, the four equations written above are not enough to solve the problem, since there are more than four unknowns, because of the appearance of the Reynolds stresses. This issue leads to the problem of closure, which can be resolved by using the so-called *turbulence models*.

4.4 Turbulence models

As just stated, in order to solve the RANS Equations, it is necessary to adopt a turbulence model to close the problem. The Reynolds stress tensor is symmetric and can be identified as a *turbulent stress tensor*. It can be modelled in a similar way as the *viscous stress tensor* written as follows

$$\frac{\overline{\overline{T}}}{\rho} = -\frac{p}{\rho}\overline{\overline{I}} + 2\nu\overline{\overline{E}} \tag{4.11}$$

that is

$$-\langle \overline{v}'\overline{v}' \rangle = -\frac{2}{3}k\overline{\overline{I}} + 2\nu_T\overline{\overline{E}} \tag{4.12}$$

where ν_T is the *turbulent viscosity* and k is the *turbulent kinetic energy*. The turbulent kinetic energy is defined as half of the trace of the Reynolds stress tensor

$$k = \frac{1}{2}tr(\langle \overline{v}'\overline{v}' \rangle) \tag{4.13}$$

Assuming that the Reynolds stress tensor can be expressed as a function of the mean strain rate tensor by means of the parameter ν_T, that is writing the term $2\nu_T\overline{\overline{E}}$, corresponds to applying the so-called *Boussinesq's hypothesis*. Hence, we can write

$$\frac{D}{Dt}\overline{V} = -\nabla\left(\frac{p}{\rho} + \frac{2}{3}k\right) + \nabla \cdot [2(\nu + \nu_T)\overline{\overline{E}}] \tag{4.14}$$

The problem is now closed, but ν_T needs to be modeled, since it is the only unknown remaining. The most widely used turbulence models are *one-equation models* or *two-*

equations models, depending on the turbulence quantities considered and on the model transport equations used for their description. The software used for the CFD calculations, ANSYS® Fluent, allows for a quite wide choice of turbulence models.

4.4.1 The Spalart-Allmaras model

The first turbulence model discussed here is the *Spalart-Allmaras* (S-A) *model*. It is a one-equation model which solves a single model transport equation for the turbulent viscosity ν_T. The model equation for ν_T is of the form

$$\frac{D\nu_T}{Dt} = \nabla \cdot \left(\frac{\nu_T}{\sigma_\nu} \nabla \nu_T \right) + S_\nu \tag{4.15}$$

where the source term S_ν depends on various quantities, such as the laminar and turbulent viscosities, ν and ν_T, and the turbulent viscosity gradient $|\nabla \nu_T|$.
In ANSYS® Fluent, the implemented transport equation for ν_T is of the form

$$\frac{D\nu_T}{Dt} = G_{\nu_T} + \frac{1}{\sigma_{\nu_T}} \left[\nabla \cdot (\nu_T \nabla \nu_T) + C_{b2} (\nabla \nu_T)^2 \right] - Y_{\nu_T} + S_{\nu_T} \tag{4.16}$$

where G_{ν_T} is the production of turbulent viscosity and Y_{ν_T} is the destruction of turbulent viscosity. σ_{ν_T} and C_{b2} are constants and S_{ν_T} is a source term. The equation for the Spalart-Allmaras model written above is obviously a simplified form of the equation commonly implemented and it has been reported just for the sake of completeness. Since the details of the model are quite complicated, refer to the original paper [26] and to the ANSYS® Fluent Theory Guide [7] for further developments.
The Spalart-Allmaras model has been developed mainly for aerodynamic and turbomachinery applications, such as supersonic and transonic flows over airfoils with mild boundary-layer separation. It showed good results in solving boundary layers subjected to adverse pressure gradients.

4.4.2 The k-ε model

As stated above, the two-equations models used to solve the turbulence closure problem are so called because two model transport equations are solved for as many turbulence quantities. Most frequently, one of the two turbulence variables employed in the most common two-equations models is the turbulent kinetic energy k, while the second turbulence quantity depends on the type of the two-equations model considered. Generally speaking, these models provide more accurate solutions, even if calculation time and computational

cost per iteration increase. The quantities of most considerable importance for describing the processes in turbulent flows are the already mentioned *turbulent kinetic energy* k; the *dissipation of turbulent kinetic energy* ε, or simply *dissipation*, defined as

$$\varepsilon = 2\nu\langle\overline{\overline{e'}} : \overline{\overline{e'}}\rangle \tag{4.17}$$

where $\overline{\overline{e'}}$ is the fluctuating strain rate tensor; and the *production of turbulent kinetic energy* P, or simply *production*, defined as

$$P = -\langle\overline{v}'\overline{v}'\rangle : \nabla\overline{V} \tag{4.18}$$

The first two-equations model described here is the *Standard (STD) k-ε model*. This turbulence model solves a model transport equation for k and a model transport equation for ε, specifying the turbulent viscosity ν_T as follows

$$\nu_T = C_\mu \frac{k^2}{\varepsilon} \tag{4.19}$$

where $C_\mu = 0.09$ is an empirical constant. The problem is closed and it can be solved once ε and k are specified with proper equations.
The standard model transport equation for k is of the form

$$\frac{\partial k}{\partial t} + \overline{V}\cdot\nabla k = \nabla\cdot\left[\left(\frac{\nu_T}{\sigma_k}\right)\nabla k\right] + P - \varepsilon \tag{4.20}$$

where

$$\sigma_k = 1.0$$

The model transport equation for ε is of the form

$$\frac{\partial \varepsilon}{\partial t} + \overline{V}\cdot\nabla\varepsilon = \nabla\cdot\left[\left(\frac{\nu_T}{\sigma_\varepsilon}\right)\nabla\varepsilon\right] + C_{\varepsilon 1}\frac{P\varepsilon}{k} - C_{\varepsilon 2}\frac{\varepsilon^2}{k} \tag{4.21}$$

where the constants are

$$C_{\varepsilon_1} = 1.44 \qquad C_{\varepsilon_2} = 1.92 \qquad \sigma_\varepsilon = 1.3$$

The standard k-ε model is the simplest two-equations turbulence model available. It is implemented in a wide range of CFD codes and solvers and it is the main turbulence model employed in industrial and engineering applications. Generally speaking, it is robust and reasonably accurate, even if it can provide poor results for flows with strong

boundary layer separation and for flows with large adverse pressure gradients.
In ANSYS® Fluent the k-ε model is available in three different forms: the already mentioned Standard (STD) k-ε model and two improved variants of the base model, the RNG k-ε model and the REALIZABLE k-ε model. The equations for each model are reported below just for the sake of completeness, since the details behind the implementation of these turbulence models are far beyond the scope of this work. For further details concerning the main differences among the three formulations of the k-ε model, refer to the ANSYS® Fluent Theory Guide [7]. The transport equations for k and ε for the STD k-ε model implemented in ANSYS® Fluent can be written in a simplified form as follows

$$\frac{Dk}{Dt} = \nabla \cdot \left[\left(\frac{\nu_T}{\sigma_k} \right) \nabla k \right] + G_k - \varepsilon + S_k - Y_M \tag{4.22}$$

$$\frac{D\varepsilon}{Dt} = \nabla \cdot \left[\left(\frac{\nu_T}{\sigma_\varepsilon} \right) \nabla \varepsilon \right] + C_{\varepsilon 1} \frac{\varepsilon}{k} G_k - C_{\varepsilon 2} \frac{\varepsilon^2}{k} + S_\varepsilon \tag{4.23}$$

where S_k and S_ε are source terms, G_k is the generation of turbulent kinetic energy, and Y_M is a term which takes into account the effects of compressibility for supersonic flows.

4.4.3 The RNG k-ε model

The *RNG k-ε model* is mathematically derived from the standard k-ε model. Without giving too much details, compared to the standard model, in the RNG k-ε model the transport equation for ε is implemented in a modified form

$$\frac{D\varepsilon}{Dt} = \nabla \cdot \left[\left(\frac{\nu_T}{\sigma_\varepsilon} \right) \nabla \varepsilon \right] + C_{\varepsilon 1} \frac{\varepsilon}{k} G_k - C^*_{\varepsilon 2} \frac{\varepsilon^2}{k} + S_\varepsilon \tag{4.24}$$

and the model constants are different from those in the standard k-ε model.

4.4.4 The REALIZABLE k-ε model

The *REALIZABLE k-ε model* differs from the standard k-ε model in the definiton of the turbulent viscosity (the constant C_μ is now computed) and in the form of the transport equation for ε, which is

$$\frac{D\varepsilon}{Dt} = \nabla \cdot \left[\left(\frac{\nu_T}{\sigma_\varepsilon} \right) \nabla \varepsilon \right] + C_1 S \varepsilon - C_2 \frac{\varepsilon^2}{k + \sqrt{\nu \varepsilon}} + S_\varepsilon \tag{4.25}$$

4.4.5 The k-ω model

The second two-equations model is the k-ω *model*, which solves a model transport equation for k and a model transport equation for the *specific dissipation* ω, or *dissipation per unit turbulence kinetic energy*, which is another turbulence quantity defined as follows

$$\omega = \frac{\varepsilon}{k} \tag{4.26}$$

Introducing Equation (4.26) into Equation (4.19), the turbulent viscosity becomes

$$\nu_T = C_\mu \frac{k^2}{\varepsilon} = C_\mu k \frac{k}{\varepsilon} = C_\mu \frac{k}{\omega} \tag{4.27}$$

The model transport equation for k is the same described in the previous section. The equation for ω is assumed to have the same form of the equation for ε

$$\frac{\partial \omega}{\partial t} + \overline{V} \cdot \nabla \omega = \nabla \cdot \left[\left(\frac{\nu_T}{\sigma_\omega} \right) \nabla \omega \right] + C_{\omega 1} P \frac{\omega}{k} - C_{\omega 2} \omega^2 \tag{4.28}$$

Generally speaking, the k-ω model is more accurate in solving the boundary layer, and performs satisfactorily for flows under adverse pressure gradients with boundary layer separation.

4.4.6 The SST k-ω model

An improved version of the k-ω model is the *Shear Stress Transport (SST) k-ω model*. This turbulence model allows to gradually switch from the standard k-ω model near a wall to the k-ε model at a certain distance from the wall, in the outer part of the boundary layer. How this transition is carried out is here briefly derived and discussed. As previously stated, the equation for ω, that is Equation (4.28), is formally the same as that for ε, that is Equation (4.21). However, the k-ε and the k-ω model are different form both a mathematical and a numerical point of view, and one way to prove it is to derive the equation for ω from the equation for ε. The demonstration of this statement is quite laborious, but it is useful to understand the main aspects of the SST k-ω model.
Consider Equation (4.21), expressed for simplicity in terms of substantial derivative

$$\frac{D\varepsilon}{Dt} = \nabla \cdot \left(\frac{\nu_T}{\sigma_\varepsilon} \nabla \varepsilon \right) + C_{\varepsilon 1} \frac{P\varepsilon}{k} - C_{\varepsilon 2} \frac{\varepsilon^2}{k} \tag{4.29}$$

Substitute $\omega = \varepsilon/k$

$$\frac{D(\omega k)}{Dt} = \nabla \cdot \left(\frac{\nu_T}{\sigma_\varepsilon} \nabla(\omega k) \right) + C_{\varepsilon 1} \frac{P\varepsilon}{k} - C_{\varepsilon 2} \frac{(\omega k)^2}{k} \tag{4.30}$$

Thus

$$k\frac{D\omega}{Dt} + \omega \frac{Dk}{Dt} = \nabla \cdot \left(\frac{\nu_T}{\sigma_\varepsilon} \nabla(\omega k) \right) + C_{\varepsilon 1} \frac{P\varepsilon}{k} - C_{\varepsilon 2} \frac{(\omega k)^2}{k} \tag{4.31}$$

Consider now Equation (4.20)

$$\frac{Dk}{Dt} = \nabla \cdot \left(\frac{\nu_T}{\sigma_k} \nabla k \right) + P - \varepsilon \tag{4.32}$$

Substituting the previous equation into Equation (4.31) and considering again $\omega = \varepsilon/k$, we obtain

$$k\frac{D\omega}{Dt} + \omega \left(\nabla \cdot \left(\frac{\nu_T}{\sigma_k} \nabla k \right) + P - \varepsilon \right) = \nabla \cdot \left(\frac{\nu_T}{\sigma_\varepsilon} \nabla(\omega k) \right) + C_{\varepsilon 1} \frac{P\varepsilon}{k} - C_{\varepsilon 2} \frac{(\omega k)^2}{k} \tag{4.33}$$

Dividing by k and rearranging, we have

$$\frac{D\omega}{Dt} = -\frac{\omega}{k} \nabla \cdot \left(\frac{\nu_T}{\sigma_k} \nabla k \right) + \frac{1}{k} \nabla \cdot \left(\frac{\nu_T}{\sigma_\varepsilon} \nabla(\omega k) \right) + (C_{\varepsilon 1} - 1) \frac{P\varepsilon}{k} - (C_{\varepsilon 2} - 1)\omega^2 \tag{4.34}$$

Consider the first term on the right-hand side of Equation (4.34) and substitute Equation (4.19); thus, we have

$$-\frac{\omega}{k} \nabla \cdot \left(\frac{\nu_T}{\sigma_k} \nabla k \right) = -\frac{C_\mu}{\sigma_k} \left(\frac{\nabla k \nabla k}{\omega} + \nabla^2 k - \frac{\nabla k \nabla \omega}{\omega} \right) \tag{4.35}$$

Similarly, for the second term on the right-hand side of Equation (4.34) we have

$$\frac{1}{k} \nabla \cdot \left(\frac{\nu_T}{\sigma_k} \nabla(\omega k) \right) = \frac{C_\mu}{\sigma_\varepsilon} \frac{\nabla k \nabla \omega}{\omega} + \frac{1}{\sigma_\varepsilon} \nabla \left(\frac{C_\mu k^2}{\varepsilon} \nabla \omega \right) + \frac{C_\mu}{\sigma_\varepsilon} \nabla^2 k + \frac{C_\mu}{\sigma_\varepsilon} \frac{\nabla k \cdot \nabla k}{k} \tag{4.36}$$

By substituting Equation (4.35) and Equation (4.36) into Equation (4.34) and rearranging, we obtain

$$\begin{aligned} \frac{D\omega}{Dt} = \nabla \cdot \left(\frac{\nu_T}{\sigma_\varepsilon} \nabla \omega \right) + (C_{\varepsilon 1} - 1) \frac{P\omega}{k} - (C_{\varepsilon 2} - 1)\omega^2 + \\ C_\mu \left(\frac{1}{\sigma_\varepsilon} + \frac{1}{\sigma_k} \right) \frac{1}{\omega} \nabla \omega \cdot \nabla k + C_\mu \left(\frac{1}{\sigma_\varepsilon} - \frac{1}{\sigma_k} \right) \left(\nabla^2 k + \frac{1}{k} \nabla k \cdot \nabla k \right) \end{aligned} \tag{4.37}$$

If we take

$$C_{\omega 1} = C_{\varepsilon_1} - 1 \qquad C_{\omega 2} = C_{\varepsilon_2} - 1 \qquad \sigma_k = \sigma_\varepsilon = \sigma_\omega \tag{4.38}$$

and substitute into Equation (4.37), we obtain

$$\frac{D\omega}{Dt} = \nabla \cdot \left(\frac{\nu_T}{\sigma_\omega} \nabla \omega \right) + C_{\omega 1} \frac{P\omega}{k} - C_{\omega 2} \omega^2 + \frac{2\nu_T}{\sigma_\omega k} \nabla \omega \cdot \nabla k \tag{4.39}$$

By comparing Equation (4.39) and Equation (4.28), we can see the presence of an additional term

$$\frac{2\nu_T}{\sigma_\omega k} \nabla \omega \cdot \nabla k \tag{4.40}$$

called *blending function*. Close to the wall, the blending function is zero and Equation (4.39) corresponds to the standard ω equation. On the other hand, far enough from the wall, the blending function is unity and Equation (4.39) corresponds to the standard ε equation. Hence, this function allows a gradual transition from the standard k-ω model near the wall to the k-ε model at a certain distance in the outer portion of the boundary layer, taking advantage of the best properties of the two models. For further details about the main characteristics of the SST k-ω model implemented in ANSYS® Fluent, refer to the ANSYS® Fluent Theory Guide [7].
The SST k-ω model is one of the most widely used turbulence models for aerodynamic problems. The SST k-ω model provides results similar to the standard k-ω model in solving the flow field in the region near a wall, that is in solving the boundary layer. Compared to other turbulence models, the SST k-ω model gives good results for flows subjected to mild adverse pressure gradients with boundary layer separation. However, in regions with strong shock-boundary layer interaction, the SST k-ω model could excessively overestimate separation. Despite this, the SST k-ω model is one of the most common turbulence model used for aerodynamic problems and turbomachinery performance analysis dealing with single airfoil or cascade under adverse pressure gradients.

4.5 Dimensionless wall distance y^+

An important parameter in CFD simulations is the so-called *dimensionless wall distance* y^+. It is defined as a non-dimensional distance from a wall and it is used to evaluate if a mesh is properly sized, that is how coarse or fine a mesh is, in order to ensure accurate simulation of the flowfield and in particular of the boundary-layer. Therefore, it is necessary to specify a suitable size for the first grid layer to have an $y^+ \simeq 1$, in order to accurately solve the boundary layer without using wall functions. Without going into too

much details, the procedure employed later for estimating the distance of the first layer of the grid from the wall derives from the boundary-layer theory for a flat-plate reported in [32] and is briefly described below.
Consider the fluid properties, that is density ρ, viscosity μ, and freestream velocity U_∞, known from the inlet boundary conditions. So, the Reynolds number can be calculated applying the definition

$$Re_L = \frac{\rho U_\infty L}{\mu} \tag{4.41}$$

where L is a reference length, in this case the chord of the blade section. The skin friction on the plate can be estimated as follows

$$C_f = 0.026 Re_L^{-1/7} \tag{4.42}$$

The wall shear stress can be found once the skin friction coefficient has been calculated

$$\tau_w = \frac{1}{2} C_f \rho U_\infty^2 \tag{4.43}$$

Hence

$$U_\tau = \sqrt{\frac{\tau_w}{\rho}} \tag{4.44}$$

Since the value of y^+ is imposed to be equal to 1, considering the definiton of y^+

$$y^+ = \frac{\rho U_\tau \Delta s}{\mu} \tag{4.45}$$

and rearranging, the first cell height Δs should be approximately

$$\Delta s = \frac{y^+ \mu}{U_\tau \rho} \tag{4.46}$$

For the complete and exhaustive theory of the boundary-layer, which is beyond the scope of this work to elaborate, refer to [23].

Chapter 5

Simulation of Flow Through ARL-SL19 Supersonic Cascade

In this chapter, the numerical simulation of the flow through a supersonic compressor cascade, referred as *ARL-SL19*, for different operating conditions is widely described. The grid sensitivity analysis and the validation study carried out with three different grid sizes and several turbulence models are illustrated. The CFD results, in terms of cascade performance and shock-wave pattern, are compared with the experimental results obtained in a supersonic wind tunnel facility.

5.1 ARL-SL19 cascade model

The *ARL-SL19* supersonic compressor cascade derives from a rotor near-tip section of a transonic axial compressor, described in [30] and [31]. The airfoil employed in the ARL-SL19 supersonic cascade is a precompression (S-shape) profile, which belongs to the so-called *ARL* supersonic profile category. The cascade is the two-dimensional aerodynamic equivalent of the compressor rotor blade section, from which it differs by the camber angle and the stream-tube area contraction at design. The cascade is the result of a design, fabrication, and testing process conducted at the Detroit Diesel Allison (DDA) Division of the General Motors Corp. In the 70's, it worked under the sponsorship of the Fluid Mechanics Research Laboratory of the Aerospace Research Laboratories (ARL) in Ohio, as reported in [6]. This cascade has aroused an ever-growing interest because of the excellent performance data obtained from the tests at DDA. The ARL-SL19 supersonic compressor cascade was also largely used for the experimental investigation of cascade performance and flow behaviour at various operating conditions, in particular for the analysis of the strong shock wave-boundary layer interaction on the blade suction

side. For that purpose, the cascade was also tested in other two supersonic cascade wind tunnel facilities, at the DFVLR in Cologne, as reported in [28], and at the ONERA, as reported in [9], with substantial differences in the examined operating conditions and in the testing arrangement, such as the number of blades, the blade chord, the cascade pitch, and the blade aspect ratio. Detailed experimental results are presented in other papers. For example, a comparison of the cascade results obtained at DFVLR, at DDA and at ONERA can be found in [25]. All these papers provide a thorough description of the cascade performance and the shock wave pattern for different operating conditions and analyze the influence of the main flow and geometric parameters on the overall cascade performance. For that reason, the ARL-SL19 supersonic compressor cascade has been considered suitable for the scope of this work.

5.1.1 Airfoil geometry

The shape of the airfoil employed in the ARL-SL19 cascade is given by points in [28] and reported in Table 5.1. The DFVLR cascade blade section coordinates were scaled from the original DDA values. As stated before, the airfoil of the ARL-SL19 supersonic compressor cascade is a *S-shape* airfoil, which is typical of supersonic axial compressors. A drawing of the cascade airfoil is sketched in Figure 5.1.

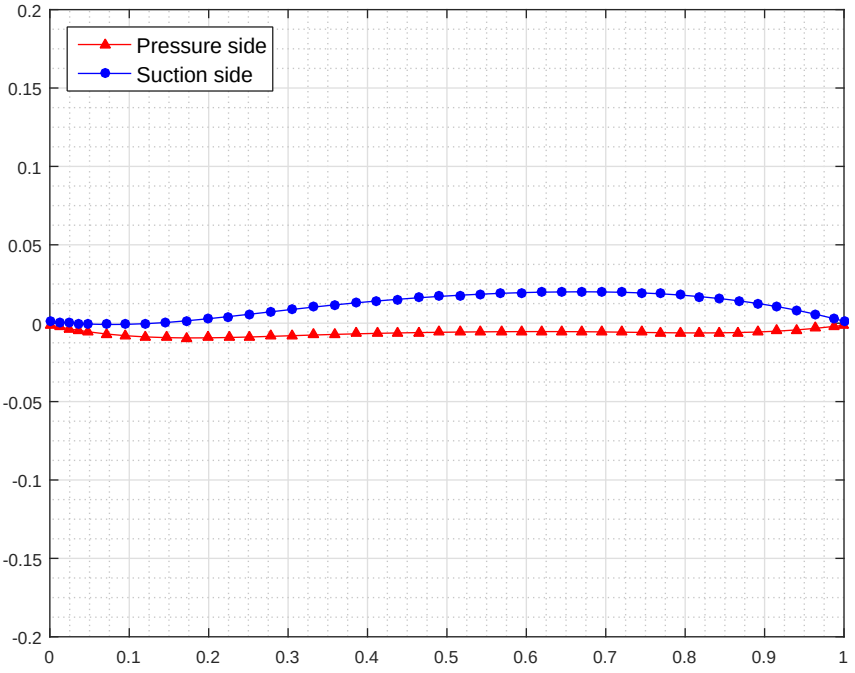

Figure 5.1: Airfoil geometry of ARL-SL19 supersonic cascade

Table 5.1: Coordinates of ARL-SL19 supersonic cascade airfoil

Suction side		**Pressure side**	
x/c	**y/c**	**x/c**	**y/c**
0.001389	0.001279	0.001170	-0.001274
0.012656	0.000661	0.012425	-0.002454
0.024082	0.000153	0.023844	-0.003535
0.035660	-0.000250	0.035422	-0.004518
0.047387	-0.000549	0.047164	-0.005402
0.071285	-0.000838	0.071114	-0.006885
0.095750	-0.000745	0.095658	-0.007995
0.120746	-0.000293	0.120748	-0.008761
0.146218	0.000481	0.146333	-0.009213
0.172107	0.001527	0.172342	-0.009395
0.198339	0.002790	0.198684	-0.009346
0.224836	0.004206	0.225272	-0.009132
0.251495	0.005714	0.252015	-0.008796
0.278244	0.007255	0.278317	-0.008390
0.305014	0.008783	0.305619	-0.007964
0.331755	0.010256	0.332374	-0.007536
0.358421	0.011662	0.359032	-0.007139
0.384988	0.012960	0.385573	-0.006784
0.411438	0.014149	0.411990	-0.006478
0.437768	0.015228	0.438286	-0.006219
0.463991	0.016203	0.464468	-0.005994
0.490107	0.017071	0.490544	-0.005806
0.516126	0.017836	0.516510	-0.005650
0.542037	0.018498	0.542370	-0.005524
0.567845	0.019048	0.568116	-0.005432
0.593545	0.019481	0.593746	-0.005371
0.619125	0.019797	0.619252	-0.005352
0.644583	0.019931	0.644619	-0.005370
0.669897	0.020033	0.669842	-0.005437
0.695076	0.019944	0.694920	-0.005552
0.720106	0.019713	0.719858	-0.005713
0.744997	0.019313	0.744659	-0.005884
0.769747	0.018729	0.769331	-0.006049
0.794367	0.017943	0.793885	-0.006171
0.818368	0.016949	0.818345	-0.006219
0.843268	0.015727	0.842723	-0.006164
0.867576	0.014268	0.867028	-0.005972
0.891806	0.012556	0.891284	-0.005617
0.915964	0.010575	0.915488	-0.005073
0.940058	0.008310	0.939661	-0.004310
0.964095	0.005741	0.963793	-0.003300
0.988073	0.002853	0.987909	-0.002021
1.000045	0.001283	0.999955	-0.001277

5.1.2 Cascade geometric parameters

The cascade geometric parameters adopted in this work are the ones adopted at the DFVLR and reported in [28]. The cascade geometric parameters are listed in Table 5.2.

Table 5.2: ARL-SL19 cascade geometric parameters

Cascade geometric parameters		
number of blades	n	5
chord	c	85 mm
pitch	s	55.58 mm
solidity	$\sigma = c/s$	1.5294
stagger angle	β_s	56.93°
leading edge radius/chord	r_{LE}/c	0.00128
maximum blade thickness/chord	t_{max}/c	0.0255
axial chord	c_{ax}	46.38 mm

The ARL-SL19 supersonic compressor cascade has a design inlet Mach number of 1.612, with a corresponding subsonic axial Mach number of about 0.90. The cascade design inlet Mach number M_1, static pressure ratio p_2/p_1, and axial velocity-density ratio (AVDR) are summarized in Table 5.3.

Table 5.3: ARL-SL19 design point parameters

Design point parameters		
Mach number	M_1	1.612
static pressure ratio	p_2/p_1	2.15
axial-velocity-density ratio	AVDR	1.00

5.2 Flow solver and computational domain

In this section, the grid generation procedure and the CFD solver setup are described. A powerful and user-friendly mesh generation software has been employed for creating the computational grids used in simulations. A widely used commercial CFD software, ANSYS® Fluent v16, has been employed for the numerical calculations.

5.2.1 Grid generation

The computational domain used for the simulations is shown in Figure 5.2. It consists of a periodic domain around a single blade airfoil with periodicity equal to the pitch spacing. The computational domain extends from $-1c_{ax} < x < 3.14c_{ax}$, where $x = 0$ corresponds to the leading edge of the airfoil. The dimensions of the domain in the mesh generator have been normalized by the chord and rescaled afterwards in the CFD solver.

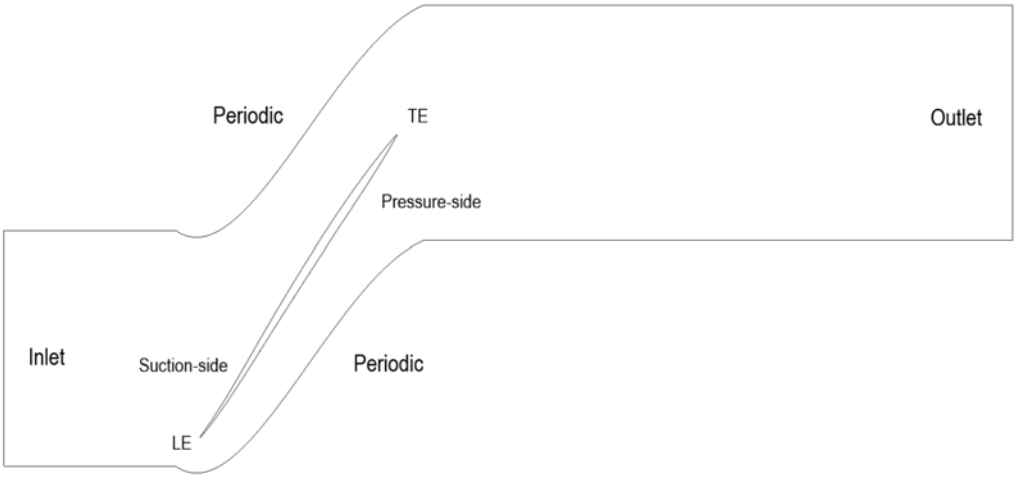

Figure 5.2: Computational domain

A multiblock structured grid with one O-grid around the airfoil was used, as shown in Figure 5.3. A multiblock structured grid is a mesh in which the domain is divided into different regions, called blocks, each of which is occupied by a structured grid, that is a mesh made of two-dimensional quadrilateral elements arranged in a uniform pattern. The O-grid around the airfoil was generated by using hyperbolic extrusion.

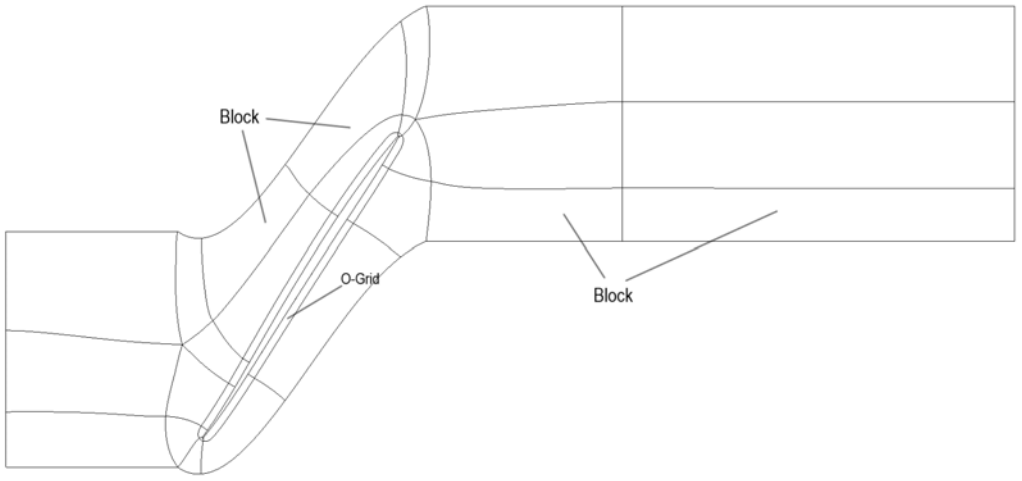

Figure 5.3: Computational grid topology

Generally speaking, for meshes which need accurate solutions of the boundary layer around airfoils or blades, a growth gate not exceeding 1.1 is recommended. A value of 0.0000016 m for the first cell height has been set. This value for the first grid layer has been computed using the flat-plate boundary layer theory described in Section 4.5. An example of the input set for the estimation of the dimensionless wall distance y^+ and the corresponding outcomes useful for the validation and the grid sensitivity analysis is summarized in Table 5.4. Input parameters have been choosen in order to respect the given Reynolds number, based on the operating conditions of the wind tunnel facility in which the experiments were carried out.

Table 5.4: Parameters for dimensionless wall distance estimation

Input			
freestream velocity	U_∞	448	$[m/s]$
freestream density	ρ_∞	0.43	$[kg/m^3]$
dynamic viscosity	μ	0.0000133	$[kg/ms]$
reference length	L	0.085	$[m]$
target dimensionless wall distance	y^+	1	
Output			
wall spacing	Δs	0.0000016	$[m]$
Reynolds number	Re	$\simeq 1.2 \cdot 10^6$	

Three grids with different nodes and elements numbers were investigated in order to find the suitable grid size providing the calculated data of better consistency with the experimental results, saving computational time at once. A *coarse mesh* of about 100k elements (Grid 1), a *medium mesh* of about 200k elements (Grid 2), and a *fine mesh* of about 500k elements (Grid 3) have been created. A comparison of the three different grid sizes is sketched in Figure 5.4, in which a close-up of the leading edge (on the left) and a close-up of the trailing edge (on the right) are shown. The grid size is increased from top to bottom.

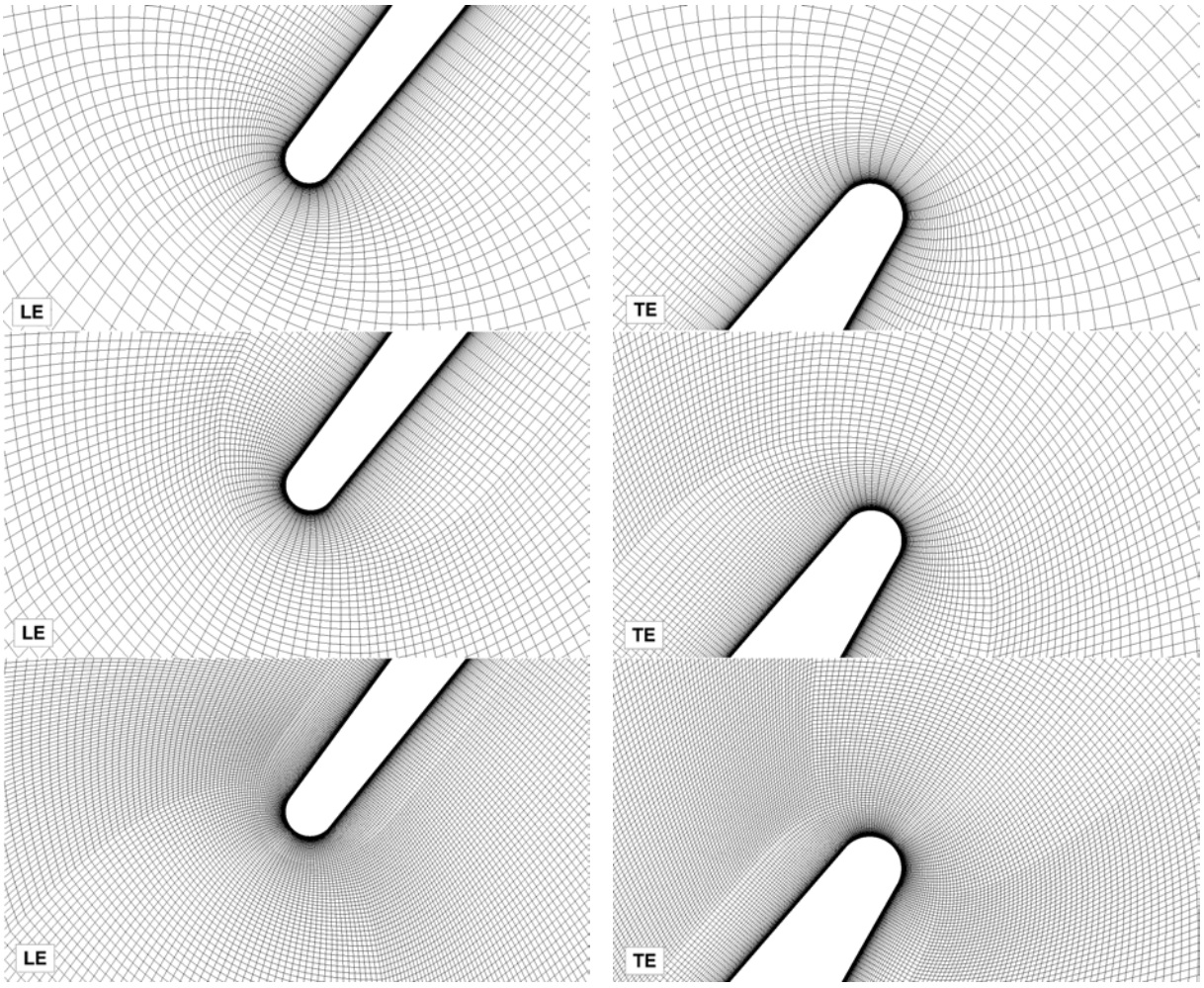

Figure 5.4: Comparison of the three grid sizes: a close-up of the leading-edge (on the left) and a close-up of the trailing-edge (on the right)

5.2.2 Grid quality check and improvement

Generally speaking, the quality of a mesh deeply affects the accuracy and the stability of a numerical simulation and this statement assumes an even higher importance for simulations of transonic flows. A good mesh can converge faster and can provide more accurate results. In contrast, a bad quality mesh usually provides inaccurate results, can converge slowly or not converge at all.

Most often, the main parameter used to check if a mesh is good enough or not is the *skewness angle*, or *equiangle skewness*. The skewness angle determines how close to equilateral a cell is. It is defined as the maximum ratio of the angles included in a cell to the angle of an equilateral element. The skewness varies between 0 (good quality) and 1 (bad quality). The skewness is computed as follows

$$max\left[\frac{(\theta_{max}-\theta_e)}{(180-\theta_e)}, \frac{(\theta_e-\theta_{min})}{\theta_e}\right] \tag{5.1}$$

where θ_{max} is the largest angle in the cell, θ_{min} is the smallest angle in the cell, and θ_e is the angle of an equilateral element, that is 90° for quadrilaterals (all angles are in degrees).

Another important parameter employed for grid quality checking is the *aspect ratio*. It is defined as the ratio of longest to the shortest length in the cell and ideally it should be equal to 1 to ensure best results. However, in structured quadrilateral grids, high aspect ratios are acceptable for the boundary layer cells.

In ANSYS® Fluent, the quality parameters are *Orthogonal Quality*, *Ortho Skew*, and *Maximum Aspect Ratio*. Orthogonal Quality ranges from 0 to 1, where values close to 0 correspond to low quality, and Ortho Skew ranges from 0 to 1, where values close to 1 correspond to low quality. The range of skewness and othogonal quality values with the related cell quality, provided by ANSYS® Fluent, are listed in the Tables on the next page. Table 5.7 summarizes the characteristics and the grid quality parameters of the three grids employed for the validation and the grid sensitivity analysis. According to the values of skewness and orthogonal quality listed below, the three mesh present very good quality characteristics.

Table 5.5: ANSYS® Fluent range of skewness values and related cell quality

Value of skewness	**Cell quality**
0	Equilateral
$> 0 - 0.25$	Excellent
$0.25 - 0.50$	Very good
$0.50 - 0.80$	Good
$0.80 - 0.94$	Acceptable
$0.95 - 0.97$	Bad
$0.98 - 1.00$	Unacceptable

Table 5.6: ANSYS® Fluent range of orthogonal quality and related cell quality

Value of orthogonal quality	**Cell quality**
$0 - 0.001$	Unacceptable
$0.001 - 0.14$	Bad
$0.15 - 0.20$	Acceptable
$0.20 - 0.69$	Good
$0.70 - 0.95$	Very good
$0.95 - 1.00$	Excellent

Table 5.7: Grid quality parameters

	Coarse	**Medium**	**Fine**
Total Elements	$100k$	$200k$	$500k$
Minimum Orthogonal Quality	0.79	0.78	0.77
Maximum Ortho Skew	0.21	0.22	0.23

5.2.3 Flow solver setup and boundary conditions

All simulations were carried out in ANSYS® Fluent v16. Two-dimensional steady state simulations were performed in double precision. Table 5.8 summarizes the main setups and the boundary conditions adopted.

At the inlet, a *pressure-far-field* boundary condition was imposed, in order to specify the inlet Mach number and the inlet flow angle (M_1,β_1) for respecting the unique incidence condition.

At the outlet, a *pressure outlet* boundary condition was imposed, specifying the outlet static pressure p_2 derived from a given static pressure ratio p_2/p_1.

To create the periodic boundary, the following command was typed into the Text User Interface (TUI):

/define/boundary-conditions/modify-zones/make-periodic

Blade walls, that is suction side, pressure side, leading-edge, and trailing-edge, were considered as no slip walls.

In order to obtain more accurate results and to ensure a better convergence, simulations have been carried out performing a few initial iterations with the first-order scheme and then turning on the second-order scheme. The calculation has then been continued until convergence.

In order to guarantee a more stable convergence, the Courant Number has been properly modified case-by-case to stabilize the convergence behaviour, even if a pressure-based simulation of a time-independent flow was carried out.

Convergence has been further accelerated by using the Full Multigrid initialization (FMG initialization). This type of initialization, compared to the Hybrid initialization, provides a better initial solution at a minimum computational cost. To customize and perform the FMG initialization, the following commands have to be typed into the TUI:

/solve/initialize/set-fmg-initialization

/solve/initialize/fmg-initialization

Convergence was established when all residuals went under $1e^{-06}$ and oscillations of some variables of interest (such as inlet and exit Mach number, inlet flow angle, and mass flow rate) were below a certain threshold or were stable around low values.

A journal file was developed in order to automatically set up the simulations in ANSYS® Fluent.

Table 5.8: CFD solver setup and boundary conditions

ANSYS®Fluent solver setup		
General		
Solver	Type	Pressure-based
	Time	Steady
	2D Space	Planar
Models		
Models	Energy	On
	Viscous	
Materials		
Materials	Air	
Properties	Density	Ideal Gas
	Cp (Specific Heat)	constant
	Thermal Conductivity	constant
	Viscosity	sutherland
	Molecular Weight	constant
Boundary Conditions		
Zone	inlet	pressure-far-field
	outlet	pressure-outlet
	upper/lower boundaries	periodic
	suction side	wall
	pressure side	wall
	leading edge	wall
	trailing edge	wall
Solution Methods		
Pressure-Velocity Coupling	Scheme	Coupled
Spatial Discretization	Gradient	Least Squares Cell Based

5.3 Grid sensitivity analysis and validation

In this section, the main outcomes of the grid sensitivity analysis and the validation study will be illustrated. The validation study is aimed at obtaining a reliable and accurate numerical model, saving computational time and verifying that the results remain essentially unchanged. Three grid sizes were employed for the validation study: a coarse grid of about 100k elements, a medium grid of about 200k elements, and a fine grid of about 500k elements. The turbulence models used for the simulations, ordered by complexity and increase in computational cost per iteration, were the Spalart-Allmaras model (S-A), the k-ε model in its three available formulations (STD k-ε, RNG k-ε and REALIZABLE k-ε), and the Shear-Stress Transport (SST) k-ω model.

5.3.1 Test cases

Three test cases, conducted in the supersonic cascade wind tunnel facility at the DFVLR and reported in [28], were selected for the validation of the numerical model and the grid sensitivity analysis. The test facility and instrumentation are widely described in [28]. A drawing of the wind tunnel test section in which the experiments were carried out is shown below, for illustrative purposes only. The picture is taken from [28].

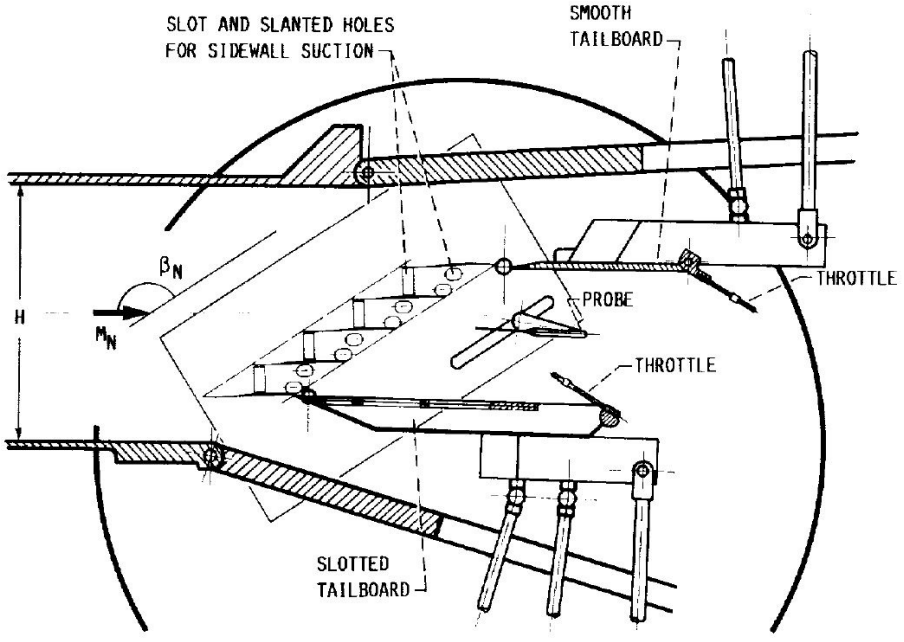

Figure 5.5: Sketch of the wind tunnel section

Inlet flow conditions and outlet flows data for each test case, such as the inlet Mach number M_1, the static pressure ratio p_2/p_1, the total-pressure loss coefficient ω, the exit flow angle β_2, and the exit Mach number M_2 are listed in Table 5.9. The inlet Mach number is equal to 1.58 and 1.59, while the static pressure ratio is 2.16, 2.12, and 2.21, respectively. The AVDR is almost unity (AVDR= 1.00) in each of the three test cases.

Table 5.9: Test cases data used for the validation

Parameter		**Test case 1**	**Test case 2**	**Test case 3**
Input				
inlet Mach number	M_1	1.58	1.58	1.59
inlet flow angle	β_1	57.9°	57.9°	57.9°
static pressure ratio	p_2/p_1	2.16	2.12	2.21
axial velocity-density ratio	AVDR	1.00	0.99	1.02
Output				
exit Mach number	M_2	0.91	0.93	-
exit flow angle	β_2	60.8°	61.2°	60.2°
total-pressure loss coefficient	ω	0.143	0.144	0.150

It is important to underline that the choice to simulate a single two-dimensional blade airfoil in a periodic domain does not accurately reflect the experimental setup, because all the cascade tests were conducted with a three-dimensional geometry, a finite number of blades, that is 5, and with sidewall boundary layer suction to avoid adverse effects. However, the periodic condition allows to simulate the case of a real flow through a rotating axial turbomachine. Moreover, this conscious simplification allows to simulate a flow not dependent on the AVDR, because the axial velocity-density ratio is always unity for a two-dimensional simulation. Moreover, the presence of secondary flows and non-periodicity effects are avoided.

The experimental behaviour of the isentropic Mach number on the suction side and on the pressure side of the blade section for the three test cases is shown in Figure 5.6.

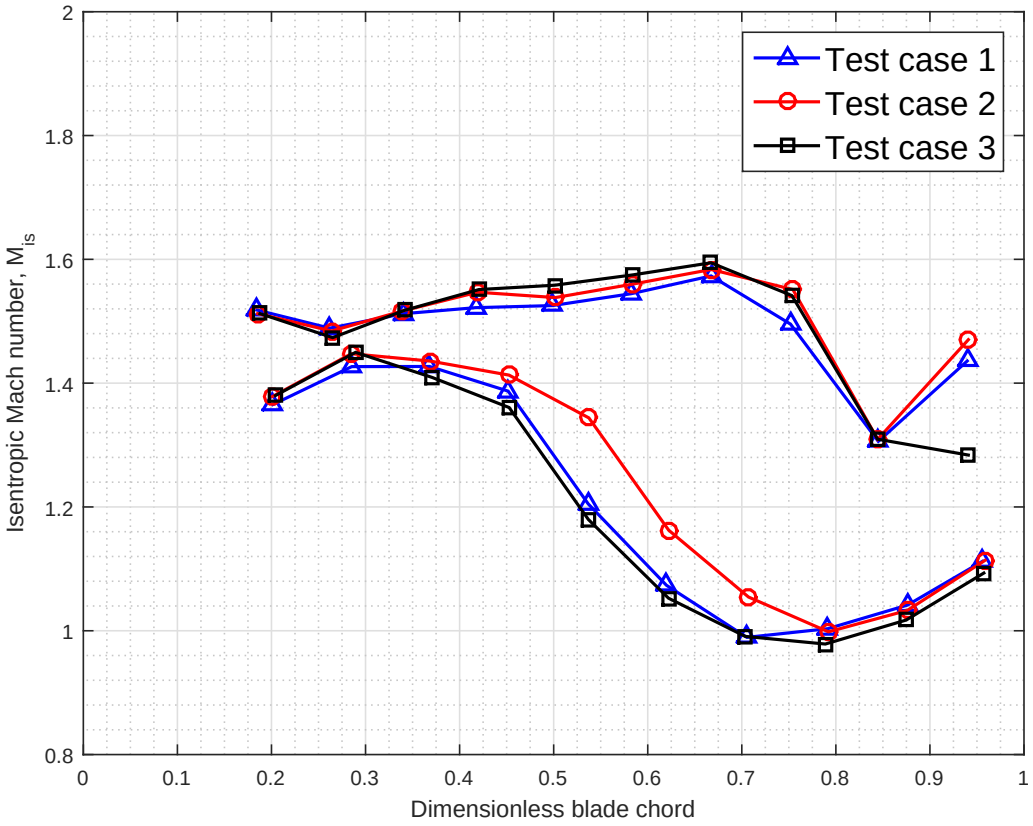

Figure 5.6: Experimental blade isentropic Mach number distribution for the three test cases

5.3.2 Specification of the unique incidence condition

As stated before, for supersonic inlet flows with axial subsonic component, in order to respect the inlet flow conditions imposed by the unique incidence, it is necessary to specify the Prandtl-Meyer relation, also referred as the supersonic Riemann invariant

$$\beta + \nu(M) = const \tag{5.2}$$

that is the relation between the inlet Mach number and the inlet flow angle. The pressure-far-field adopted as inlet boundary condition allowed to specify this relation, because it makes it possible to set the inlet Mach number and the inlet flow direction. However, the inlet flow angle depends on how the mesh grid is aligned with the flow and for that reason it is not equal to the experimental inlet flow angle. Thus, for a given Mach number, the inlet flow angle becomes an outcome of the simulation, that is a dependent variable, and must be determined. For that reason, in order to identify the correct flow condition (M_1,β_1) that satisfies the unique incidence, for a specified inlet Mach number, the inlet flow angle was manually varied until the difference between the calculated inlet Mach number and the imposed inlet Mach number was below a certain threshold.

5.3.3 Inlet flow conditions

For the wide range of cascade tests described in [28], the wind tunnel operating conditions were set to an upstream total pressure in the range 100 and 130 kPa and a total temperature between 300 and 312 K. The chord Reynolds numbers were in the range $1.1 \cdot 10^6$ to $1.4 \cdot 10^6$, for cascade inlet Mach numbers between 1.30 and 1.71.

For the purpose of this work, having no information about the exact cascade operating conditions for the test cases selected as benchmark data for the validation, a total pressure of 101325 Pa, a total temperature of 300 K, and a Reynolds number of about $1.2 \cdot 10^6$ were set as operating conditions, referring to the experimental range reported in [28] and listed above. The turbulence intensity for the test cases at DFVLR reported in [28] was measured to be less than 1, as reported in [25]. Thus, having no further information about the turbulence levels in the wind tunnel in which the experiments were carried out, a value of 1% for the turbulence intensity and a value of 1 for the turbulent viscosity were used, even if the preset default values for turbulent intensity and turbulent viscosity ratio (5% and 10, respectively) are reasonable for cases in which no information about turbulence at inlet is available. However, the adopted specification of turbulent intensity and turbulent viscosity ratio is more reasonable for a freestream in a wind tunnel.

5.3.4 Calculation of the variables of interest

Downstream calculations of static pressure, total-pressure, exit Mach number, and mean exit flow angle were obtained with a *mass-weighted average* surface integral at an axial distance of 26 mm ($\xi/c_{ax} = 0.56$) downstream of the cascade exit plane, exactly where the probe was located during the experiments in the supersonic wind tunnel, as reported in [28]. The location of the measurement plane is sketched in the Figure below, adapted from [28]. Inlet Mach number, inlet flow angle, inlet static pressure, and inlet total pressure were calculated using a *mass-weighted average* surface integral at the domain inlet. The total-pressure loss coefficient was also calculated and compared with the corresponding experimental coefficient. The estimated uncertainties reported in [28] for the key dependent variables, that is the inlet flow angle β_1, the mean exit flow angle β_2, and the total-pressure loss coefficient ω are listed below. These relatively large uncertainties are due to non-periodicity effects and secondary flows, as stated in [28]. In the reference article, all the average variables have been calculated by using the "*mixed-out*" type of integration.

Table 5.10: Estimated uncertainties for the main quantities

Quantity		Uncertainty
Inlet flow angle	β_1	$\pm 0.5°$
Exit flow angle	β_2	$\pm 1.5°$
Loss coefficient	ω	± 0.010

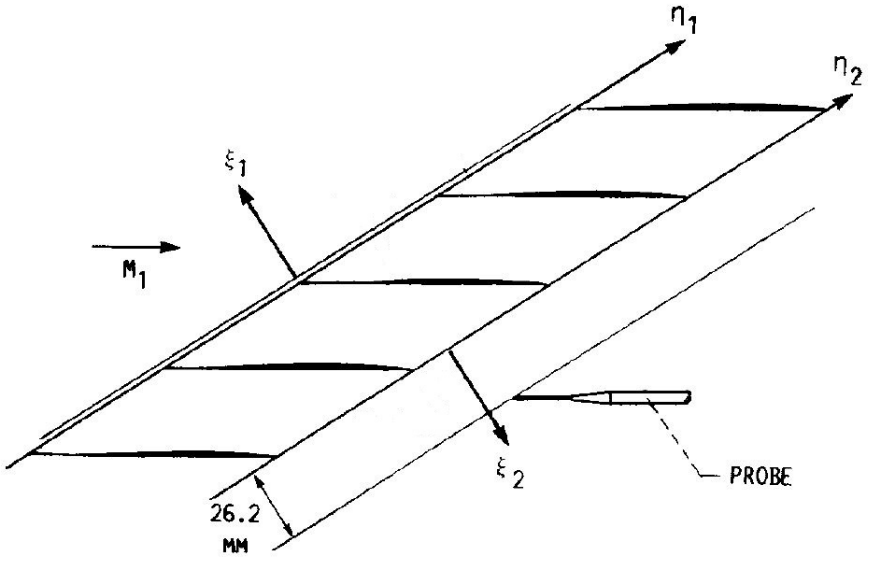

Figure 5.7: Measurement plane location downstream of the cascade

5.3.5 Results and discussion

The CFD results for each test case are listed in the Tables in the following pages, in comparison with the experimental results. For brevity, only the outcomes obtained with the S-A model and the STD k-ε model are reported, because the simulations carried out with these two turbulence models gave more accurate results. The calculated isentropic Mach number distributions for the S-A model and the STD k-ε are plotted in comparison with the experimental trends, along with the contours of the Mach number through the cascade for the finest grid.

The CFD results obtained with the S-A model and the STD k-ε are in substantial agreement with the corresponding experimental results. The variations of cascade performance and exit flow variables as a function of grid size are quite subtle. Moreover, the isentropic Mach number distribution is not affected at all by the grid size.

As regards the inlet flow angle, the difference between the calculated inlet flow angle and the experimental inlet flow angle, whose prediction seems to be overestimated regardless grid size, is due to the turbulence model employed, which can be more or less dependent on the inlet turbulence entity specified, and to the mesh quality, as previously specified. As a consequence, the inlet angle and also the exit angle are shifted to higher values than the experimental ones. The reported experimental inlet flow angle was 57.9°, against a inlet flow angle of 58.4° and 58.6° calculated with the S-A model and the STD k-ε respectively in the first test case and in the second test case. The inlet flow angle calculated using the S-A model and the STD k-ε for the third test case was 58.3° and 58.5° respectively. Based on the results, the STD k-ε seems to overestimate the inlet flow angle slightly more.

As regards the exit Mach number, it is quite well predicted regardless the turbulence model employed and the grid size in each of the two test cases for which the experimental results are available.

As regards the total-pressure loss coefficient, the S-A model and the STD k-ε seem to be in very good agreement with the experiments, even if the S-A model underestimates the total-pressure loss coefficient in the third test case, while the STD $k-\varepsilon$ seems to slighlty overestimate it in the first test case and in the second test case. The estimation of the total-pressure loss coefficient with the STD k-ε model seems to be in better agreement with the experiments, since the percentage error is never greater than 3%, against a percentage error of 5.6%, 4.9%, and 11.3% calculated with the S-A model in the three test cases respectively. The relative percentage error as a function of the grid size for the three test cases is reported in the Tables and in the Figures in the following pages.

Table 5.11: Calculated loss coefficients and relative percentage errors (Test case 1)

Exp. ω	**Grid size**	**S-A**	**err%**	**STD** k-ε	**err%**
0.143	100k	0.138	3.5	0.149	4.2
	200k	0.135	5.6	0.146	2.1
	500k	0.135	5.6	0.145	1.4

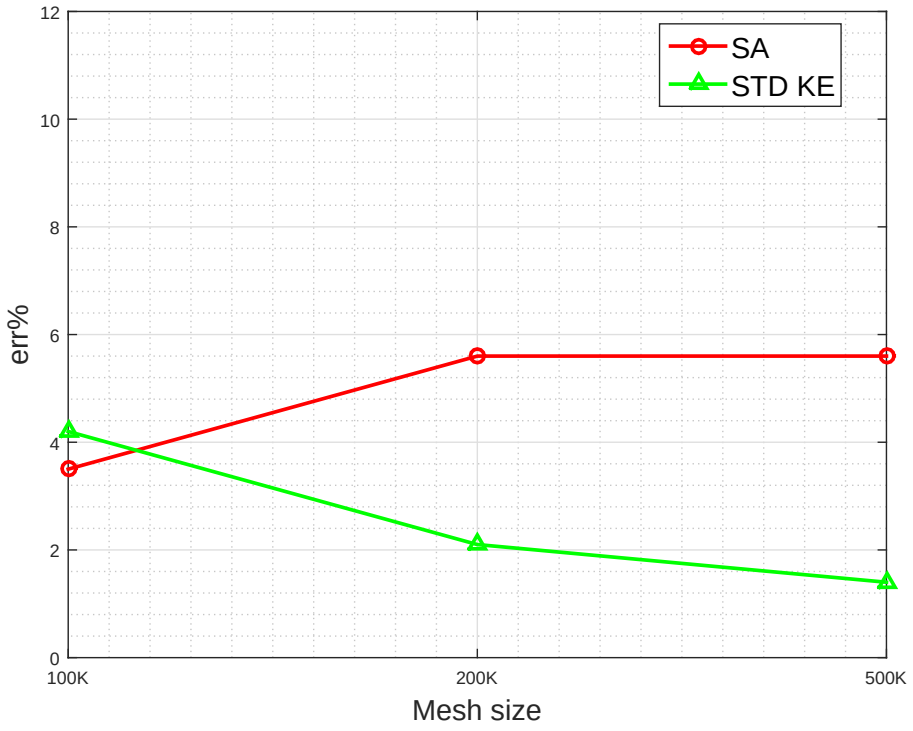

Figure 5.8: Relative percentage error for the total-pressure loss coefficient as a function of grid size (Test case 1)

Table 5.12: Calculated loss coefficients and relative percentage errors (Test case 2)

Exp. ω	**Grid size**	**S-A**	**err%**	**STD** k-ε	**err%**
0.144	100k	0.140	2.8	0.151	4.9
	200k	0.137	4.9	0.148	2.8
	500k	0.137	4.9	0.148	2.8

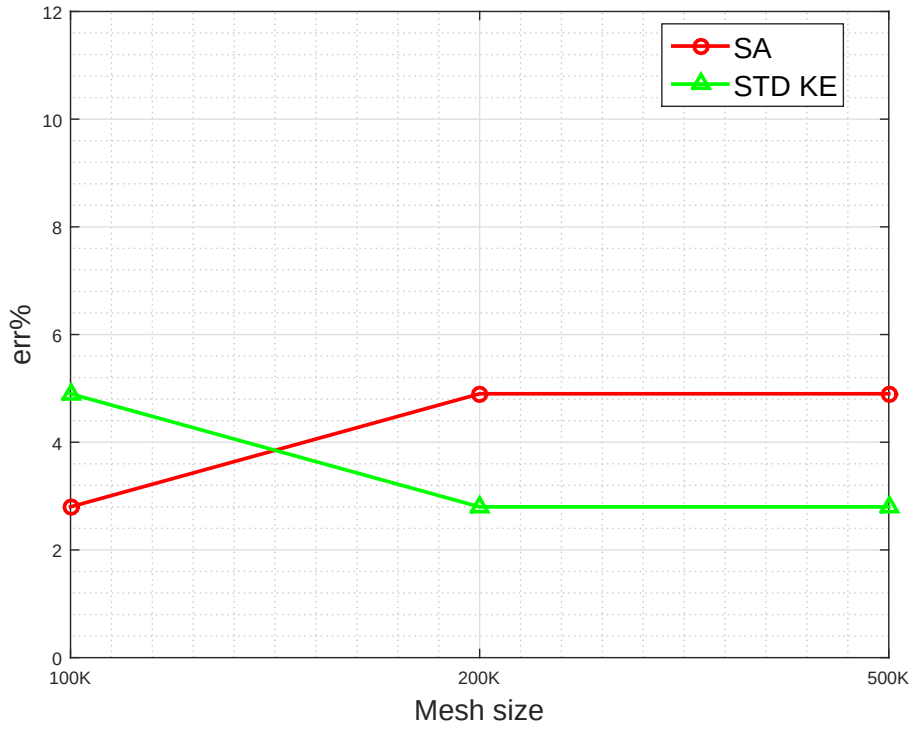

Figure 5.9: Relative percentage error for the total-pressure loss coefficient as a function of grid size (Test case 2)

Table 5.13: Calculated loss coefficients and relative percentage errors (Test case 3)

Exp. ω	**Grid size**	**S-A**	**err%**	**STD** k-ε	**err%**
0.150	100k	0.136	9.3	0.149	0.7
	200k	0.133	11.3	0.147	2.0
	500k	0.133	11.3	0.147	2.0

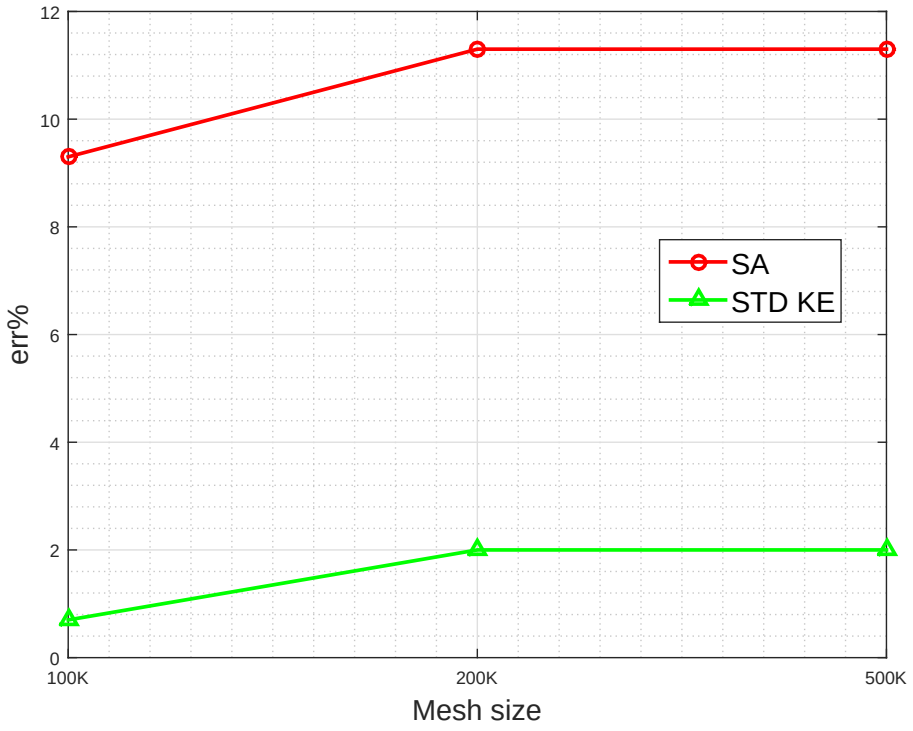

Figure 5.10: Relative percentage error for the total-pressure loss coefficient as a function of grid size (Test case 3)

The calculated isentropic Mach number distributions on the suction side and on the pressure side of the airfoil present substantial differences in comparison with the experimental profiles, especially around the peaks representing the location of the shock waves on the blade surfaces, as we can see in the Figures in the following pages. This significant diversity is due to three main reasons:

- the turbulence model employed for the simulations; in fact, the way in which the flow field and the wave pattern are solved depends on the turbulence model. Consequently, also the isentropic Mach number distribution on the suction side and on the pressure side of the airfoil depends on the turbulence model employed;
- the presence of three dimensional effects and disturbances during the experiments;
- the approach adopted for the validation and the grid sensitivity analysis; the input parameters of the simulations, such as the inlet Mach number, the inlet flow angle, and especially the static pressure ratio have been set in such a way that they showed the best agreement with the experimental quantities, and not in such a way that the isentropic Mach number distribution and the shockwave location were in the best agreement with the experimental distribution and layout, respectively. In fact, the numerical inlet boundary conditions, especially the static pressure ratio, should be slightly adjusted case-by-case with respect to the experimental values, in a way that the shock wave pattern and the isentropic Mach number distribution obtained from the simulations result in good agreement with the experiments. However, this adjustement could bring to a static pressure ratio significantly different from the imposed experimental one, because of the turbulence model used. This approach takes away every information on the effective static pressure ratio at which the cascade is operating, adapting the problem to the static pressure ratio "seen" by the turbulence model. This validation approach is widely used to validate codes or numerical solvers. Since the aim of the validation in this work is to identify the turbulence model which gives the results of better consistency with the experimental performance parameters for a given static pressure ratio and then evaluate the performance of the cascade for different operating conditions, this validation approach is not recommended for the purpose of this work.

Anyway, the S-A model seems to better reproduce the isentropic Mach number distribution on the pressure side and the suction side of the airfoil in all the analyzed test cases. In other words, the S-A model better reproduces the shock wave pattern inside the cascade passage.

The blade-to-blade wake losses for the second and the third test case, calculated with the S-A model and the STD k-ε, are sketched in Figure 5.23 and in Figure 5.24, respectively. The wake seems to be quite well captured by the S-A model. In fact, the local loss coefficient curves calculated with the S-A model are well aligned on the peak and on the left concavity, which represent viscous losses and shock losses respectively. The not complete consistency with the experimental results is probably due to mixing phenomena downstream of the cascade, which are unsteady and not predictable by a steady state simulation, and to the non-periodicity of the experimental cascade. In fact, it can be seen quite easily that the experimental blade-to-blade loss profile is not periodic, because of the finite number of blades in the testing arrangements. The results of the validation are also in quite good agreement with the ones obtained in [18] for the second test case and the third test case.

Overall, the CFD results seem to accurately predict the cascade performance, even considering the quite high experimental uncertainties. The validation study and the grid sensitivity analysis suggested that for the purpose of this work the medium grid could be adopted, because it represents the best compromise between accuracy and computational time. As regards the turbulence model, the validation study showed that the S-A model gave more precise results in simulating the flow in the blade passage and across the wake, even if it seems to slightly underestimate the total-pressure loss coefficient. Despite this, it has been choosen as the turbulence model for the subsequent simulations. Another important reason behind the choice of the S-A model will be described later.

The main considerations resulting from the validation study are summarized below:

- as regards the total-pressure loss coefficient, the S-A model has a tendency to underestimate it, while the STD k-ε seems to overestimate it;
- as regards the isentropic Mach number profile, the S-A model better predicts the distribution on the pressure side and on the suction side of the airfoil;
- as regards the downstream blade-to-blade total-pressure loss, the curves calculated with the S-A model are better aligned with the experimental ones;
- as regards the inlet flow angle, it is better determined by the S-A model;
- as regards the exit Mach number and the mean exit flow angle, there are no significant differences between the two turbulence models employed.

Although not reported here for brevity, it is worth to say a couple of words about the results obtained with the other turbulence models tested in the validation study. As regards the total-pressure loss coefficient, the mean exit flow angle and the exit Mach number, they seem to be quite well calculated by the REALIZABLE k-ε model and the RNG k-ε model. However, the isentropic Mach number distribution and the blade-to-blade losses measured downstream of the cascade were not as well predicted. The isentropic Mach number distribution on the suction side is not well captured by both the turbulence models, especially in the rearmost part near the trailing-edge, as well as the blade-to-blade total-pressure loss coefficient, which results deeply underestimated. The SST k-ω model gave a poor resolution of the isentropic Mach number distribution on the suction side of the blade in the first test case and seems to widely underestimates the total-pressure loss coefficient in the second test case and in the third test case, showing an excessive boundary layer separation on the blade suction side, which affects the calculation of the isentropic Mach number distribution and the total-pressure loss coefficient.

Table 5.14: Cascade parameters calculated with Grid 1 (Test case 1)

Mesh coarse 100k			
$M_1 = 1.58$		$p_2/p_1 = 2.16$	
Parameter	**Exp.**	**S-A**	**STD** k-ε
β_1	57.9	58.4	58.6
M_2	0.91	0.91	0.90
β_2	60.8	61.1	60.9
ω	0.143	0.138	0.149

Table 5.15: Cascade parameters calculated with Grid 2 (Test case 1)

Mesh medium 200k			
$M_1 = 1.58$		$p_2/p_1 = 2.16$	
Parameter	**Exp.**	**S-A**	**STD** k-ε
β_1	57.9	58.4	58.6
M_2	0.91	0.91	0.90
β_2	60.8	61.1	60.8
ω	0.143	0.135	0.146

Table 5.16: Cascade parameters calculated with Grid 3 (Test case 1)

Mesh fine 500k			
$M_1 = 1.58$		$p_2/p_1 = 2.16$	
Parameter	**Exp.**	**S-A**	**STD** k-ε
β_1	57.9	58.4	58.6
M_2	0.91	0.91	0.90
β_2	60.8	61.1	60.8
ω	0.143	0.135	0.145

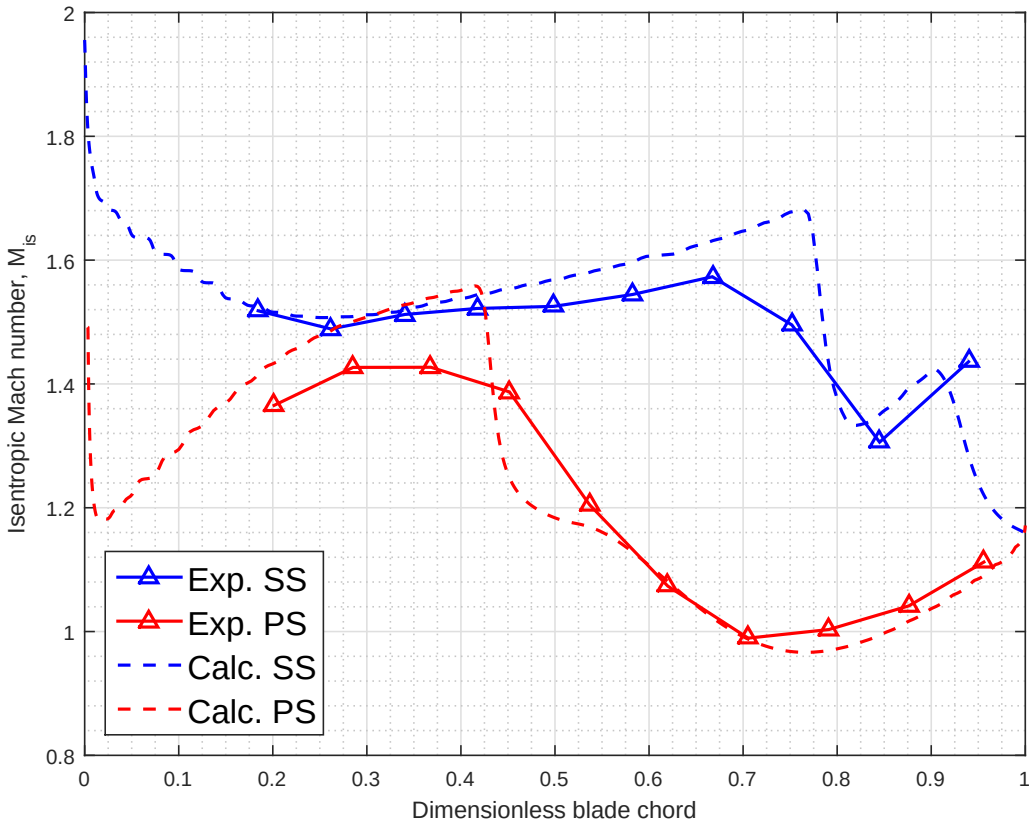

Figure 5.11: Distribution of isentropic Mach number using S-A model (Test case 1)

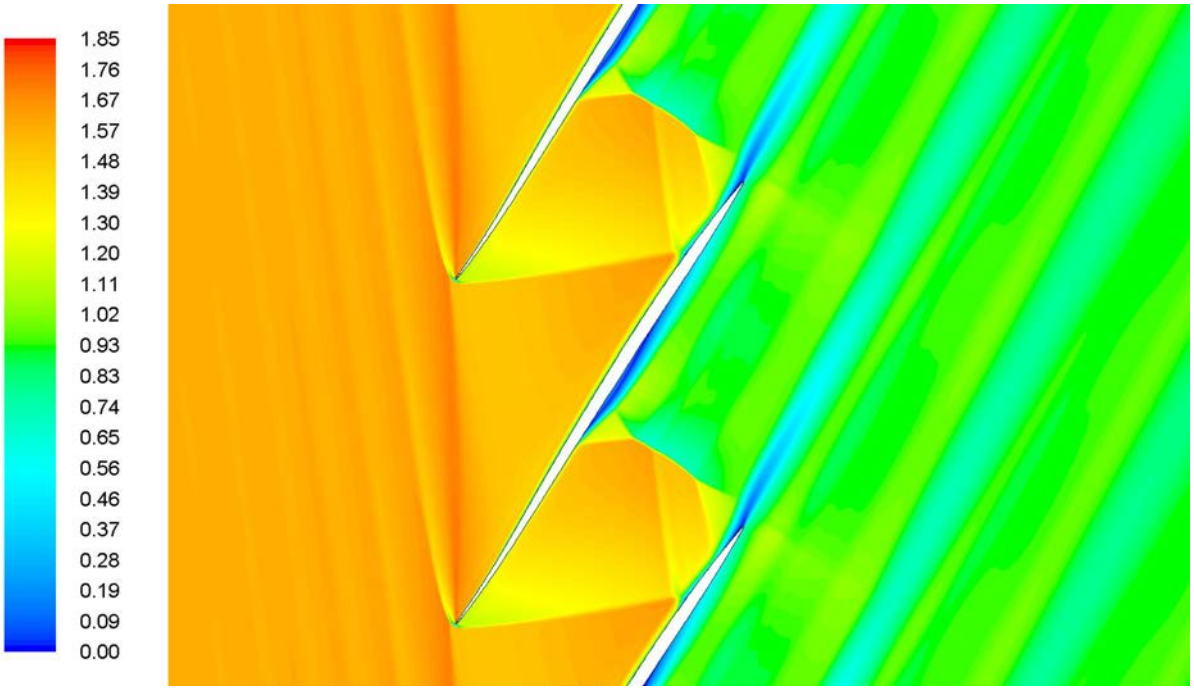

Figure 5.12: Mach number contours using S-A model (Test case 1)

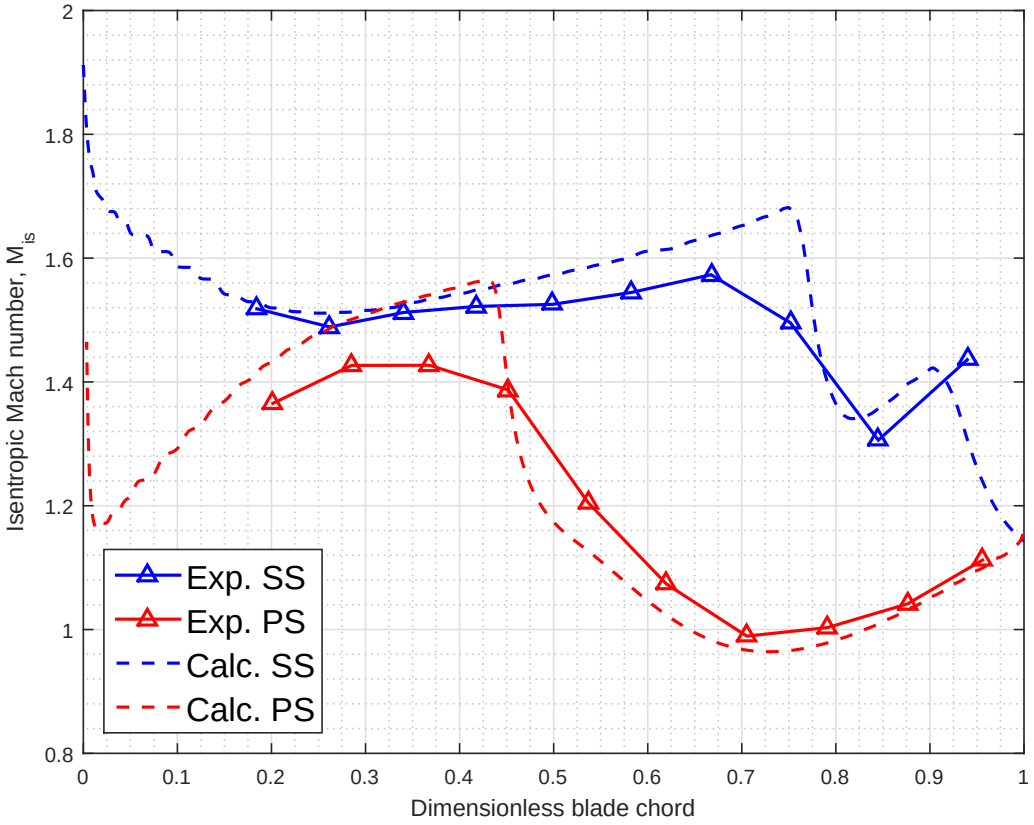

Figure 5.13: Distribution of isentropic Mach number using STD k-ε model (Test case 1)

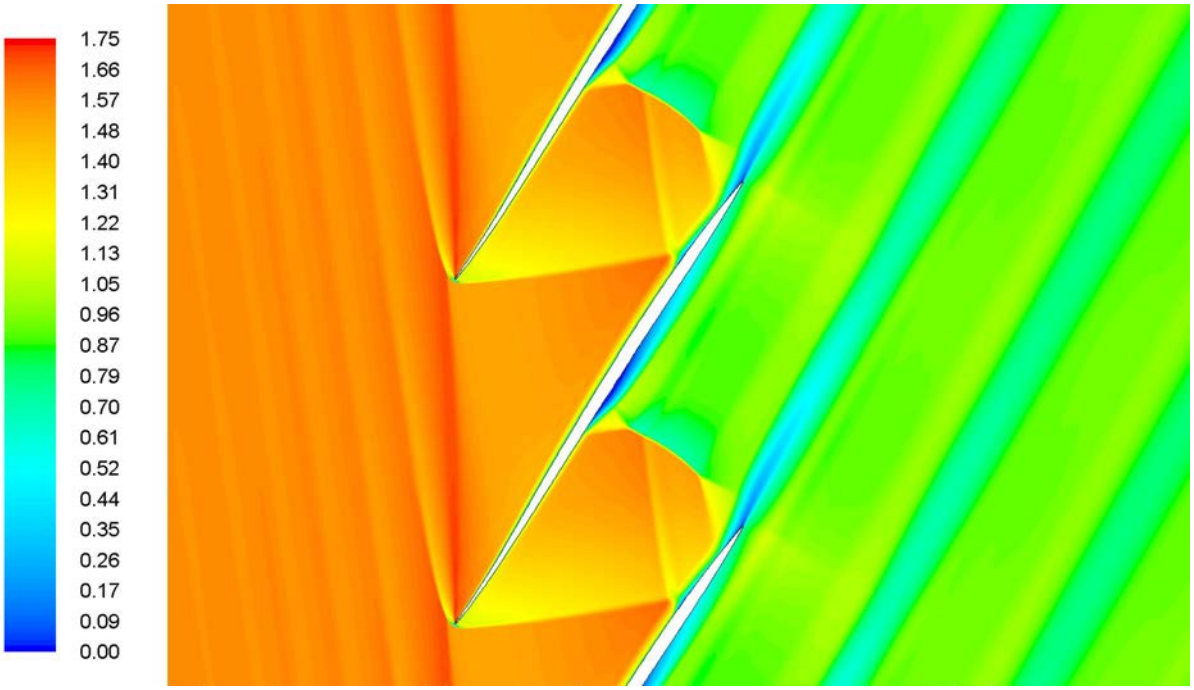

Figure 5.14: Mach number contours using STD k-ε model (Test case 1)

Table 5.17: Cascade parameters calculated with Grid 1 (Test case 2)

Mesh coarse 100k			
$M_1 = 1.58$		$p_2/p_1 = 2.12$	
Parameter	**Exp.**	**S-A**	**STD** k-ε
β_1	57.9	58.4	58.6
M_2	0.93	0.92	0.91
β_2	61.2	61.2	60.9
ω	0.144	0.140	0.151

Table 5.18: Cascade parameters calculated with Grid 2 (Test case 2)

Mesh medium 200k			
$M_1 = 1.58$		$p_2/p_1 = 2.12$	
Parameter	**Exp.**	**S-A**	**STD** k-ε
β_1	57.9	58.4	58.6
M_2	0.93	0.92	0.91
β_2	61.2	61.2	60.9
ω	0.144	0.137	0.148

Table 5.19: Cascade parameters calculated with Grid 3 (Test case 2)

Mesh fine 500k			
$M_1 = 1.58$		$p_2/p_1 = 2.12$	
Parameter	**Exp.**	**S-A**	**STD** k-ε
β_1	57.9	58.4	58.6
M_2	0.93	0.92	0.91
β_2	61.2	61.2	60.9
ω	0.144	0.137	0.148

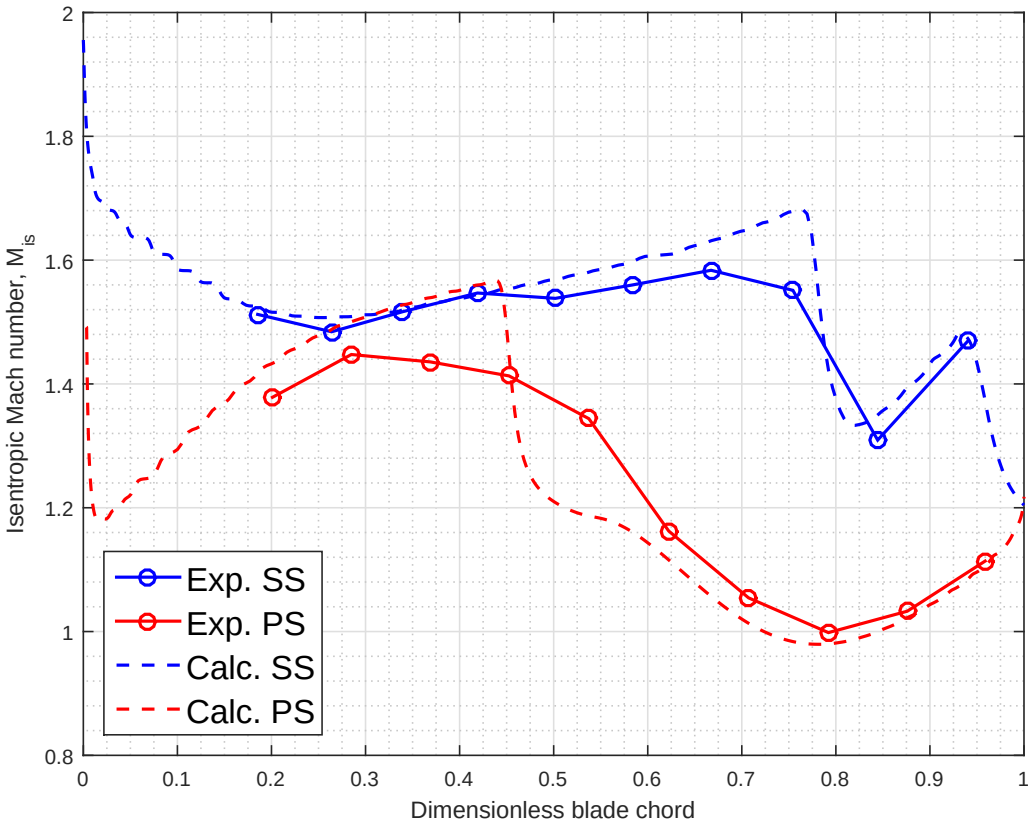

Figure 5.15: Distribution of isentropic Mach number using S-A model (Test case 2)

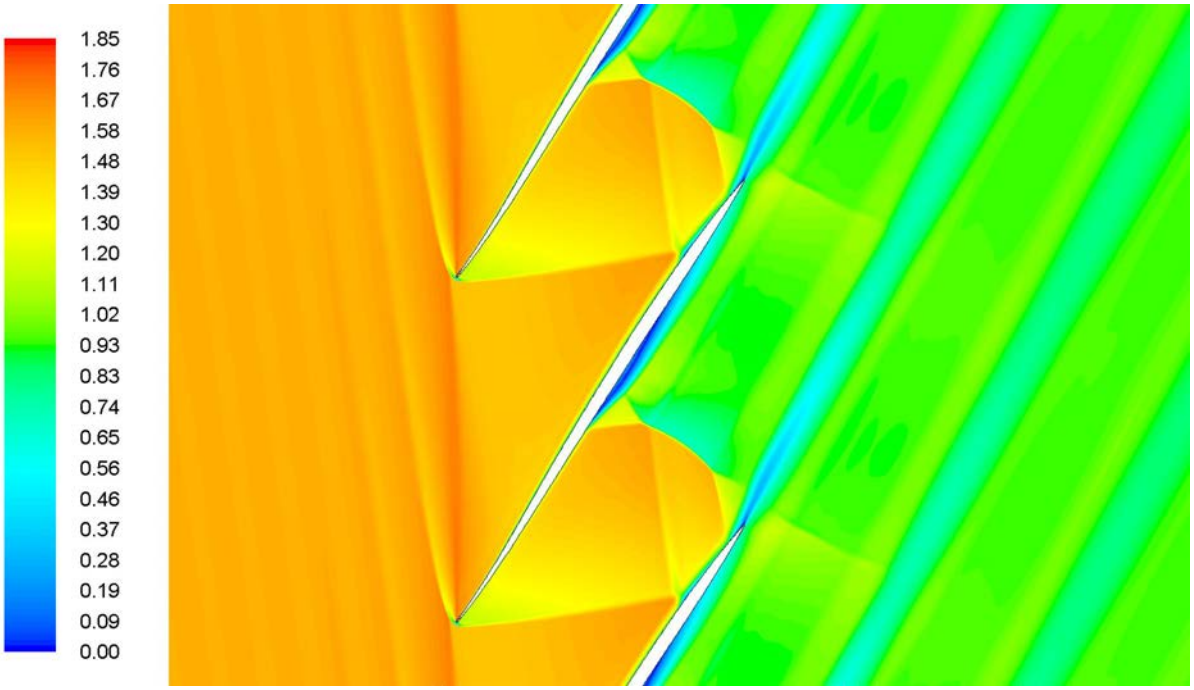

Figure 5.16: Mach number contours using S-A model (Test case 2)

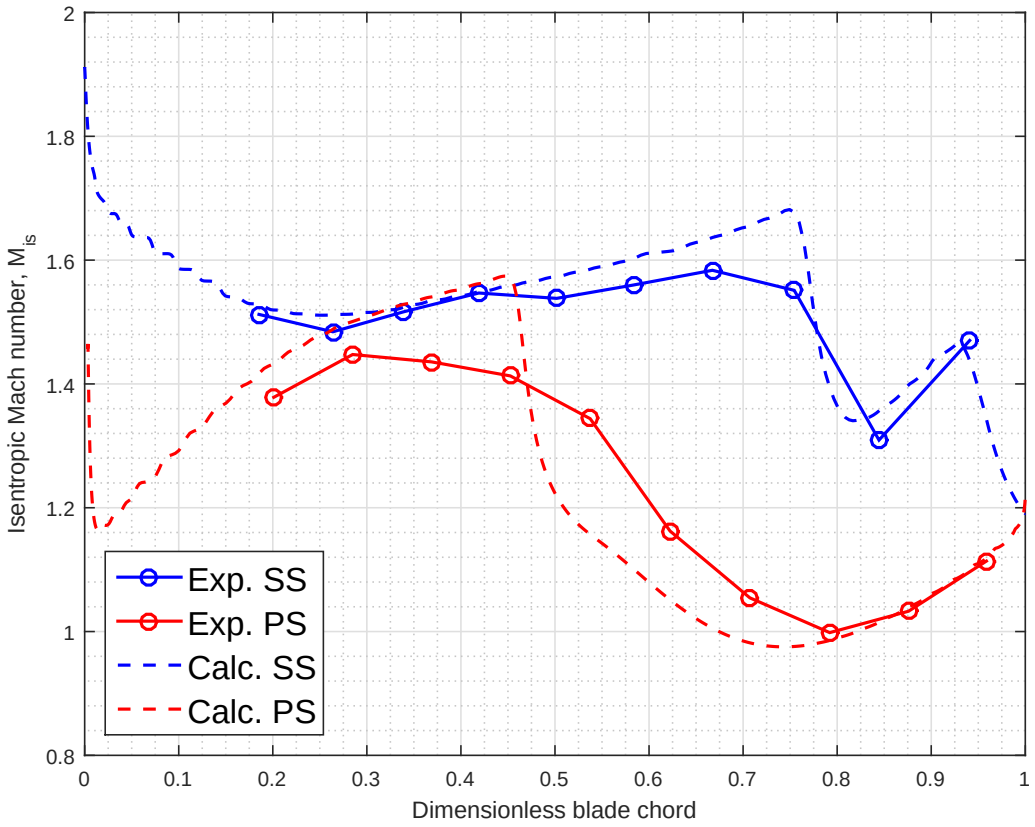

Figure 5.17: Distribution of isentropic Mach number using STD k-ε model (Test case 2)

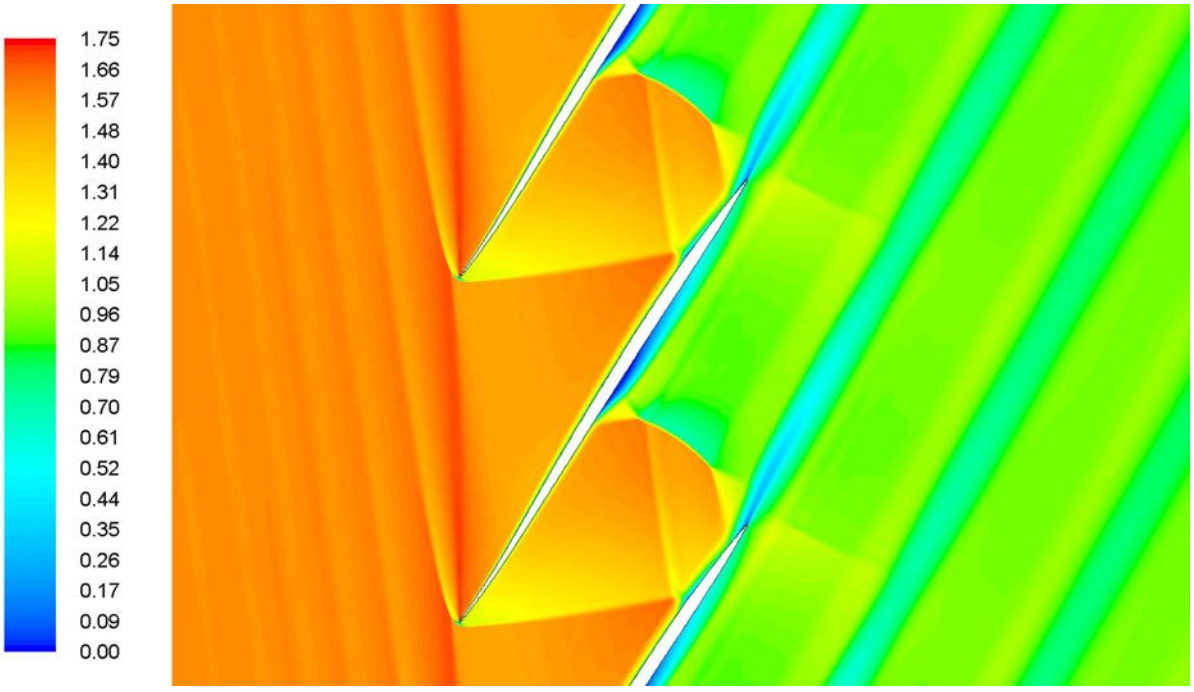

Figure 5.18: Mach number contours using STD k-ε model (Test case 2)

Table 5.20: Cascade parameters calculated with Grid 1 (Test case 3)

Mesh coarse 100k			
$M_1 = 1.59$		$p_2/p_1 = 2.21$	
Parameter	**Exp.**	**S-A**	**STD** k-ε
β_1	57.9	58.3	58.5
β_2	60.2	61.2	60.9
ω	0.150	0.136	0.149

Table 5.21: Cascade parameters calculated with Grid 2 (Test case 3)

Mesh medium 200k			
$M_1 = 1.59$		$p_2/p_1 = 2.21$	
Parameter	**Exp.**	**S-A**	**STD** k-ε
β_1	57.9	58.3	58.5
β_2	60.2	61.2	60.9
ω	0.150	0.133	0.147

Table 5.22: Cascade parameters calculated with Grid 3 (Test case 3)

Mesh fine 500k			
$M_1 = 1.59$		$p_2/p_1 = 2.21$	
Parameter	**Exp.**	**S-A**	**STD** k-ε
β_1	57.9	58.3	58.5
β_2	60.2	61.2	60.9
ω	0.150	0.133	0.147

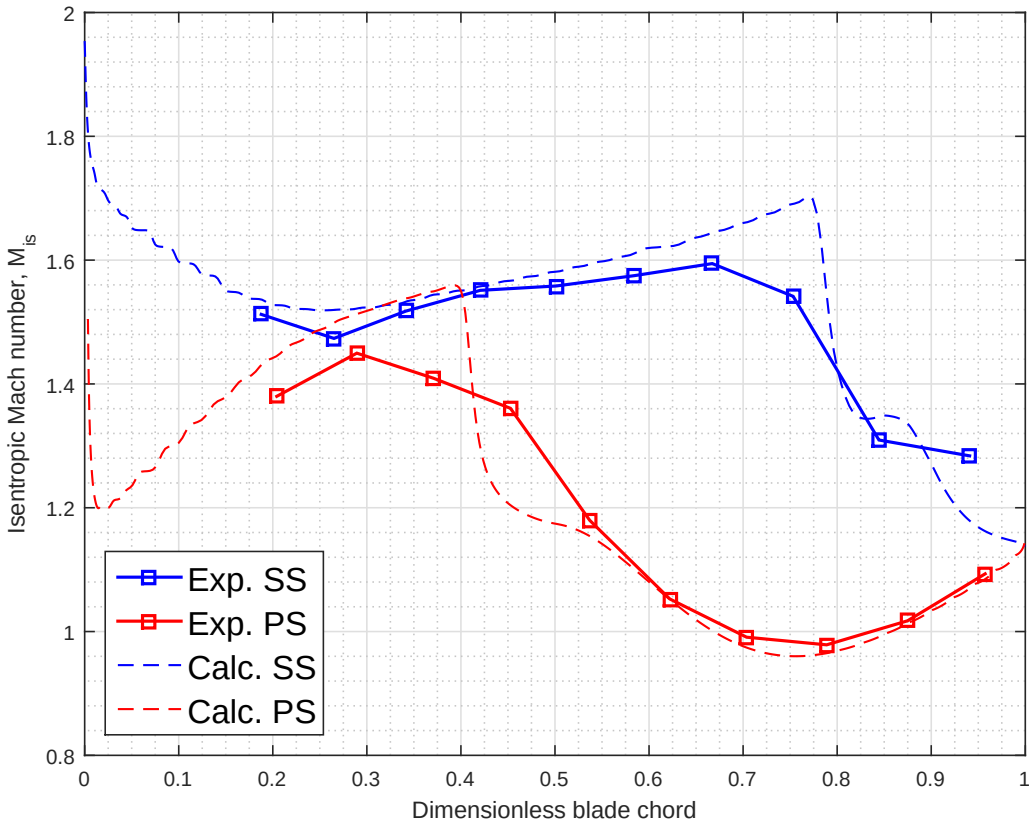

Figure 5.19: Distribution of isentropic Mach number using S-A model (Test case 3)

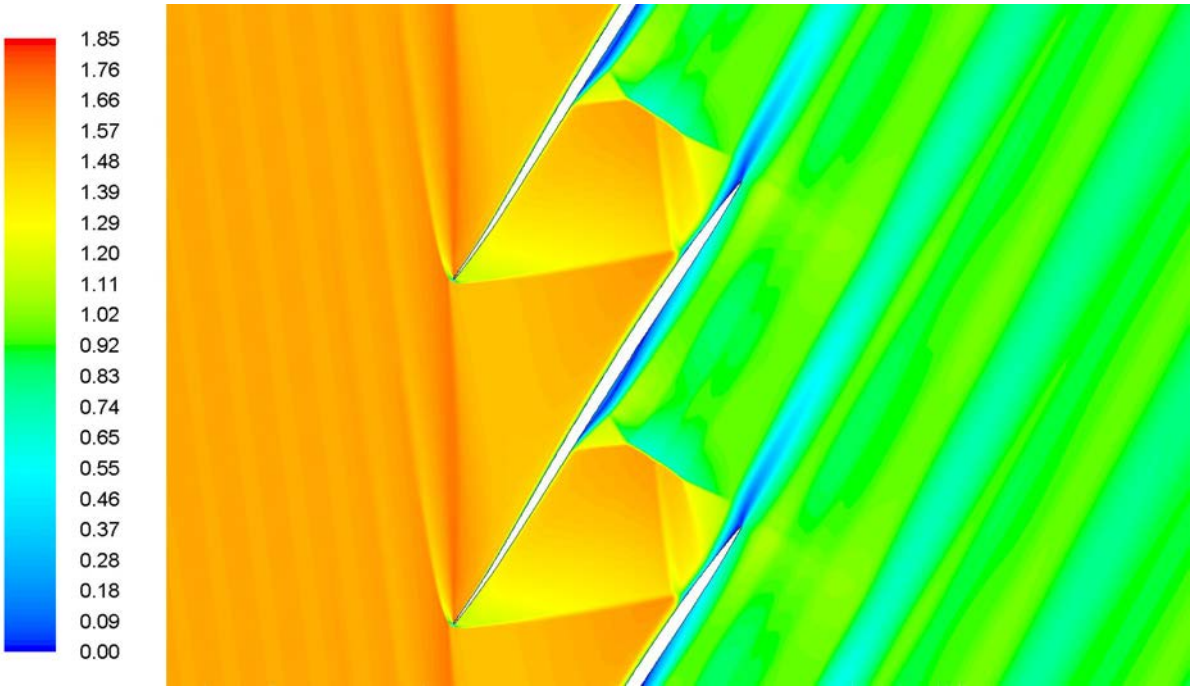

Figure 5.20: Mach number contours using S-A model (Test case 3)

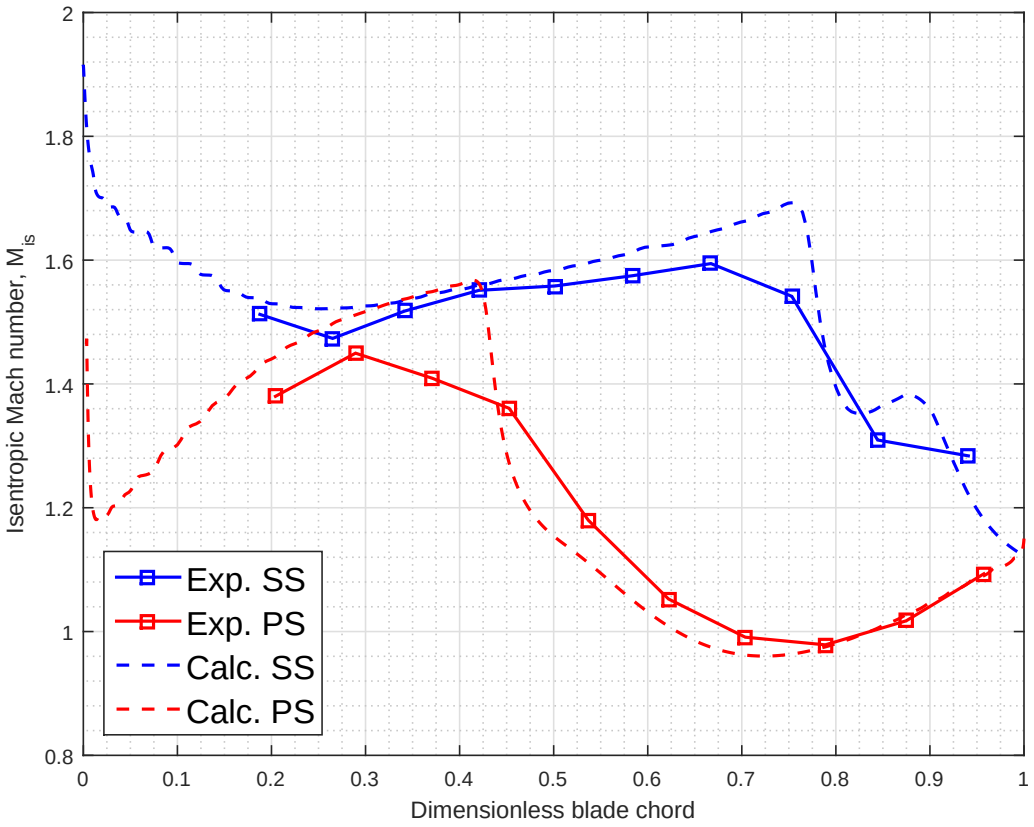

Figure 5.21: Distribution of isentropic Mach number using STD k-ε model (Test case 3)

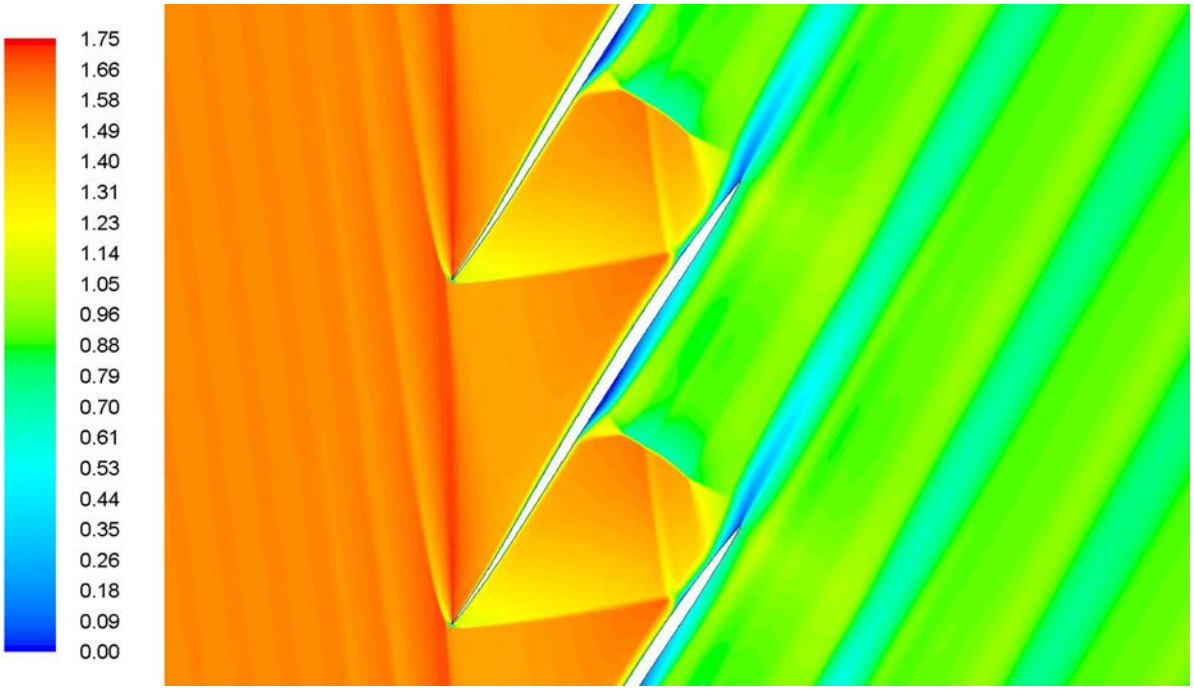

Figure 5.22: Mach number contours using STD k-ε model (Test case 3)

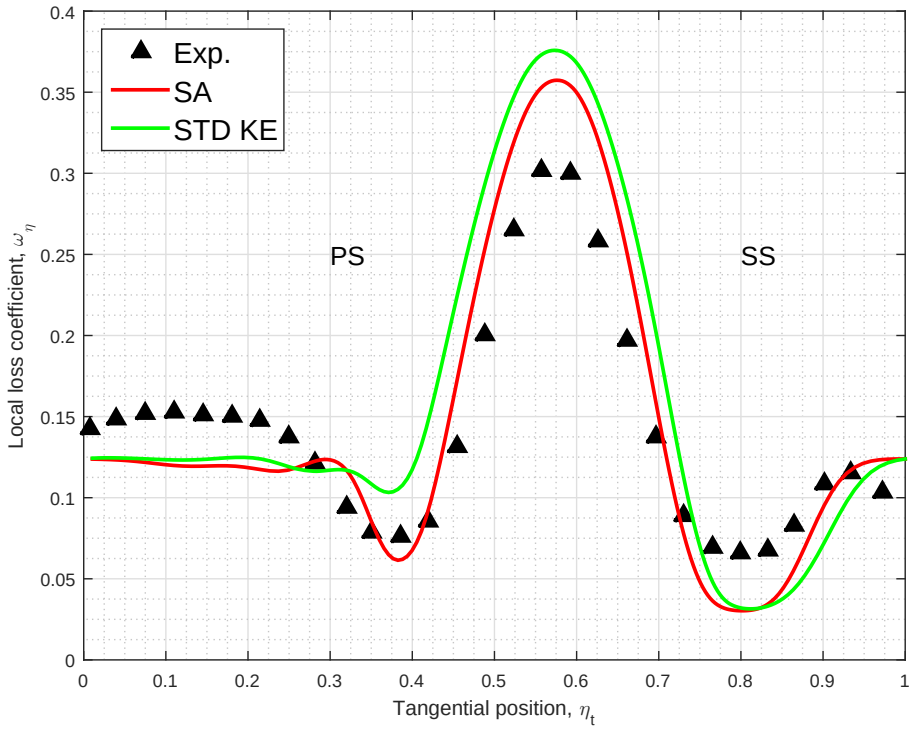

Figure 5.23: Wake total pressure loss profile (Test case 2)

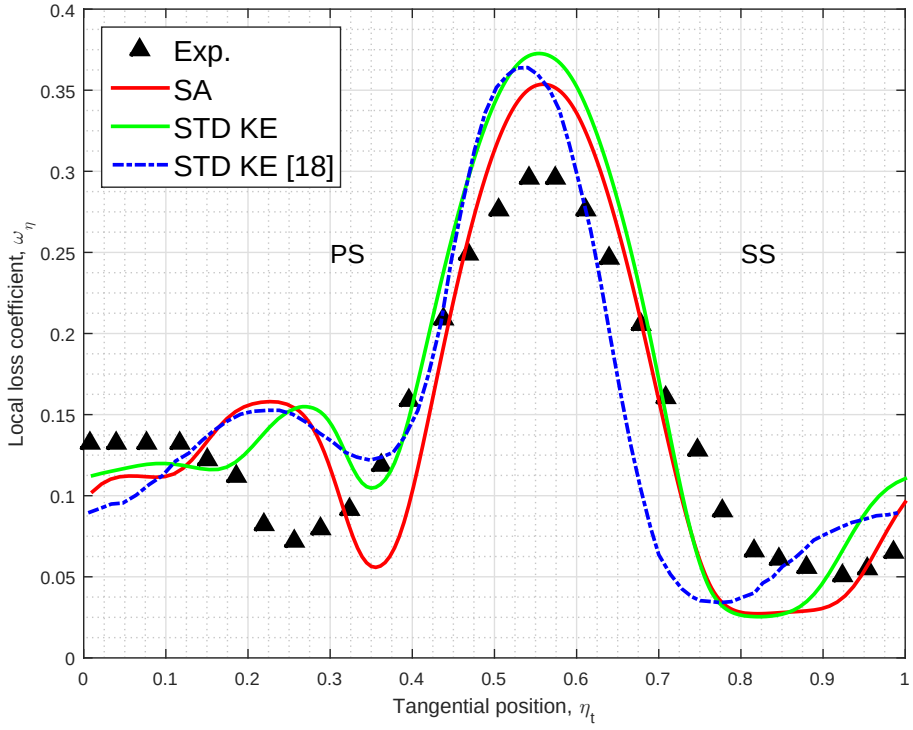

Figure 5.24: Wake total pressure loss profile (Test case 3)

5.3.6 Numerical shock-wave pattern and flow field

In order to further verify the accuracy of the validation study, a brief qualitative analysis of the shock-wave pattern has been performed. Even if Schlieren pictures of the shock-wave pattern for the analyzed test cases are not reported in [28], a quite exhaustive examination of the flow field in the cascade can be done in accordance with the typical shock-wave patterns which result from supersonic cascades experiments performed in wind tunnels. In Figure 5.25, a picture of the shock-wave pattern by means of the magnitude of the density gradient, that is a so-called numerical Schlieren picture, is reported. The figure on the left refers to the first test case, that is for an inlet Mach number of 1.58 and a static pressure ratio equal to 2.16. The figure in the center and the figure on the right refer to the second and the third test case respectively, that is for an inlet Mach number of 1.58 and 1.59 and a static pressure ratio equal to 2.12 and 2.21, respectively. A close up of the leading edge is also sketched in Figure 5.26. A detail of the shock wave pattern in the blade passage is reported in Figure 5.27.

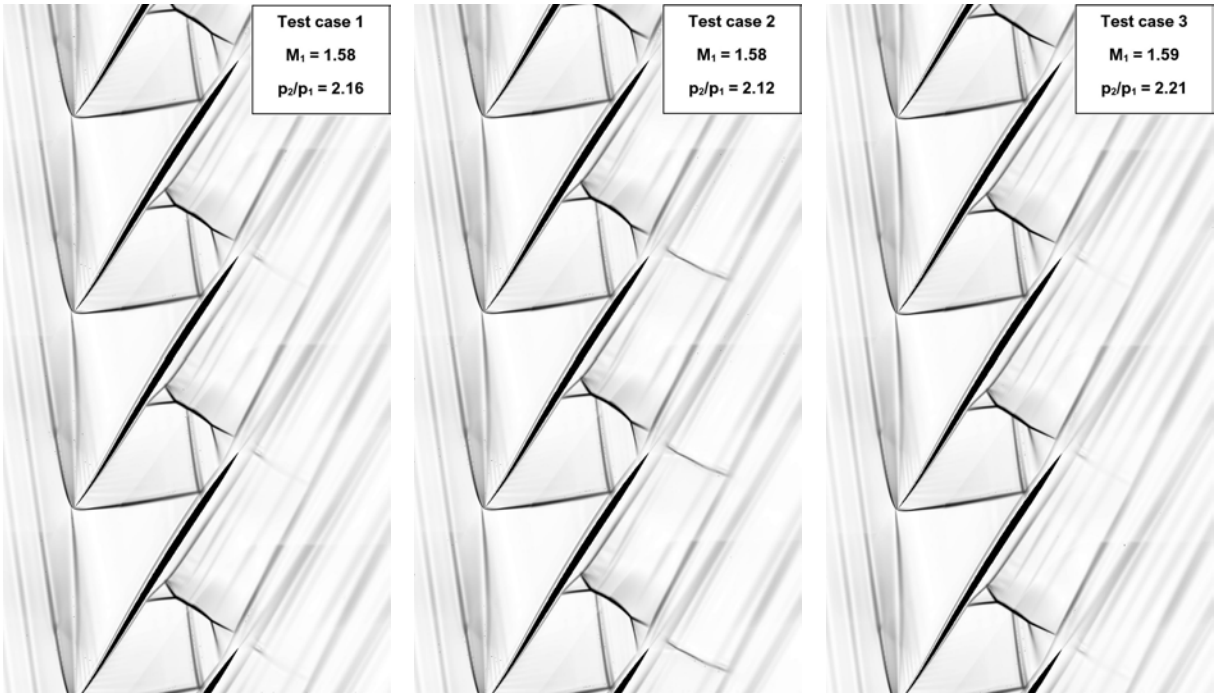

Figure 5.25: Numerical Schlieren pictures of the cascade for the three test cases

Figure 5.26: Numerical Schlieren picture of the leading edge: close-up of the bow shock and the precompression shock

Figure 5.27: Numerical Schlieren picture of the cascade: shockwave pattern in the blade passage

Even if the shock wave pattern varies according to blade geometry, cascade geometry, and operating conditions, as stated before, for cascades operating in unique incidence condition a typical configuration of shock waves and expansion waves can be identified. As previously described, the most common shock wave pattern in a S-shape cascade presents a first shock at the entrance of the cascade passage and a second shock located near the passage exit. First of all, it can be seen that the finite thickness of the leading edge develops a detached bow shock, as is to be expected. As stated before, two oblique shock branches depart from the bow shock, a weaker branch that extends into the region upstream of the cascade entrance plane and a stronger branch that runs into the passage and intersects the suction side of the adjacent blade. In this case, as is reported in [28], the intersection between the oblique shock in the passage and the suction side of the adjacent blade occurs at about 75% chord for values of static backpressure lower than or equal to the design backpressure. The location in which the shock wave encounters the adjacent blade and is reflected slightly varies according to the turbulence model used in the simulation. For example, running a simulation using the S-A model, the location has been roughly estimated to be at about 80% chord, so it is quite well predicted. The oblique shock in the foremost portion of the passage is strong enough that, impinging on the suction side of the adjacent blade, causes the detachment of the boundary layer. The upper portion of the bow shock affects the entire region in front of the other blades of the cascade and the resulting flow field is a distinctive feature of supersonic flows with subsonic axial Mach number in supersonic cascades. In fact, because of the periodicity of the cascade, there is a series of left-running waves extending in front of the entire cascade. The expansion waves at the leading edge are also well captured, as well as the pre-compression shock typical of this kind of cascade with S-shape profiles, which intersects the bow shock in front of the leading edge of the adjacent blade, as can be seen in Figure 5.26. The second passage shock at the outlet of the cascade passage is a normal shock wave, with a lambda shock at the end near the blade surface, originated by the strong shock wave-boundary layer interaction in that region.

Chapter 6

Parametric study of ARL-SL19 supersonic cascade

In this chapter, the parametric study of the ARL-SL19 supersonic cascade is presented. The main independent variables in a parameteric study are *flow variables*, that is the inlet Mach number, the static pressure ratio, and the axial velocity-density ratio (AVDR), or *geometric parameters*, such as the cascade solidity. All of these parameters strongly influence the cascade performance. Dependent variables are the exit Mach number, the mean exit flow angle, and the total-pressure loss coefficient. The inlet flow angle is also a dependent variable which must be determined, since it is a function of the inlet Mach number because of the unique incidence. The outcomes are presented for different operating conditions. Numerical data were obtained over a range of different inlet Mach numbers, static pressure ratios, and solidity values. Since the AVDR is not a parameter in a two-dimensional simulation, only the inlet Mach number, the static pressure ratio, and the cascade solidity were tested.

The presentation of the results obtained from the parametric study is organized into five sections. The first section considers the cascade design operating condition: the cascade behaviour is analyzed at design condition and the results in terms of performance and shock pattern are compared with the available experimental data. The second section is about the numerical determination of the cascade unique incidence operating condition: the numerical unique incidence curve for the cascade is determined by points and compared with the theoretical curves reported in [28]. The last three sections are concerned with the parametric study of the cascade: the influence of the main flow and geometric variables, that is inlet Mach number, static pressure ratio, and solidity, on the overall cascade performance is investigated.

6.1 Analysis of cascade design operating condition

The cascade design operating condition has been widely examined in order to further verify the accuracy of the simulations and the correctness of the choice of the turbulence model. Moreover, a detailed numerical knowledge of the cascade design operating condition is necessary for the subsequent analysis. At design point condition ($M_1 = 1.612$, $p_2/p_1 = 2.15$, AVDR= 1.00), the total-pressure loss coefficient and the mean exit flow angle, determined experimentally in [28], are 0.143 and 61.0°, respectively. The measured inlet flow angle associated with the unique incidence condition is 57.6°. The calculated flow turning between the cascade inlet and the cascade outlet ($\Delta\beta = \beta_1 - \beta_2$) is of −3.4°. The experimental inlet and outlet parameters determined at design operating condition are summarized in Table 6.1. As it can be noted, the AVDR at design condition is unity, so this operating condition is particularly suitable for being analyzed with a 2D simulation. A sketch of the approximate wave pattern at the cascade entrance region at the design inlet Mach number is shown in Figure 6.1, taken form [28], with an estimation of the Mach number in certain points of the cascade passage, such as at the leading-edge, dowstream of the precompression shock, and upstream of the first-passage shock.

Table 6.1: Design parameters of ARL-SL19 supersonic cascade

Cascade design parameters			
Input		**Output**	
M_1	1.612	M_{ax}	0.87
p_2/p_1	2.15	ω	0.143
β_1	57.6°	β_2	61.0
$AVDR$	1.00	$\Delta\beta$	−3.4°

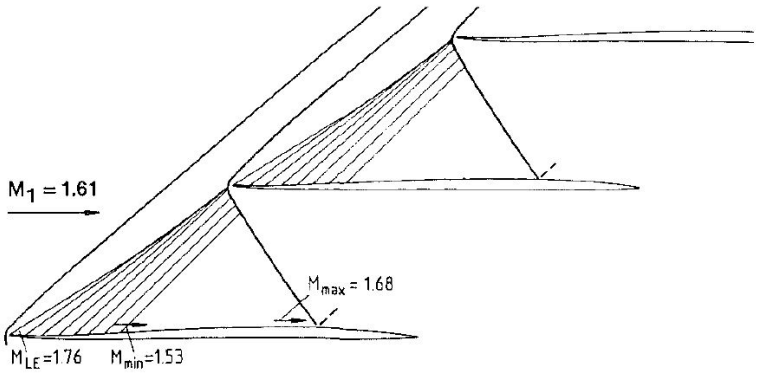

Figure 6.1: Approximate wave pattern at design inlet condition

The CFD results obtained at the cascade design operating condition, calculated using the S-A model, are reported in Table 6.2 and compared with the experimental data listed above.

Table 6.2: CFD results for cascade design operating condition

$M_1 = 1.612$	$p_2/p_1 = 2.15$	$AVDR = 1.00$
Parameter	**Exp.**	**Calculation**
β_1	57.6	58.2
β_2	61.0	61.6
$\Delta\beta = \beta_1 - \beta_2$	$-3.4°$	$-3.4°$
ω	0.143	0.142
M_{ax}	0.87	0.85

The CFD results are in quite total agreement with the experimental data.
As regards the inlet flow angle and the mean exit flow angle, the numerical values are shifted to higher values than the experimental ones. The reason behind this difference between the measured inlet flow angle and the calculated inlet flow angle, and as a conseguence between the measured mean exit flow angle and the calculated mean exit flow angle, has already been pointed out. The calculated flow turning is well predicted anyway ($-3.4°$). The fact that the calculated mean inlet flow angle is slightly higher than the experimental value affects the value of the calculated axial component of the inlet Mach number, which is slightly lower than the experimental one.
The total-pressure loss coefficient calculated with the S-A model corresponds to the experimental one (the relative percentage error is of about 1%). In comparison, the corresponding total-pressure loss coefficient calculated by using the STD k-ε was 0.154, which is clearly overpredicted. This result confirms the tendency of the STD k-ε to overpredict the total-pressure loss coefficient. Hence, the choice of the S-A model as the turbulence model for the parametric study derived from the validation has been confirmed as being correct.
The Mach number contours at cascade design operating condition are shown in Figure 6.2. As it can be noted from Figure 6.1, the theoretical Mach number at the leading edge is reported to be 1.76, with a corresponding maximum Mach number of 1.68 near the suction side upstream of the oblique shock wave inside the blade passage. The calculated Mach number at the leading edge and the maximum Mach number are 1.87 and 1.69, respectively.

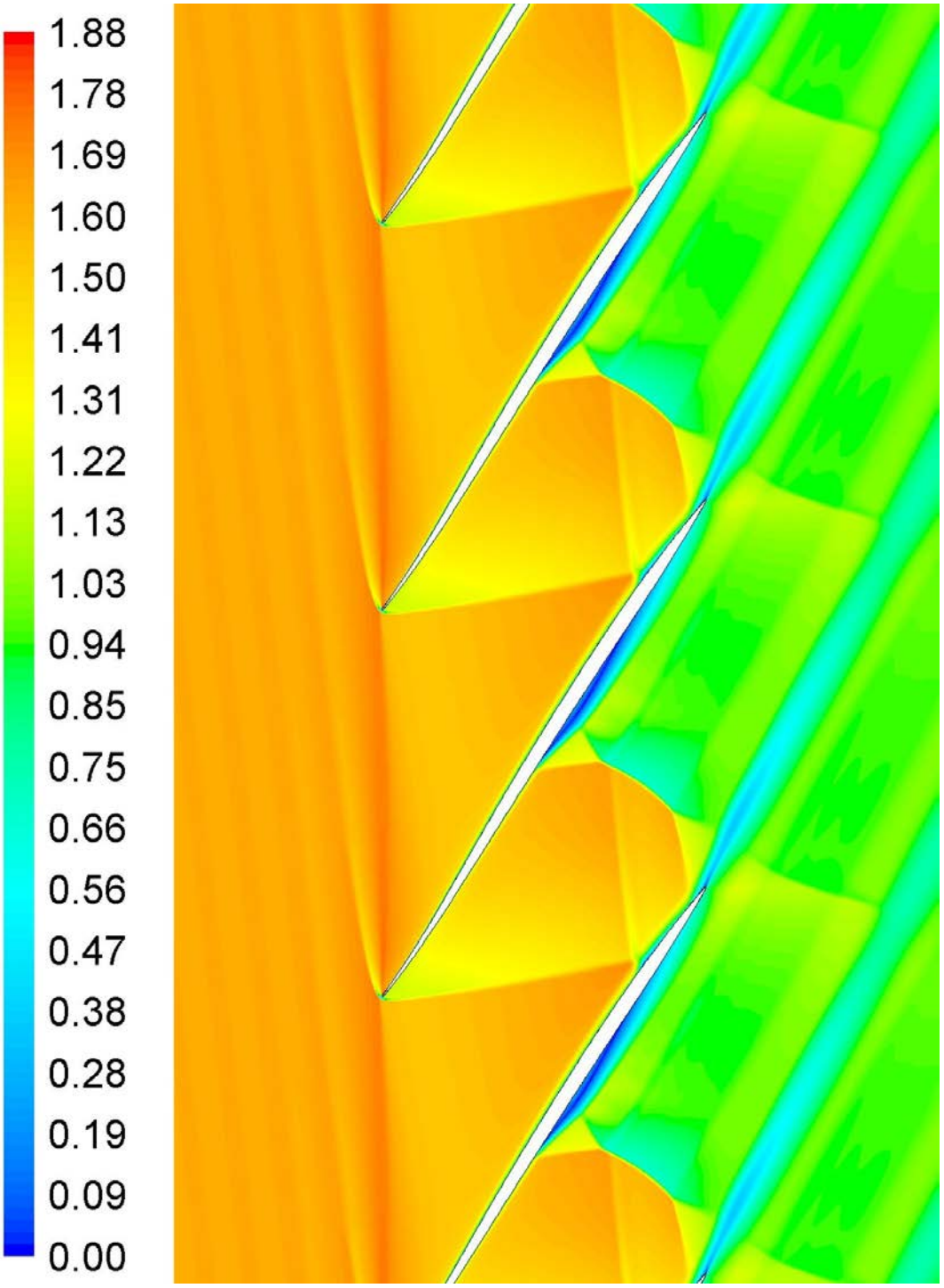

Figure 6.2: Mach number contours at design operating condition

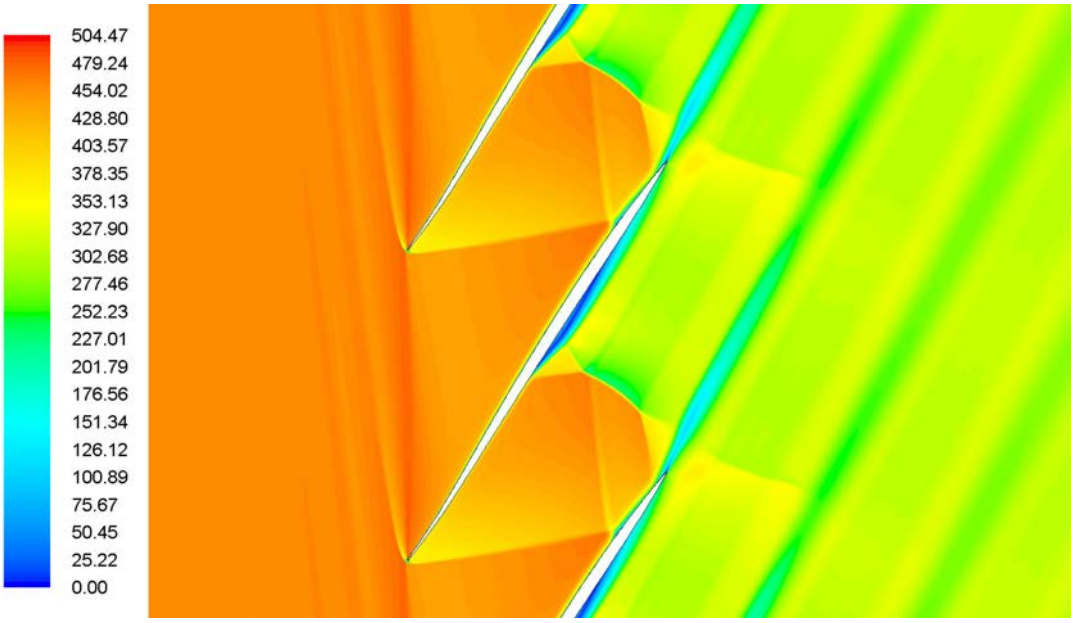

Figure 6.3: Velocity magnitude contours at design operating condition

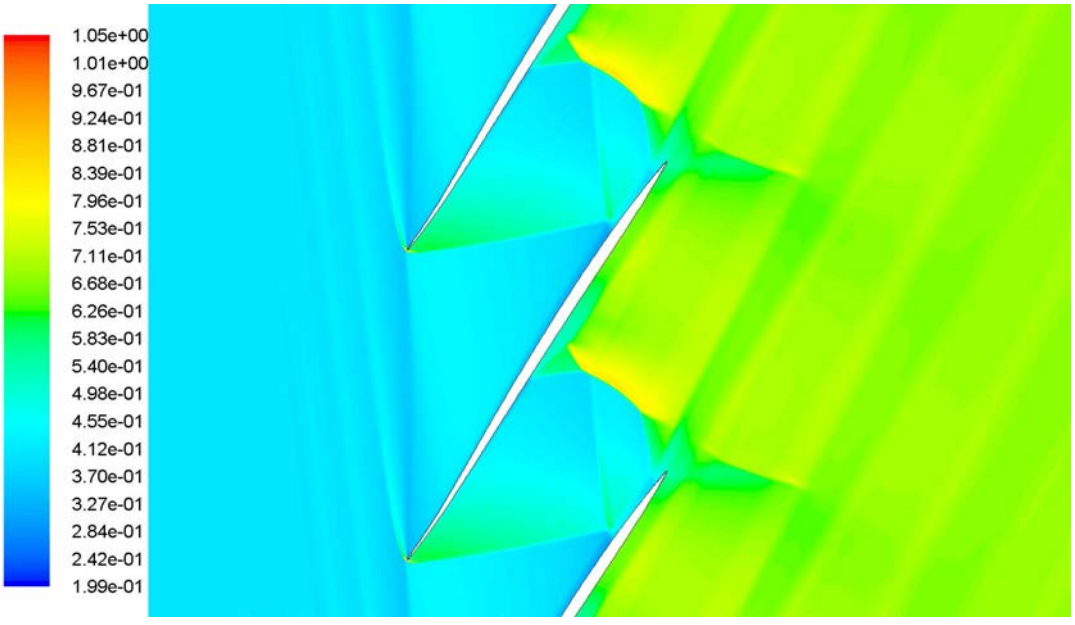

Figure 6.4: Density contours at design operating condition

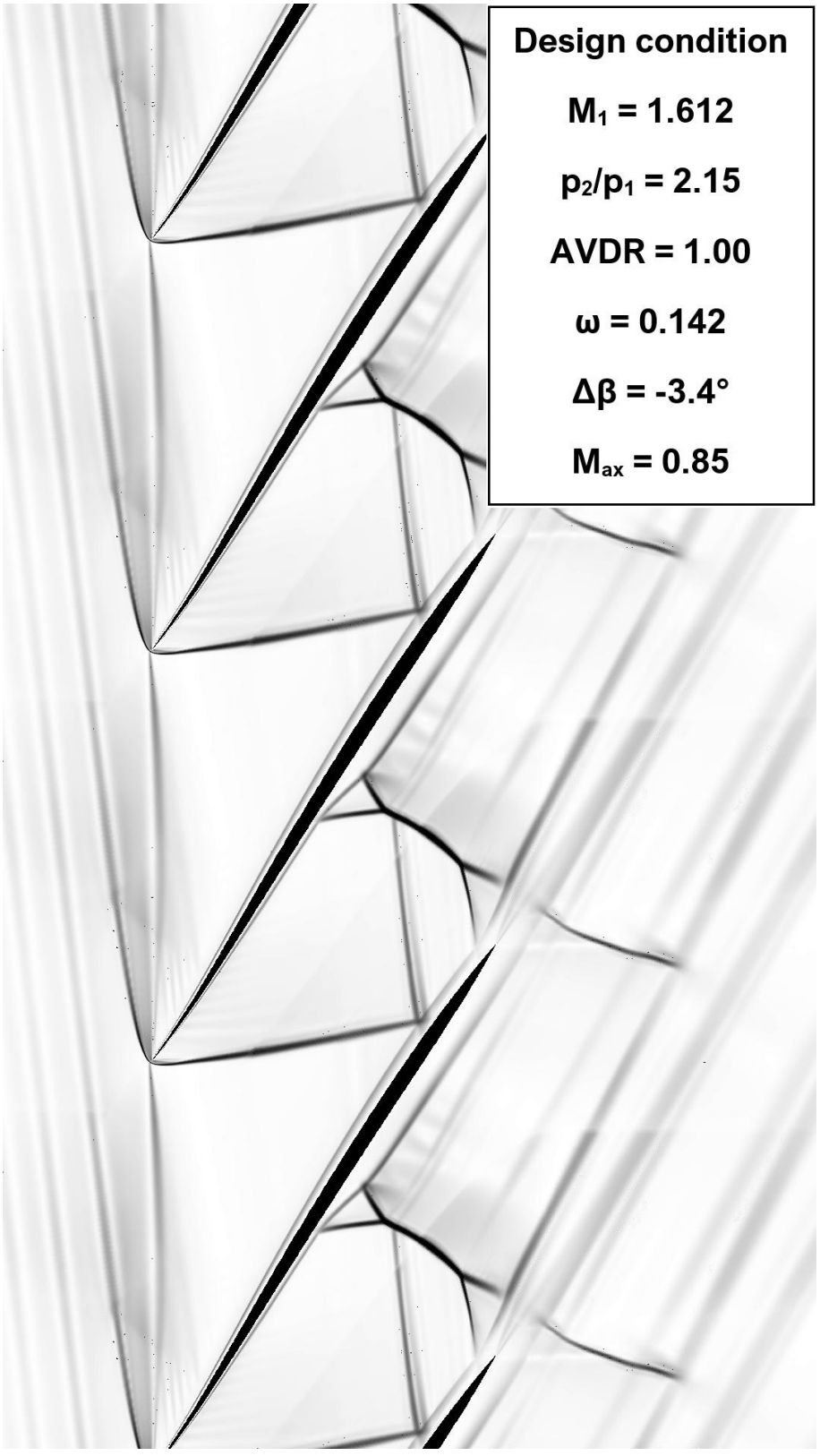

Figure 6.5: Shock-wave pattern in the cascade at design operating condition

6.2 Numerical determination of the unique incidence curve

As widely discussed before, a supersonic cascade flow with a subsonic axial component implies a dependency of the inlet flow angle on the inlet Mach number. The unique incidence curve for the ARL-SL19 cascade has been numerically calculated for several inlet Mach numbers and compared with the theoretical unique incidence curve determined in [28] by using an analytical method. The theoretical unique incidence curves for the present cascade, reported in [28] and determined following the analytical method developed in [27], are shown in Figure 6.6. The points identified by triangular markers represent the experimental values. The curves identified by solid-lines were calculated considering approximated losses due to the leading-edge bow shock, which determines a lower axial Mach number. The curves identified by the dashed lines were calculated neglecting these losses, as reported in [28].

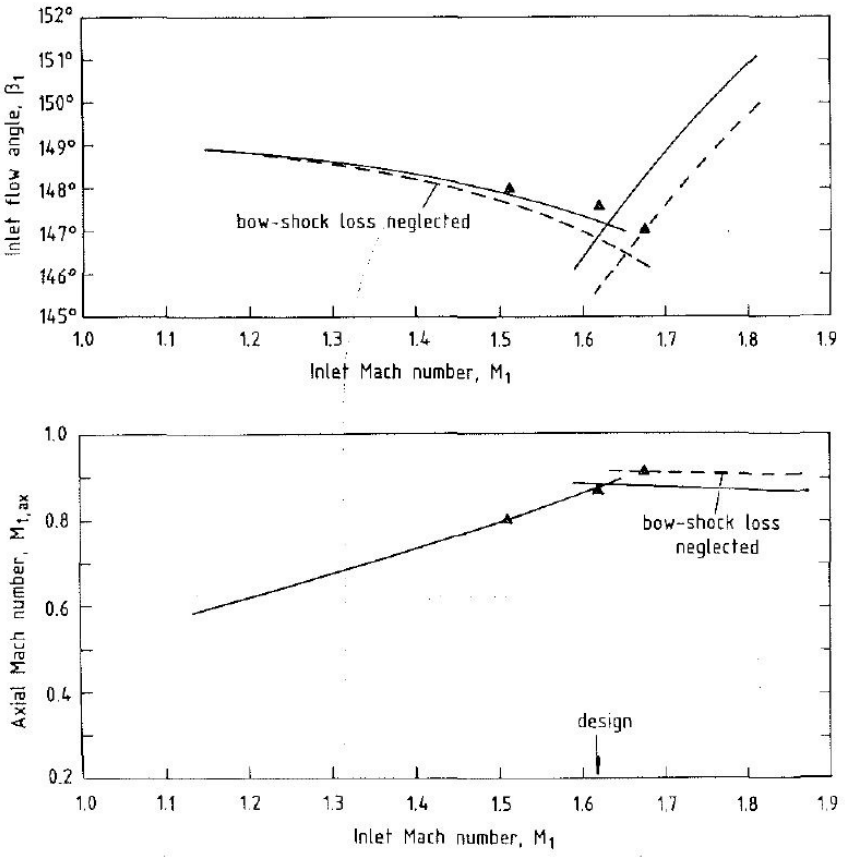

Figure 6.6: Analytical and experimental unique incidence curves for ARL-SL19 supersonic cascade

The Mach numbers imposed for determining the numerical unique incidence curve were in the range 1.32 to 1.71. The unique incidence condition has been numerically determined with a simple iterative approach, that is for an imposed Mach number the inlet flow angle has been slightly varied until the difference between the calculated inlet Mach number and the imposed inlet Mach number was below a certain threshold. The numerical inlet flow angles and the corresponding inlet axial Mach numbers calculated for each inlet Mach number in the range specified above are listed in Table 6.3.

Table 6.3: Numerical inlet flow angle and corresponding inlet axial Mach number for the unique incidence condition

Inlet Mach number	**Inlet flow angle**	**Axial Mach number**
M_1	β_1	M_{ax}
1.32	59.3	0.67
1.40	59.1	0.72
1.51	58.7	0.79
1.58	58.4	0.83
1.612	58.2	0.85
1.71	59.4	0.88

The comparison of the numerical, the analytical, and the experimental unique incidence curves is reported in Figure 6.7. The point identified by a diamond marker represents the measured inlet flow angle and the axial Mach number at design operating condition. The comparison of the calculated, the experimental, and the theorical axial Mach number curves, is reported in Figure 6.8. Let first consider Figure 6.7. As it can be seen, the agreement among measured, predicted, and calculated values for the inlet flow angle is quite good. The measured inlet flow angle at the design inlet Mach number is 57.6°, against a predicted theoretical value of 57.2°. The numerical inlet flow angle at the design inlet condition is 58.2°. This difference, as discussed before, is due to the turbulence model and the way in which the grid guides the flow, that is related to mesh quality. The percentage error is about 1%. If we take a look at Figure 6.8, the agreement between the experimental and the calculated values is quite good also in this case, with a measured axial inlet Mach number of 0.87 at design, against a calculated value of 0.85. The percentage error in this case is about 2%. The numerical unique incidence curve is similar to the one reported in [17] and sketched in Figure 3.16. The differences between the two diagrams are obviously due to the fact that the unique incidence condition depends on the blades thickness, the suction side curvature, and the stagger angle.

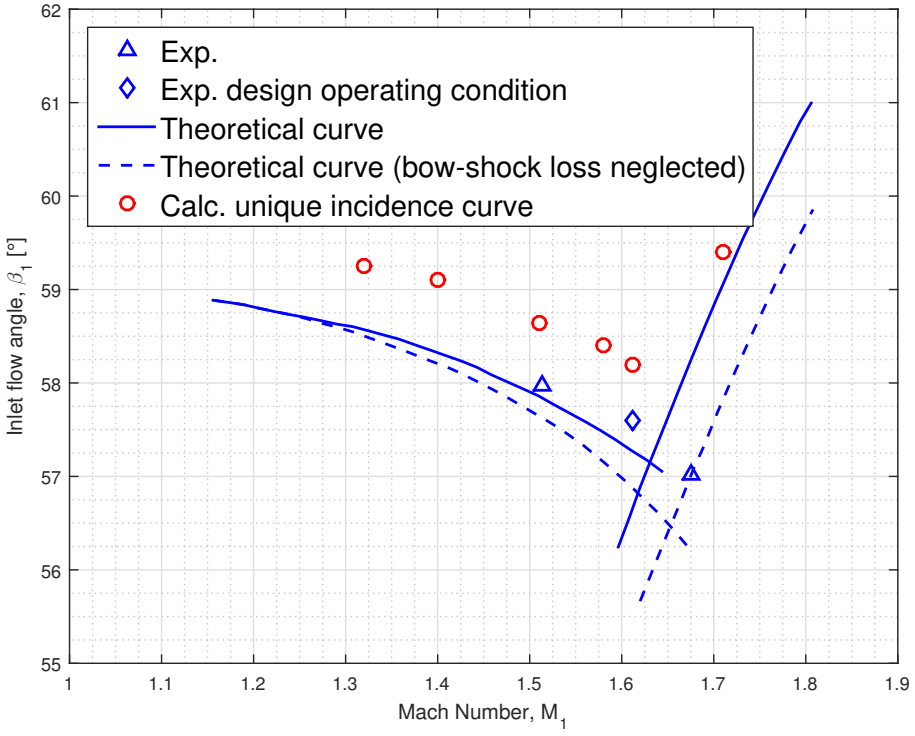

Figure 6.7: Unique incidence curves of ARL-SL19 supersonic compressor cascade

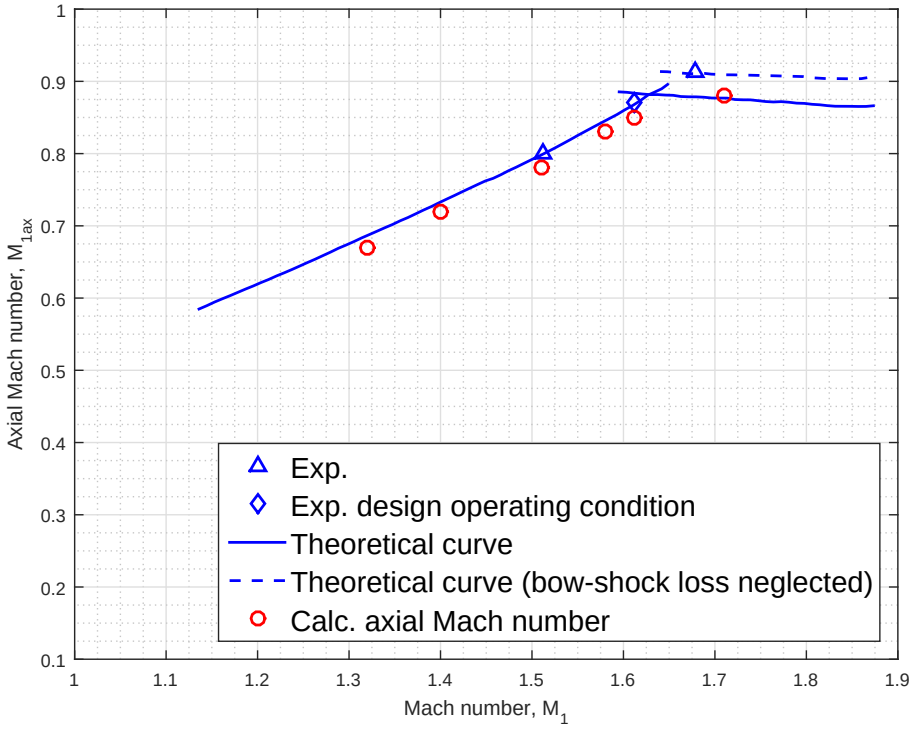

Figure 6.8: Inlet axial Mach number curves

Calculations of local Mach number and local flow angle for an inlet Mach number of 1.51 were performed. The inlet measurement plane was located at 1.54 mm upstream of the cascade inlet plane. The results were compared with the experimental and theoretical data reported in [28], as can be seen in Figure 6.9. The curves for local inlet Mach number and local inlet flow angle plotted with dashed lines represent the solution obtained by applying the expansion fan equations at the leading-edge of the airfoil, that is the theoretical solution obtained by applying the Prandtl-Meyer relation. The vertical curves drawn with dashed lines represent the location where the bow shock waves and precompression shock intersect the measurement line in the CFD simulation and the measurement plane in the experiments. The calculated results are in fairly good agreement with both the theoretical results and the experimental results.

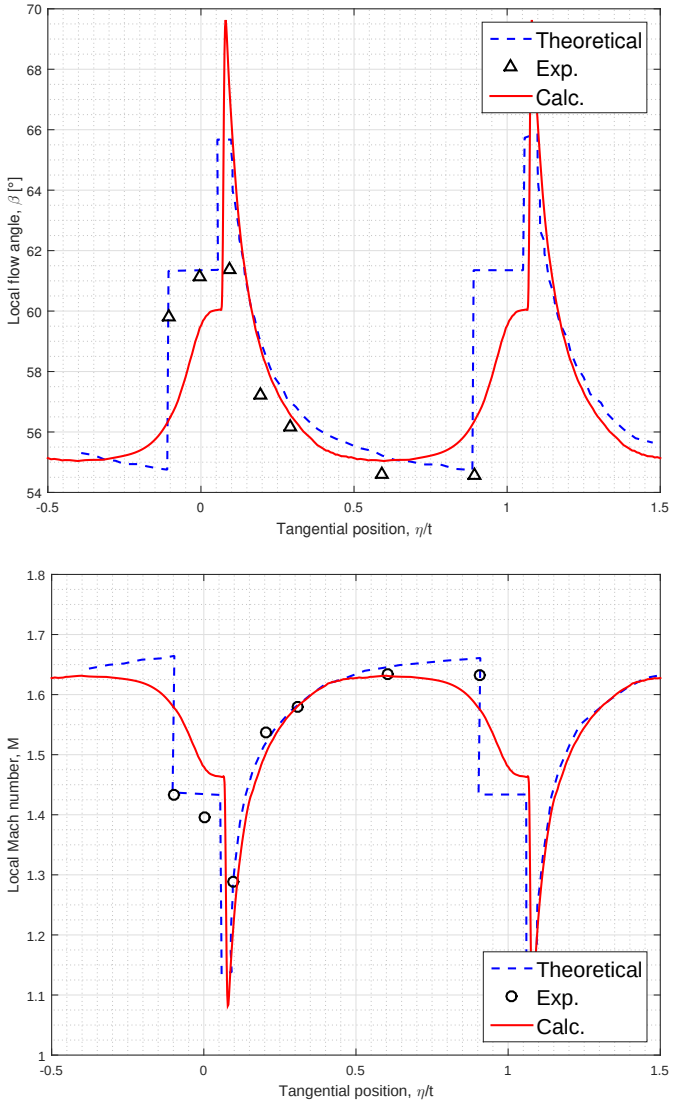

Figure 6.9: Local inlet flow angle and inlet Mach number ($M_1 = 1.51$)

6.3 Influence of inlet Mach number

The inlet Mach number is one of the most important parameters which influence the performance of a supersonic compressor cascade. The quantity which is mainly influenced by the inlet Mach number is the maximum static pressure ratio achievable by the supersonic compressor cascade. In order to investigate the influence of the inlet Mach number on the maximum static pressure ratio, a series of simulations were carried out, identifying the maximum static pressure ratio achievable for each imposed Mach number. The total-pressure loss coefficient corresponding to each maximum static pressure ratio was calculated. Five Mach numbers were investigated, varying the static pressure ratio until the maximum value were achieved, that is when a quasi-normal shock wave was exactly at the passage entrance. The influence of inlet Mach number on the maximum achievable static pressure ratio and the related total-pressure loss coefficient is reported in Figure 6.10 and Figure 6.11. The results were graphically compared with the interpolation line of the available experimetnal data reported in [28]. The maximum achieved static pressure ratio and the corresponding total-pressure loss coefficient for each inlet Mach number are listed in Table 6.4.

Table 6.4: Calculated maximum static pressure ratio and corresponding total-pressure loss coefficient

Mach number	**Max. static pressure ratio**	**Total-pressure loss coefficient**
M_1	p_2/p_1	ω
1.32	1.9	0.064
1.40	2.06	0.077
1.51	2.30	0.109
1.58	2.47	0.129
1.612	2.53	0.138

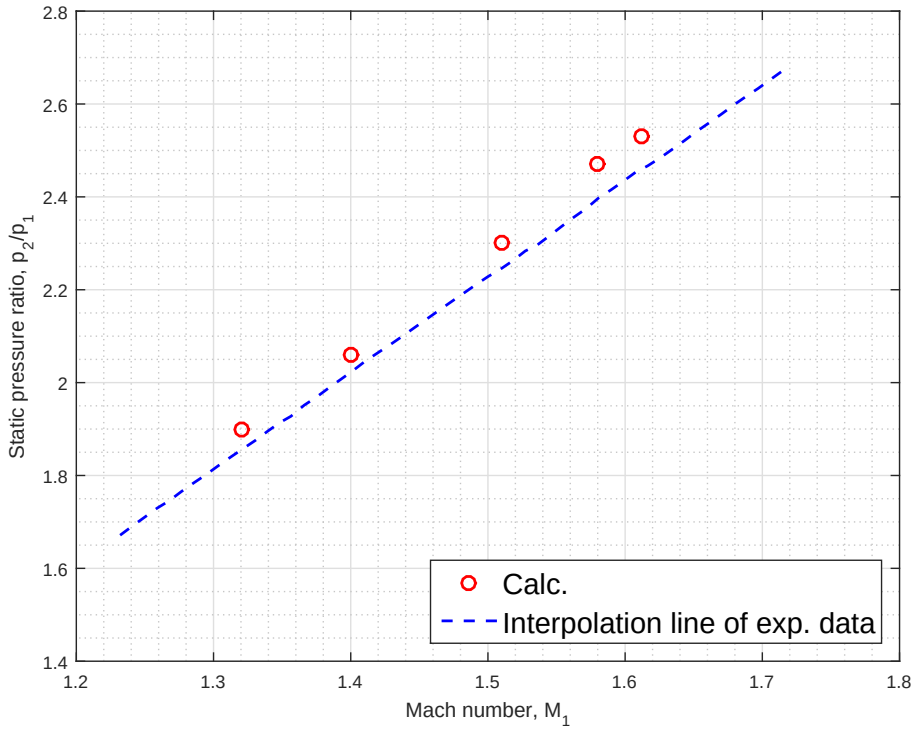

Figure 6.10: Influence of inlet Mach number on maximum static pressure ratio

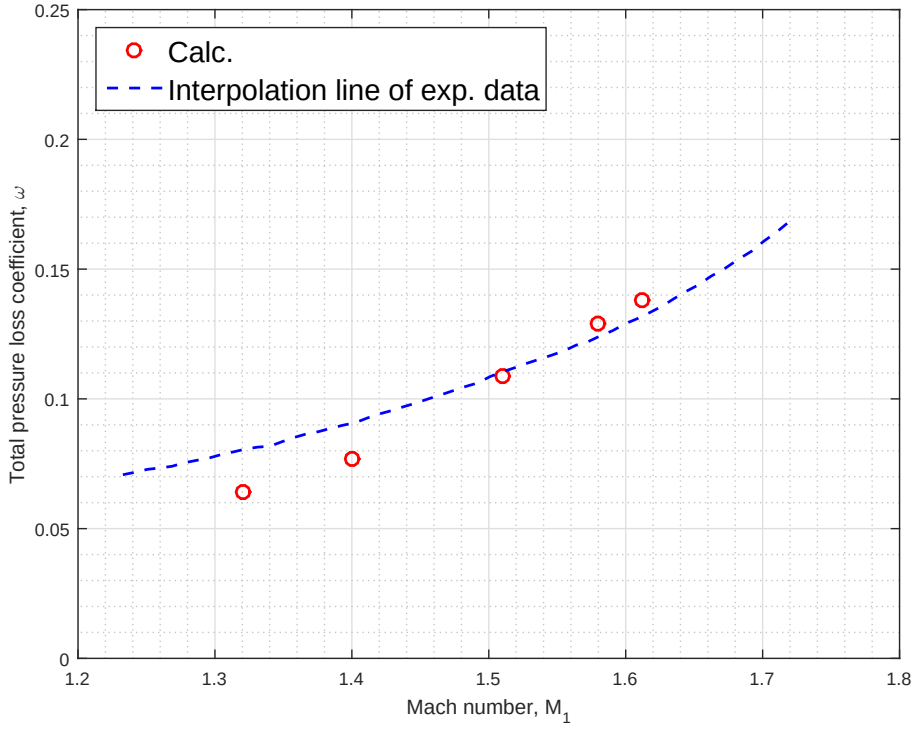

Figure 6.11: Influence of inlet Mach number on total-pressure loss coefficient

First of all, lets take a closer look at the influence of inlet Mach number on the maximum static pressure ratio achievable by the cascade. The results show an evident trend according to which increasing inlet Mach number corresponds to an increase of the maximum static pressure ratio. The interpolation of the experimental data shows a linear dependence of maximum achievable static pressure ratio on inlet Mach number and this trend is reproduced by the CFD results in a satisfactory manner. For lower inlet Mach numbers (1.32-1.40), the maximum static pressure ratio achievable by the cascade is well predicted. For moderate inlet Mach numbers (1.51) and higher inlet Mach numbers (1.58-1.612), the maximum static pressure ratio is slightly overestimated (by around 2%). For example, a maximum static pressure ratio of 2.47 was obtained experimentally at the design inlet Mach number (1.612), against a maximum pressure ratio of 2.53 calculated via CFD. This slight mismatch is due to the turbulence model employed in the simulations, which has a tendency to not exactly predict the position of the shock waves inside the blade passage. Even if the effective static backpressure at which the cascade is operating corresponds to the imposed one, the different location of the shock waves influences the outcomes, because the shock waves are estimated to be further back than they are. This in turn causes the cascade to operate at static pressure ratios beyond the experimental maximum static pressure ratio, that is beyond the experimental spill point, even if the cascade still operates in unique incidence condition. The relative percentage error in overestimating the maximum static pressure ratio achievable by the cascade is within the model tolerance limits anyway. Lastly, according to both the experimental and the related numerical trend, it can be noticed that increasing inlet Mach number determines an increase in the range of static pressure ratios at which the cascade, or the corresponding compressor rotor stage, can operate.

As regards the influence of the inlet Mach number on the total-pressure loss coefficient, the results show that increasing inlet Mach number corresponds to an increase of the total-pressure loss coefficient. This is quite obvious, because increasing Mach number causes an increase in strength of the shock waves and, as a consequence, a corresponding increase of the shock losses. Moreover, the stronger interaction between shock waves and the boundary layer causes an increment of viscous losses, due to the separation of the boundary layer. The CFD results quite well predict this trend. The total-pressure loss coefficients calculated for the experimental maximum static pressure ratio are quite well calculated, also taking into account the quite high measurement uncertainties and the different method with which the total-pressure loss coefficient was determined in the reference article. We can distinguish two different sets of calculated total-pressure loss coefficients for each inlet Mach number: the former includes the total-pressure loss coeffi-

cients calculated at the experimental maximum static pressure ratio; the latter groups the total-pressure loss coefficients calculated at the maximum static pressure ratio determined via CFD, which is slightly different. The total-pressure loss coefficient obtained in [28] at the design inlet Mach number for the experimental maximum static pressure ratio (2.47) was 0.130 (AVDR= 1.18), against a calculated total-pressure loss coefficient of 0.133 at the corresponding static pressure ratio (with a 2% margin of error). The main reason why the calculated total-pressure loss coefficient is slightly higher than the experimental total-pressure loss coefficient can be due primarily to the different value of the AVDR: in fact, increasing the AVDR for moderate to high static pressure ratios, that is above the design static pressure ratio, causes a reduction in loss. Differentiating two sets of data for the total-pressure loss coefficient gives a better meaning to the comparison between the available experimental data and the CFD results. At very high inlet Mach numbers, that is far beyond the design value, the total-pressure loss coefficient calculated via CFD at the corresponding experimental maximum pressure ratio results overestimated. For example, at an inlet Mach number of 1.71, for the experimental maximum static pressure ratio of 2.61, the calculated total-pressure loss coefficient was 0.161, against a total-pressure loss coefficient of 0.183 determined via CFD. This significant difference is essentially due to the boundary layer separation caused by the strong shock wave-boundary layer interaction, which determines an increase in the viscous losses. Moreover, this large boundary layer separation pushes the turbulence model over its limits of application.

It is necessary to specify that the results refer to a supersonic cascade slightly different from the experimental one tested in [28]. In fact, three main differences must be underlined: the non-periodicity of the experimental cascade, that is the finite number of blades; the fact that the cascade model is two-dimensional, that is AVDR is unity; the total absence of secondary flows phenomena and disturbances in the flow due to the presence of measurement instruments and equipments. Moreover, the value of the AVDR for the experiments, carried out in [28] for determining the maximum static pressure ratio and the corresponding total-pressure loss coefficient varying the inlet Mach number, is not reported, so a complete consistency between the numerical results and the experimental data is not ensured. To summarize, we can draw some conclusions of a general nature: increasing inlet Mach number corresponds to an increase of the maximum static pressure ratio and the total-pressure loss coefficient.

6.4 Influence of static pressure ratio

Varying the static backpressure at a fixed inlet condition, that is for a fixed inlet Mach number and a corresponding inlet flow angle determined by the unique incidence condition, modifies the shock wave pattern inside the cascade passage and the exit flow field, in terms of mean exit flow angle and exit Mach number. The overall performance, in terms of total-pressure loss coefficient, is influenced as well. The procedure for investigating the influence of the static pressure ratio on the other cascade parameters was to set the inlet Mach number and then increase gradually the static pressure ratio from low values to the maximum value achievable by the cascade while mantaining periodicity, that is the unique incidence condition. Five nominal inlet Mach numbers have been investigated.

Experimentally, varying the AVDR independently of the static pressure ratio is not possible. In fact, static backpressure and AVDR are closely related to each other, since varying the former influences the latter. As stated in [28], increasing the static pressure ratio between the cascade entrance and the cascade exit is always followed by an increase in the AVDR. Increasing the backpressure causes a considerable thickening of the boundary layer and an enlargement of the wake width, with a corresponding reduction of the passage between two adjacent blades. For that reason, the reference experimental data obtained in [28] were affected by some scatter, due to the simultaneous increase of AVDR with static pressure ratio. Hence, an effort to separate the influence of the AVDR and the static pressure ratio on the main exit variables was made in [28]. The curves for the exit Mach number, the exit flow angle, and the total-pressure loss coefficient reported in [28] are referred as "semi-empirical" curves and were obtained by applying the conservation equations of gas dynamics (continuity, momentum, and energy) to a quasi-three-dimensional control volume (assuming blade-to-blade periodicity). The mathematical procedure which led to these semi-empirical curves for the main exit variables, reported in Figure 6.12, is widely described in [28]. These curves can be useful for a qualitative comparison with the numerical results, but some caution should be used if these curves are applied in a quantitative manner, since they are the results of a manipulation of the experimental data. Moreover, the curves refer just to a single inlet Mach number and inlet flow angle. The AVDR in the simulations is always unity, so the results obtained via CFD are affected only by the static pressure ratio. For that reason, the comparison between the CFD and the experimental results must be done even more carefully, since the experimental data were manipulated and some aspects may have been disregarded.

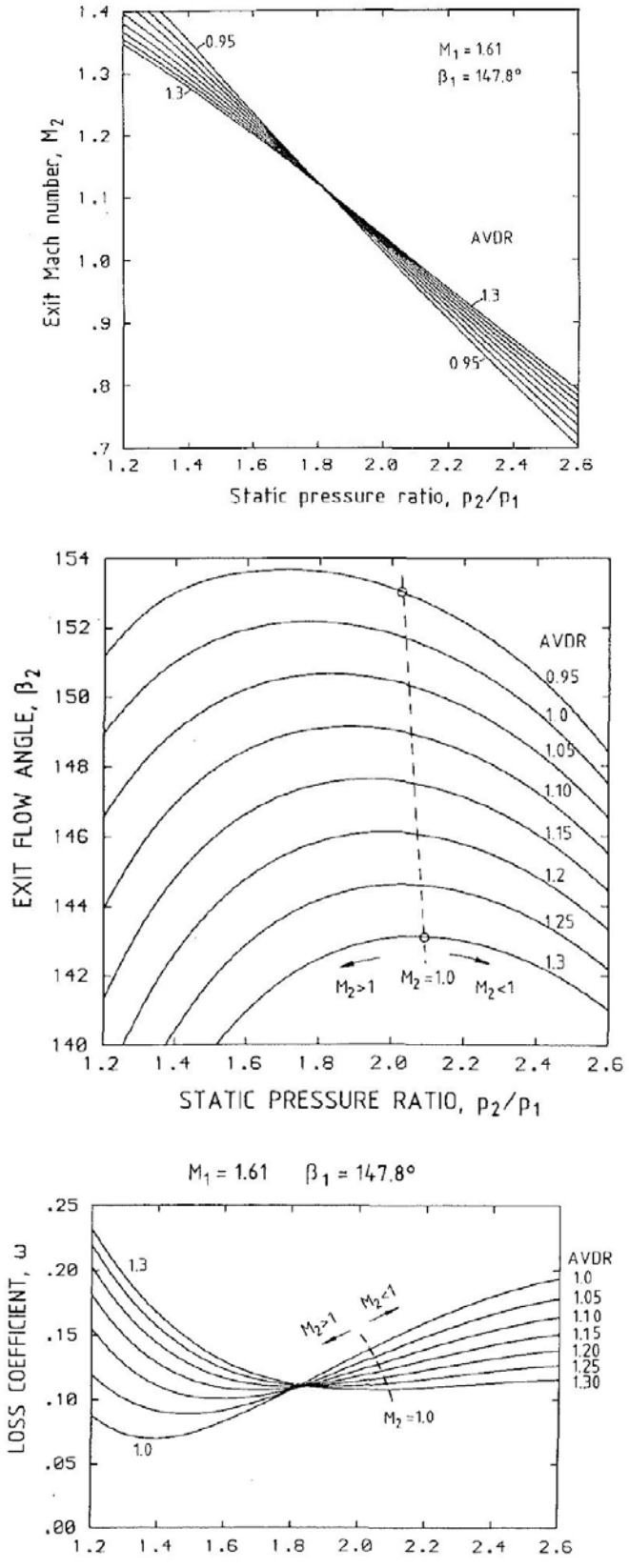

Figure 6.12: Semi-empirical curves showing the influence of static pressure ratio and AVDR on the main cascade exit variables

This section is organized into three main subsections: the first one is concerned with the influence of static pressure ratio on exit Mach number; the second one considers the influence of static pressure ratio on the mean exit flow angle and the flow turning; the third one deals with the influence of the static pressure ratio on cascade performance, in terms of total-pressure loss coefficient.

6.4.1 Exit Mach number

The influence of the static pressure ratio on the exit Mach number is reported in Figure 6.13. The curves in Figure 6.13 clearly reveal a linear dependence of the exit Mach number on the static pressure ratio and this trend reflects the one reported in [28]. Moreover, the CFD results show that increasing inlet Mach number, for a fixed static pressure ratio, corresponds to an increase in exit Mach number, while increasing static pressure ratio, for a fixed inlet Mach number, corresponds to a decrease of the exit Mach number.

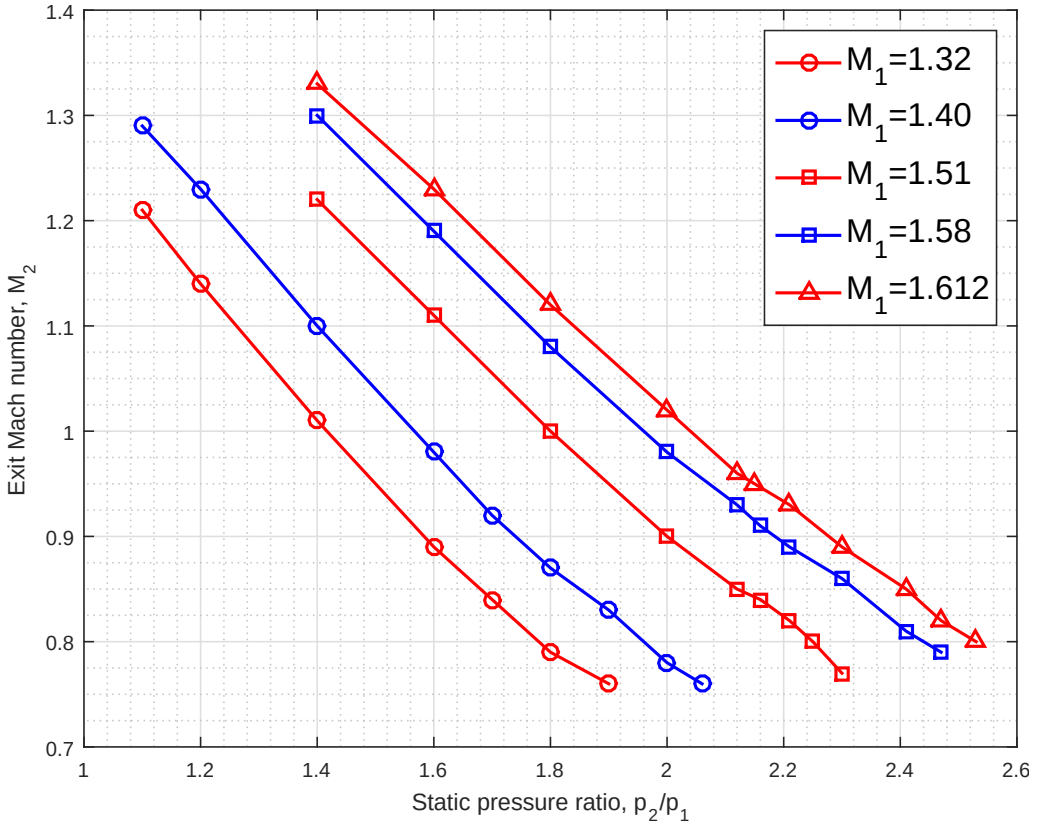

Figure 6.13: Influence of static pressure ratio on exit Mach number

6.4.2 Exit flow angle and flow turning

The variations in exit flow angle with static pressure ratio are reported in Figure 6.14.

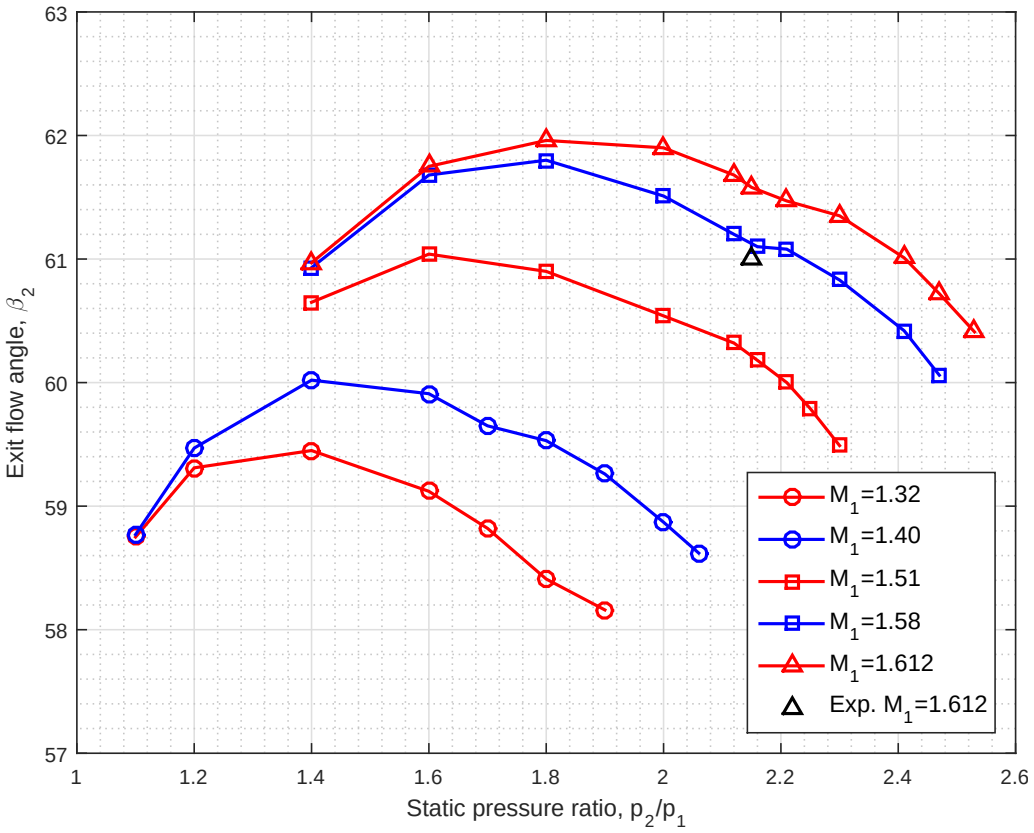

Figure 6.14: Influence of static pressure ratio on exit flow angle

As it can be seen, the trend of the CFD results depicted in Figure 6.14 substantially reflects the semi-empirical overall behaviour for an AVDR equal to unity reported in [28]. For example, increasing the static pressure ratio from low values (1.4) to high values (2.5), for a fixed inlet Mach number (1.612), corresponds to an increasing and then a decreasing of the mean exit flow angle, with a net change almost null. For different inlet Mach numbers, that is lower than the design inlet Mach number, increasing the static pressure ratio determines a similar behaviour of the mean exit flow angle. The maximum flow turning has been calculated to be at most of 2° and this fact is experimentally confirmed. The maximum mean exit flow angle is reached at near-sonic exit condition, that is when the exit Mach number downstream of the cascade is near unity. This fact is confirmed in [17], even if for flat-plate cascades. The reason behind the difference between measured and calculated exit flow angles at the design operating condition has already been discussed and it is related to mesh quality. Another interesting observation can be done looking at the contours of the Mach number resulting from the increasing in static

pressure ratio. It can be seen that from low to moderate static pressure ratios, the wake at the trailing edge is thin and almost symmetrical; at high pressure ratios the wake is asymmetrical and relatively thick, sign of a significant boundary layer separation on the suction side. The variation of the wake width from low to high static pressure ratio is reported in Figure 6.15 (static pressure ratio is increased from top to bottom).

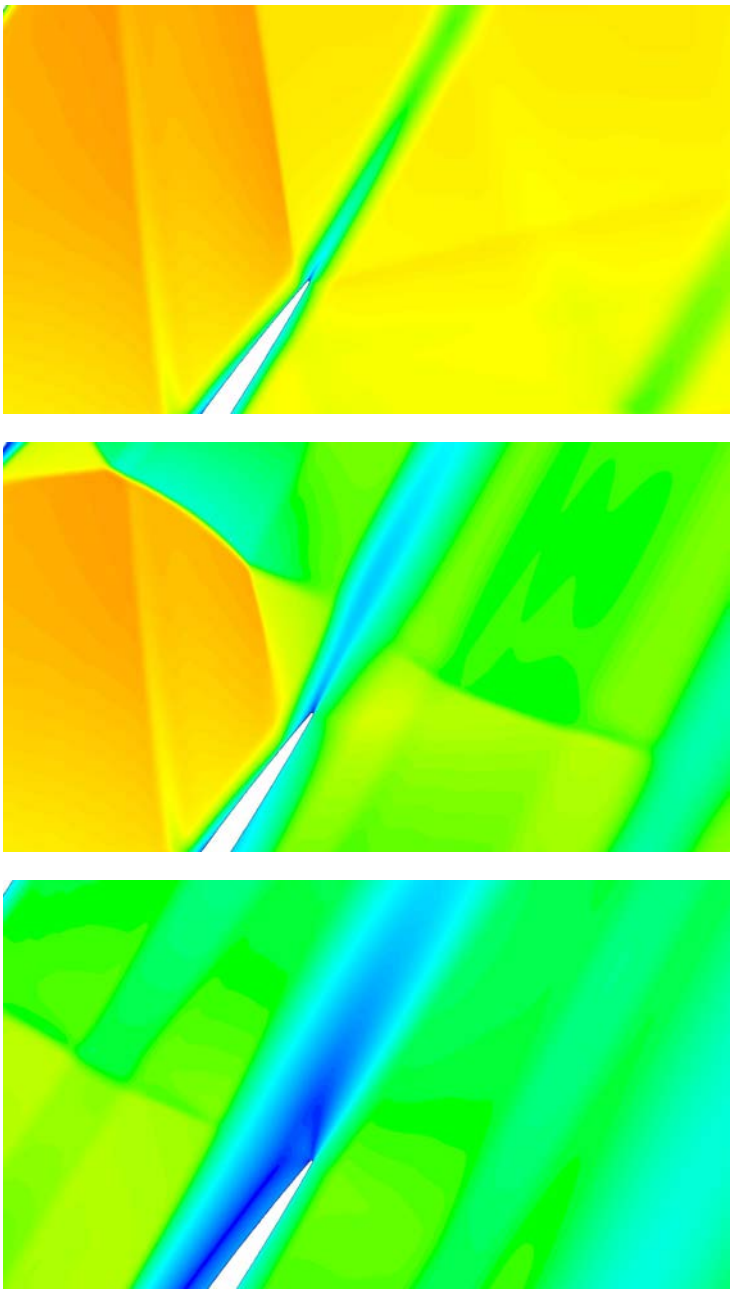

Figure 6.15: Variations of wake width with static pressure ratio

6.4.3 Total-pressure loss coefficient

The total-pressure loss coefficient curves are plotted in Figure 6.16.

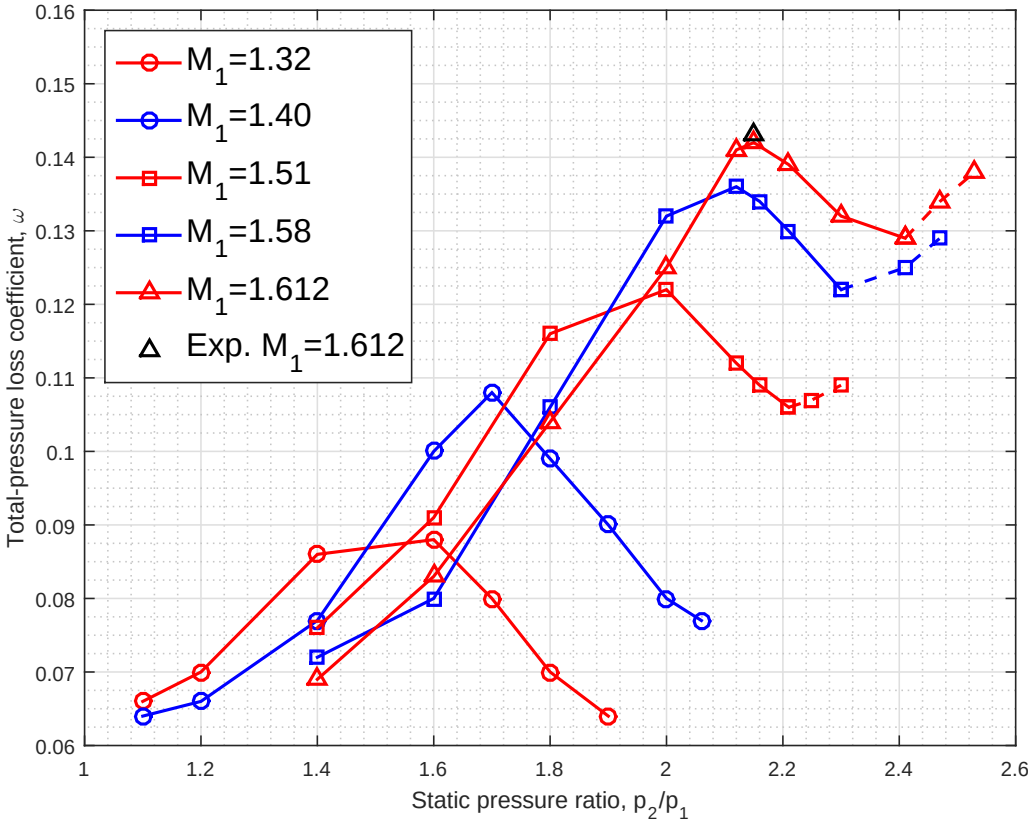

Figure 6.16: Influence of static pressure ratio on total-pressure loss coefficient

Generally speaking, taking a look at Figure 6.16, some considerations about the total-pressure loss coefficient can be made varying inlet Mach number for a fixed static pressure ratio or, on the other hand, varying static pressure ratio at fixed inlet conditions.

For a fixed static pressure ratio, increasing inlet Mach number corresponds to an increase of the total-pressure loss coefficient. This fact is quite obvious, since increasing inlet Mach number, that is flow speed, corresponds to an increase in strength of the shock waves. As a consequence, shock losses and viscous losses increase, since the boundary-layer separation on the suction side is stronger. Thus, the total-pressure loss coefficient increases.

For a fixed inlet Mach number, increasing static pressure ratio from low to moderate values causes an increase in total-pressure loss. It has been found that the total-pressure loss coefficient is maximum when a normal shock wave is situated near the exit of the cascade passage. This statement is experimentally confirmed in [28]. On the other hand, keeping the inlet conditions fixed and varying the static pressure ratio from moderate

to high values, leads to a reduction of the total-pressure loss coefficient. The general behaviour is that increasing the static backpressure from moderate to high values determines a reduction in shock losses, but, on the other hand, causes an increase in viscous losses due to the strong suction side boundary layer separation. In fact, the lambda shock patterns, which are produced by the interaction between the shock waves and the boundary layer, lead to a reduction of shock losses, but determine a corresponding increase in viscous losses. In fact, the lambda-shock systems rising in the passage determine a reduction in strength of the shock waves within the passage, but cause a considerable thickening of the boundary layer. The minimum total-pressure loss point is achieved just before the cascade spill point condition occurs. This fact has been experimentally demonstrated in [24], even if for a MCA profile cascade at slightly supersonic/transonic inlet Mach numbers, that is for an operating condition characterized by weaker shock wave-boundary layer interaction. However it is necessary to make a distinction. For relatively low inlet Mach numbers, that is for 1.32 and 1.40, the downward trend of the total-pressure loss coefficient with increasing static pressure ratio is kept until the maximum cascade static pressure ratio is reached. On the other hand, for higher inlet Mach numbers (1.51, 1.58, and 1.612), the total-pressure loss coefficient reaches its minimum at a certain value of the static pressure ratio and then it raises again. This trend could be due to three main reasons:

- the influence of AVDR on total-pressure loss coefficient. The increasing of viscous loss due to the strong boundary layer separation on the suction side can be mitigated only by increasing the AVDR, as has been experimentally demonstrated in [28]. In fact, an increase in AVDR reduces shock losses and viscous losses related to the shock wave-boundary layer interaction on both the pressure side and the suction side. In addition, wake width is considerably reduced when AVDR is increased and this corresponds to a reduction of overall losses, a reduction of the mean exit flow angle, and an increase in the flow turning. Since in a real supersonic compressor cascade, periodic or not, increasing the static backpressure corresponds to an increase in AVDR, and an increase in AVDR leads to a reduction of viscous loss, the total-pressure loss coefficient decreases if the static pressure ratio is increased to higher values than the design one. Moreover, the loss reduction due to the increasing of the AVDR is more pronounced at higher static pressure ratios, as has been demonstrated in [28] for the present cascade and in [13] for a similar one. Since all the simulations were carried out with a unity AVDR, the overall behaviour of the total-pressure loss coefficient is affected only by the static pressure ratio and not by the influence of the AVDR. Hence, the trend of the total-pressure loss coefficient beyond the minimum

point may be not completely realistic (for that reason it has been depicted with dashed lines). In order to better reproduce the cascade behaviour, it would be necessary to consider the influence of the AVDR, which cannot be reproduced in a two-dimensional simulation;

- the reaching of the limits for the turbulence model applicability, due to the large boundary layer separation and the high level of shock wave-boundary layer interaction, which can lead to an overestimation of the viscous loss and, as a consequence, of the total-pressure loss;

- the fact that the cascade maximum static pressure ratio results slightly overestimated, so the cascade is operating at static pressure ratios beyond the spill point, even if the unique incidence condition is still valid. For that reason, the operating conditions beyond the experimental maximum static pressure ratio could not have any physical meaning.

An important observation can be made comparing the semi-empirical curves for the total-pressure loss coefficient reported in Figure 6.12 with the curves resulting from the parametric study reported in Figure 6.16. It can be easily noted that the numerical trend does not correspond to the semi-empirical one. This is simply due to the fact that the semi-empirical trend of the total-pressure loss coefficient has been determined manipulating the experimental data in order to separate the influence of AVDR from that of the static pressure ratio. Since the experimental data have been mathematically manipulated by applying the conservation equations, some aspects have been neglected. In fact, as stated in [28], the semi-empirical loss-coefficient curves have not been determined using measured loss data, but following an indirect approach. On the other hand, the curves resulting from the CFD analysis have been determined calculating the total-pressure loss coefficient directly from the resulting values of total pressure upstream and downstream of the cascade. Moreover, the total-pressure loss coefficient, since the AVDR is unity in a 2D simulation, is affected only by the variation of the static pressure ratio. In summary, the overall trend of the total-pressure loss coefficient taking into account only the influence of the static pressure ratio could be summarized as follows: increasing the static pressure ratio from low to moderate values corresponds to an increase in the total-pressure loss coefficient; the point of maximum total-pressure loss corresponds to the condition in which a normal shock wave is located at the blade passage exit; increasing then the static pressure ratio from moderate to high values determines an overall reduction in total-pressure loss until a mimimum total-pressure loss point is achieved. The unique incidence is valid for all the operating conditions below the maximum achievable static pressure ratio.

Table 6.5: Cascade parameters variations with static pressure ratio ($M_1 = 1.32$)

$M_1 = 1.32$			
Static pressure ratio	**Exit flow angle**	**Exit Mach number**	**Total-pressure loss coefficient**
p_2/p_1	β_2	M_2	ω
1.1	58.8	1.21	0.066
1.2	59.3	1.14	0.070
1.4	59.5	1.01	0.086
1.6	59.1	0.89	0.088
1.7	58.8	0.84	0.080
1.8	58.4	0.79	0.070
1.9	58.2	0.76	0.064

Table 6.6: Cascade parameters variations with static pressure ratio ($M_1 = 1.40$)

$M_1 = 1.40$			
Static pressure ratio	**Exit flow angle**	**Exit Mach number**	**Total-pressure loss coefficient**
p_2/p_1	β_2	M_2	ω
1.1	58.8	1.29	0.064
1.2	59.5	1.23	0.066
1.4	60.0	1.10	0.077
1.6	59.9	0.98	0.100
1.7	59.7	0.92	0.108
1.8	59.5	0.87	0.099
1.9	59.3	0.83	0.090
2.0	58.9	0.78	0.080
2.06	58.6	0.76	0.077

Table 6.7: Cascade parameters variations with static pressure ratio ($M_1 = 1.51$)

$M_1 = 1.51$			
Static pressure ratio	**Exit flow angle**	**Exit Mach number**	**Total-pressure loss coefficient**
p_2/p_1	β_2	M_2	ω
1.4	60.7	1.22	0.076
1.6	61.0	1.11	0.091
1.8	60.9	1.00	0.116
2.0	60.5	0.90	0.122
2.12	60.3	0.85	0.113
2.16	60.2	0.84	0.109
2.21	60.0	0.82	0.106
2.25	59.8	0.80	0.107
2.31	59.5	0.77	0.109

Table 6.8: Cascade parameters variations with static pressure ratio ($M_1 = 1.58$)

$M_1 = 1.58$			
Static pressure ratio	**Exit flow angle**	**Exit Mach number**	**Total-pressure loss coefficient**
p_2/p_1	β_2	M_2	ω
1.4	60.9	1.30	0.072
1.6	61.7	1.19	0.080
1.8	61.8	1.08	0.106
2.0	61.5	0.98	0.132
2.12	61.2	0.93	0.136
2.16	61.1	0.91	0.134
2.21	61.0	0.89	0.130
2.30	60.8	0.86	0.122
2.41	60.4	0.81	0.125
2.47	60.1	0.79	0.129

Table 6.9: Cascade parameters variations with static pressure ratio ($M_1 = 1.612$)

$M_1 = 1.612$			
Static pressure ratio	**Exit flow angle**	**Exit Mach number**	**Total-pressure loss coefficient**
p_2/p_1	β_2	M_2	ω
1.4	61.0	1.33	0.069
1.6	61.8	1.23	0.083
1.8	62.0	1.12	0.104
2.0	61.9	1.02	0.125
2.12	61.7	0.96	0.141
2.15	61.6	0.95	0.142
2.21	61.5	0.93	0.139
2.30	61.4	0.89	0.132
2.41	61.0	0.85	0.129
2.47	60.7	0.82	0.134
2.53	60.4	0.80	0.138

6.4.4 Shock wave pattern and flow field

As previously stated, static pressure ratio affects not only the performance of a cascade, but also the shock wave pattern and the flow field within the blade passage. In Figure 6.17, Figure 6.18, and Figure 6.19 a sketch of the shock wave pattern is reported for an inlet Mach number of 1.32 and for the design inlet Mach number. The static pressure ratio is increased from low, to moderate, and then to high values, that is the static pressure ratio varies from values below to values above the design static pressure ratio. Taking a look at the wave pattern for different static pressure ratios at a fixed inlet condition, it can be noted how deeply the increase in static pressure ratio affects the flow field through a supersonic compressor cascade. As it can be seen, the shock wave pattern also varies according to the value of the inlet Mach number.

At low static pressure ratios, an oblique shock system develops from the trailing-edge of the profiles and spreads into the downstream region. The oblique shock waves at the trailing-edge are reflected on the pressure side of the adjacent blade and give rise to a complex interaction with the wake. The reflection of the shock-wave on the pressure side can produce a weak boundary-layer separation with reattachment.

Increasing the static backpressure from low to moderate values moves the shock at the trailing-edge forward into the blade passage. The shock wave located at the trailing-edge becomes gradually a normal shock wave, forming a lambda-shock structure at the suction side. For lower inlet Mach numbers, the lambda shock near the trailing edge of the airfoil is conspicuously smaller. The resulting shock wave-boundary layer interaction on the suction side causes a boundary-layer separation. In this operating condition, the flow field inside the cascade passage is characterized by a first passage shock near the entrance of the cascade passage and a second passage shock close to passage exit, with one or more reflected shocks. At design inlet conditions, this wave pattern is kept until the design static pressure ratio is achieved.

At high static pressure ratios, the oblique shock located at the passage entrance becomes a quasi-normal shock forming a lambda-shock with a related boundary-layer separation, while the second passage shock moves forward in the blade passage. The second passage shock, as it moves inside the passage, reduces its strength until it almost disappears. The width of the wake has considerably increased, affecting all the covered passage and the rearmost portion of the suction side, causing a shrinking of the passage area and an increase in viscous loss. For lower values of inlet Mach number, since the shock wave-boundary layer interaction is weaker, the boundary layer separation on the suction side is smaller and the wake is visibly thinner.

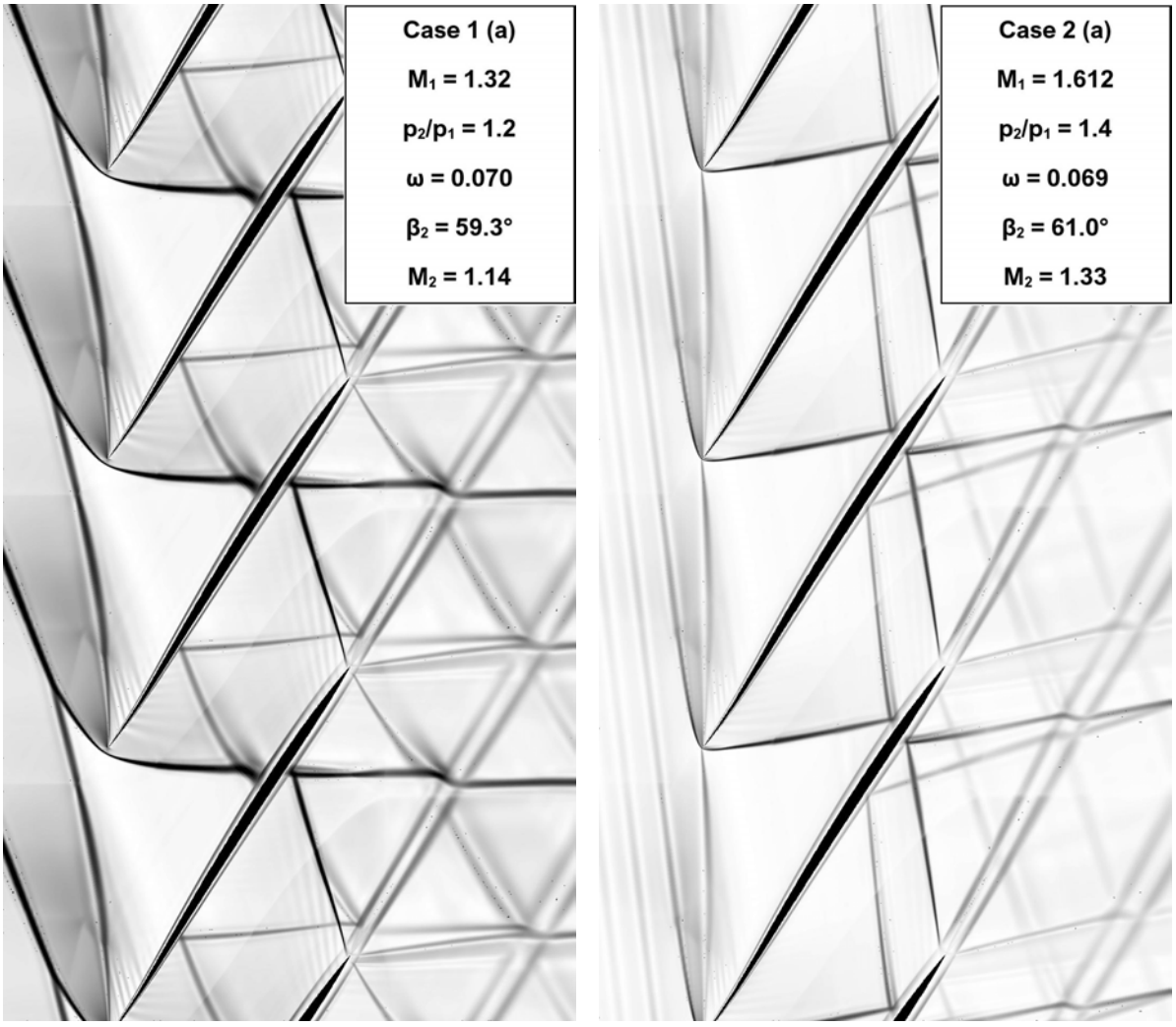

Figure 6.17: Numerical Schlieren pictures at low static pressure ratios for two values of inlet Mach number

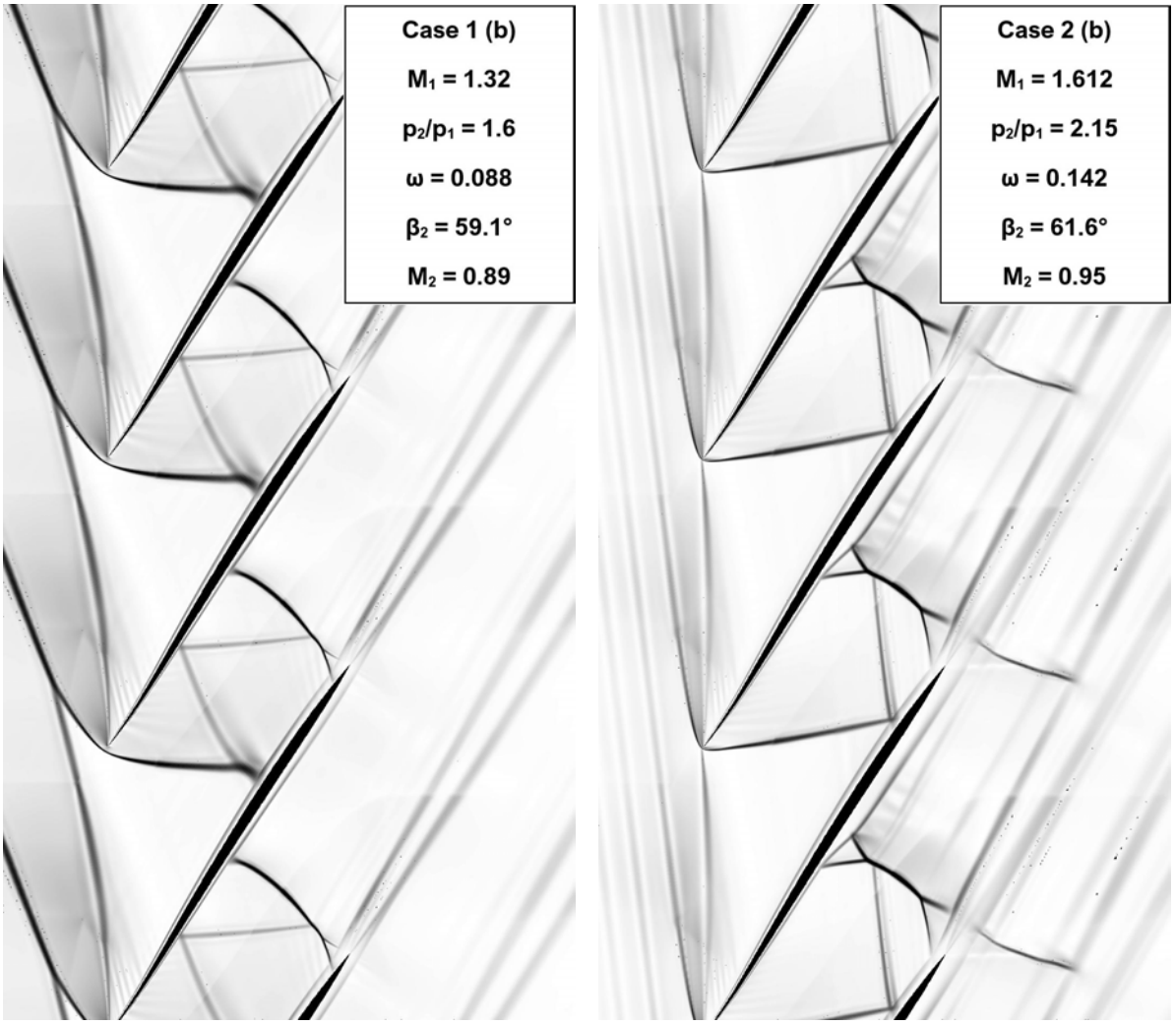

Figure 6.18: Numerical Schlieren pictures at moderate static pressure ratios for two values of inlet Mach number

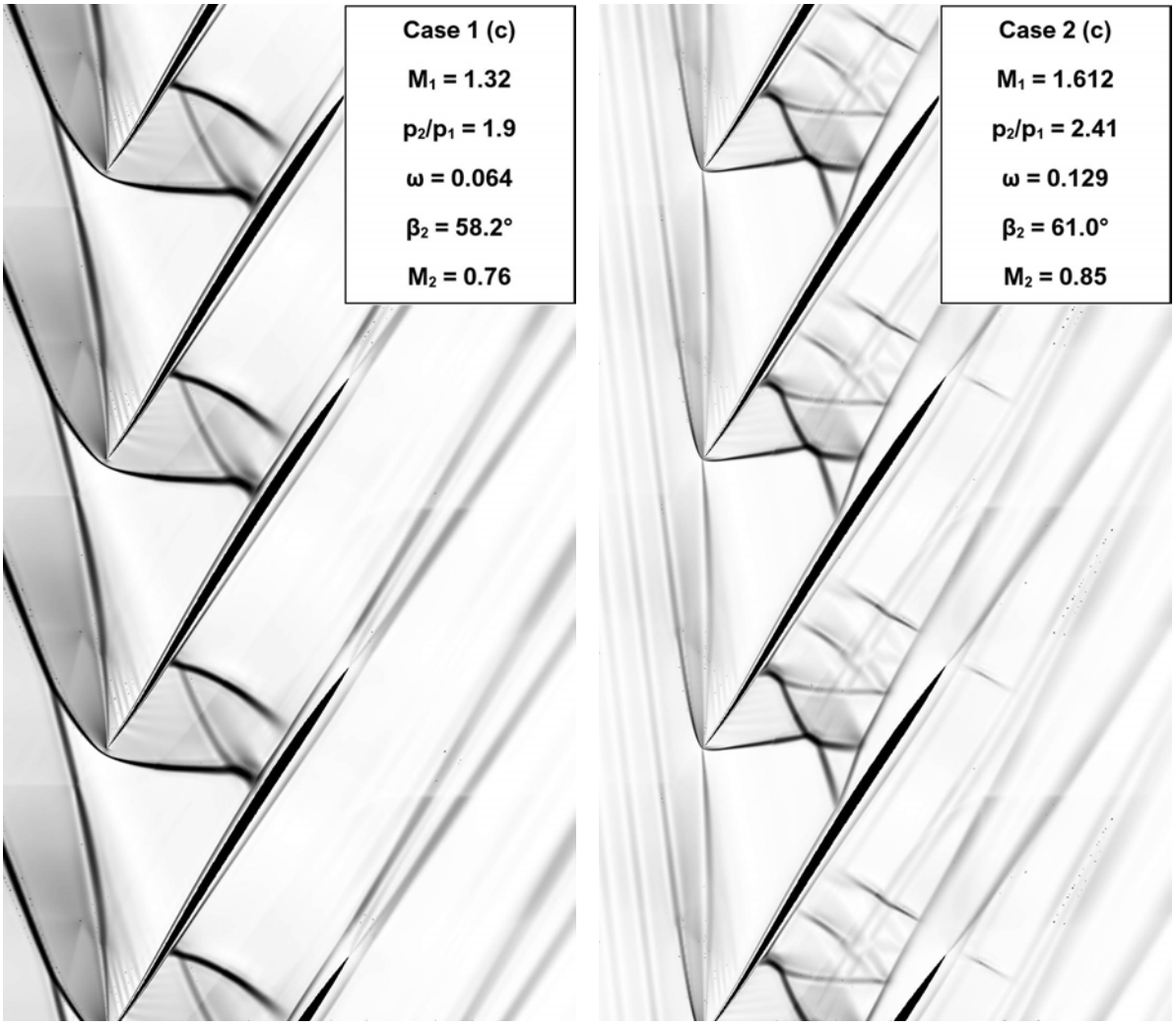

Figure 6.19: Numerical Schlieren pictures at high static pressure ratios for two values of inlet Mach number

The point of minimum total-pressure loss is reached when the first passage shock has become a quasi-normal shock located near the leading-edge. At the operating condition with minimum total-pressure loss, the shock at the passage entrance is still attached. On the other hand, the maximum total-pressure loss coefficient is obtained when a normal shock wave is located near the passage exit. For example, in Figure 6.20 a sketch of the shock wave pattern for the condition in which the total-pressure loss is maximum is reported. It refers to an operating condition with a nominal inlet Mach number of 1.58 and a static pressure ratio of 2.12, which corresponds to the point of maximum total-pressure loss.

Figure 6.20: Example of the shock wave pattern at maximum total-pressure loss point

6.5 Influence of cascade solidity

As stated before, cascade solidity deeply affects the overall performance of a supersonic compressor cascade. In fact, changing the solidity determines a modification of the passage width and, as a consequence, of the shock wave pattern inside the blade passage.
In order to analyze the influence of cascade solidity on the overall performance of the cascade, five cascades with different values of solidity were constructed. The variation in solidity has been performed varying the pitch and mantaining the blade chord (85 mm). Thus, it has been necessary to slightly modified the mesh for each analyzed value of cascade solidity. Table 6.10 summarizes the cascade solidity values employed in the simulations and the corresponding values of the cascade pitch.

Table 6.10: Investigated range of cascade solidity

Solidity	**Pitch**
σ	s $[mm]$
1.47	57.82
1.50	56.67
1.5294	55.58
1.56	54.49
1.60	53.125

As can be seen, for a fixed value of the blade chord, increasing the cascade solidity corresponds to a decrease of the cascade pitch. Moreover, increasing the cascade solidity corresponds to an increase of the length of the covered passage, since adjacent blades are closer to each other. The range of variation of the solidity is not too large, since in supersonic cascades small changes in geometry can produce great variations in the shock pattern, leading to unexpected results. The variation in cascade solidity from the baseline value of 1.5294 is around 5%, while the overall variation from the lower value (1.47) to the higher value (1.60) is approximately 9%.

The influence of the cascade solidity was carried out by examining some values of static pressure ratio in the range between the maximum and minimum total loss point, for an inlet Mach number equal to 1.612, that is the design inlet Mach number. The baseline cascade has a solidity equal to 1.5294, as previously specified. The calculated total-pressure loss coefficient for each value of cascade solidity and static pressure ratio is reported in Table 6.11, 6.12, and 6.13.

Table 6.11: Influence of solidity on total-pressure loss coefficient ($p_2/p_1 = 2.15$)

$p_2/p_1 = 2.15$	
Solidity	**Total-pressure loss coefficient**
σ	ω
1.47	0.142
1.50	0.143
1.5294	0.142
1.56	0.141
1.60	0.140

Table 6.12: Influence of solidity on total-pressure loss coefficient ($p_2/p_1 = 2.30$)

$p_2/p_1 = 2.30$	
Solidity	**Total-pressure loss coefficient**
σ	ω
1.47	0.133
1.50	0.132
1.5294	0.1316
1.56	0.131
1.60	0.132

Table 6.13: Influence of solidity on total-pressure loss coefficient ($p_2/p_1 = 2.40$)

$p_2/p_1 = 2.40$	
Solidity	**Total-pressure loss coefficient**
σ	ω
1.47	0.132
1.50	0.131
1.5294	0.129
1.56	0.127
1.60	0.125

These results demonstrate that increasing cascade solidity corresponds to a reduction of the total-pressure loss coefficient and, as a consequence, an increase in cascade efficiency. By comparing the total-pressure loss coefficient calculated at the design static pressure ratio and at the minimum loss static pressure ratio, for the maximum and the minimum values of cascade solidity considered, the decrease in total-pressure loss is around 2% and 5%, respectively. For that reason, it can be concluded that increasing the solidity of the cascade results in a reduction of the total-pressure loss. However, supersonic compressor cascades are quite susceptible to changes in solidity and, for that reason, solidity cannot be modified above certain limits. The influence of cascade solidity on the total-pressure loss coefficient for a fixed static pressure ratio is reported in Figure 6.21. Conversely, the influence of static pressure ratio on the total-pressure loss coefficient for a fixed value of the solidity is reported in Figure 6.22.

As regards the other exit flow variables, that is mean exit flow angle, exit Mach number, and inlet flow angle, which is a dependent variables related to the inlet Mach number by the unique incidence, changes in solidity did not provide significant variations.

As stated before, even small variations in cascade solidity can provide great change in the shock wave pattern and in the flow field within the blade passage. In fact, increasing or decreasing the cascade solidity of about 5% from the baseline value corresponds to a deep modification of the shock wave layout inside the passage. The Figures in the following pages compare the shock wave patterns obtained with a solidity equal to 1.47, 1.5294, and 1.60, respectively. The static pressure ratio is increased from left to right. As we can see, increasing the cascade solidity determines a lengthening of the blade covered passage and an increment of the number of shock waves within the passage. Consequently, the flow passing through each shock wave is slower, the strenght of the shock waves is reduced, and then the shock loss decreases, determining a reduction in total-pressure loss. Even if the behaviour of the flow passing throughout a supersonic cascade may not be easily understood, this simple consideration could explain the total-pressure loss coefficient trend resulting from the simulations. However, the increased number of shocks inside the passage determines a stronger interaction with the boundary layer, which tends to become thicker as the cascade passage becomes narrower, because of the increase in solidity. It may also be seen that, when cascade solidity is increased, the oblique shock reflected on the suction side of the adjacent blade does not impinge anymore on the quasi-normal portion of the second passage shock, but on the pressure side of the blade by which it is generated, creating a more complex interaction with the boundary layer on the blade surface.

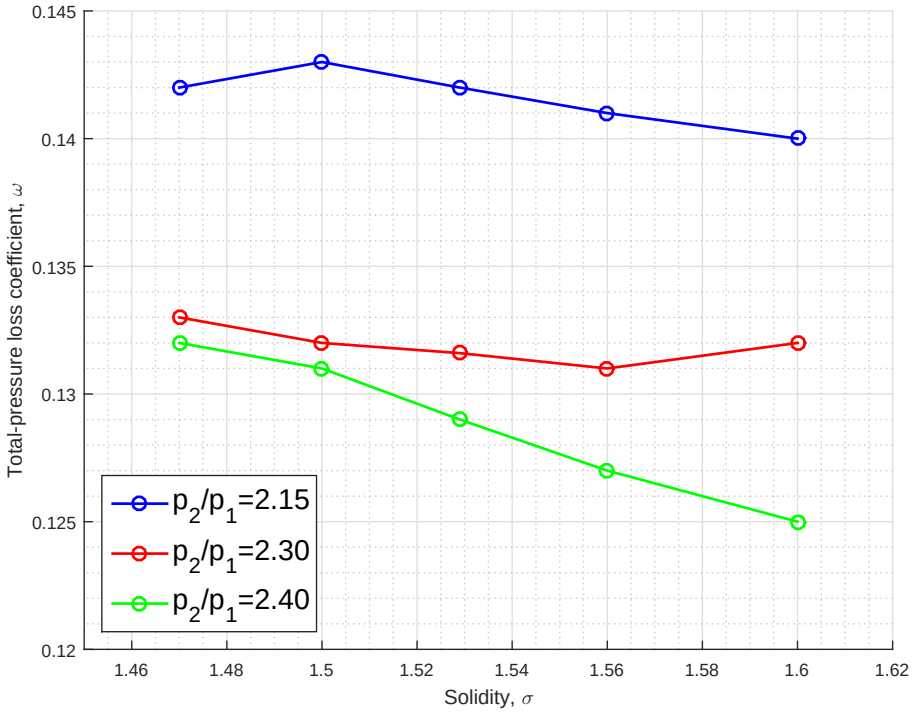

Figure 6.21: Influence of cascade solidity on total-pressure loss coefficient for a fixed static pressure ratio

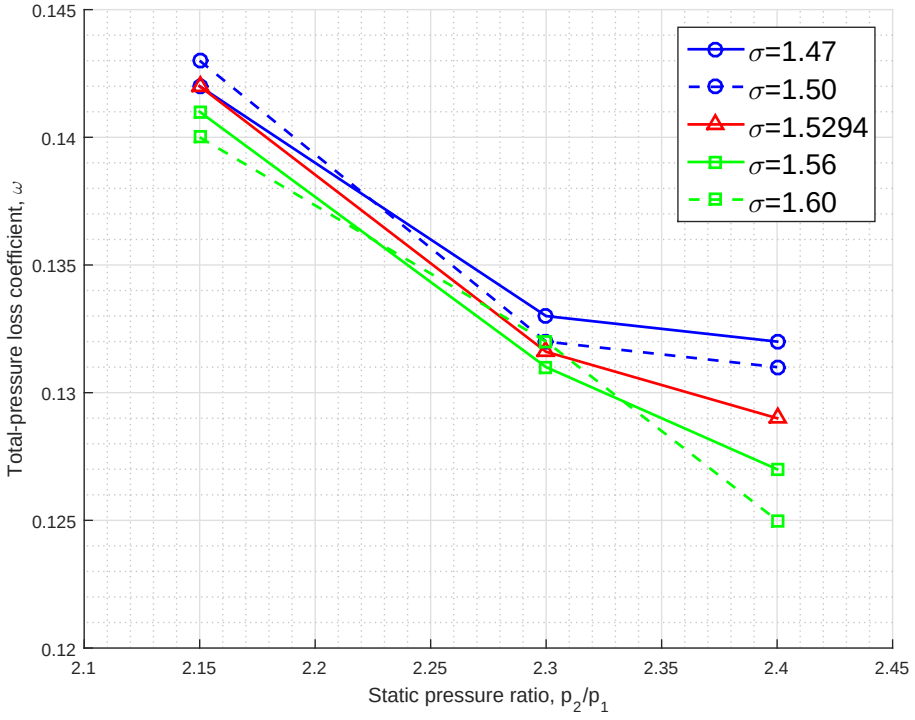

Figure 6.22: Influence of static pressure ratio on total-pressure loss coefficient for a fixed value of solidity

Figure 6.23: Numerical Schlieren pictures of the cascade flow field at different static pressure ratios for $\sigma = 1.47$

Figure 6.24: Numerical Schlieren pictures of the cascade flow field at different static pressure ratios for $\sigma = 1.5294$

Figure 6.25: Numerical Schlieren pictures of the cascade flow field at different static pressure ratios for $\sigma = 1.60$

Moreover, taking a look at the magnitude of the density gradient and at the Mach number contours at the leading-edge for a cascade solidity equal to 1.47 and 1.60, it can be noticed that the pre-compression shock intersects the bow shock of the adjacent blade on the suction side and on the blade leading-edge, respectively. Reasonably, a further increase in solidity makes the pre-compression shock to intersect the bow shock of the adjacent blade on the pressure side. The condition in which the pre-compression shock intersects the bow shock of the adjacent blade at the leading-edge corresponds to the maximum efficiency operating condition. If the intersection point is on the pressure side, the flow upstream of the cascade is not influenced by the pre-compression shock; conversely when the intersection point is on the suction side, the pre-compression shock influences the flow in the upstream region of the cascade.

Figure 6.26: Numerical Schlieren pictures of the leading-edge for $\sigma = 1.47$ and $\sigma = 1.60$

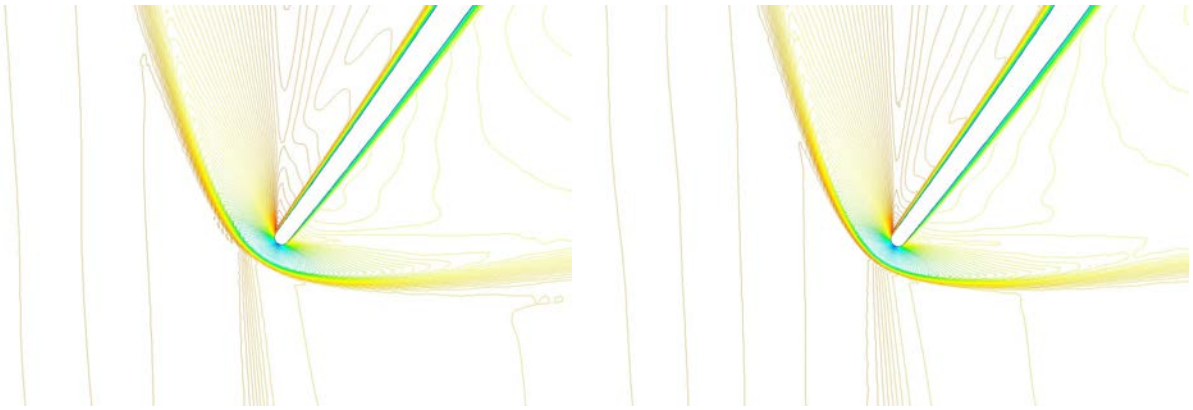

Figure 6.27: Mach number contours for $\sigma = 1.47$ and $\sigma = 1.60$

Conclusions

The thesis provided a detailed study of the two-dimensional flow in a linear supersonic compressor cascade. After a preliminary mesh validation study, a parametric analysis was carried out in oder to investigate the influence of the main flow and geometric quantities on the overall cascade performance, highlighting their effects on the main exit flow variables. The numerical results of the parametric study of the two-dimensional supersonic compressor cascade, known as ARL-SL19, have been presented and widely discussed. The cascade was tested over a quite wide range of inlet Mach numbers, static pressure ratios, and cascade solidity. The main results obtained from the validation and the parametric study, which was the focus of the present work, can be summarized as follows:

- the results obtained with the SA model showed the best agreement with the experimental data;
- the results concerning the numerical determination of the unique incidence for the cascade present good agreement with the experimental data and the analytical results;
- the design operating condition ($M_1 = 1.612$, $p_2/p_1 = 2.15$, AVDR= 1.00) is well reproduced by the numerical model. The calculated total-pressure loss coefficient was 0.142, with a corresponding flow turning of $-3.4°$, against measured values of 0.143 and $-3.4°$, respectively;
- a linear dependency of the maximum static pressure ratio achievable by the cascade on inlet Mach number was determined, over the range of inlet Mach numbers considered;
- increasing the static pressure ratio from low to moderate values corresponds to an increase in total-pressure loss, while increasing the static pressure ratio from moderate to high values corresponds to a reduction in total-pressure loss;
- it has been numerically confirmed that the maximum flow turning occurs at near-sonic exit conditions;

- a linear dependency of the exit Mach number on static pressure ratio was found;
- a moderate increase in cascade solidity corresponds to a reduction in total-pressure loss of around 2%-5% for static pressure ratios in the range between the design value and the static pressure ratio near the minimum loss point.

The CFD results have shown that the numerical solver ANSYS® Fluent provides a quite accurate solution of the two-dimensional supersonic flow through the ARL-SL19 supersonic compressor cascade and an excellent reproduction of the shock wave pattern in front and within the cascade passage. The overall performance data for different operating conditions are well predicted and in quite total agreement with the available experimental data. The results obtained from the parametric study in the present work may be of support to the preliminary design of a transonic/supersonic compressor cascade, the corresponding rotor blade section, or the stage of a supersonic compressor or fan, because they provide an accurate description of the influence of the main flow and geometric parameters on the performance, the exit flow variables, and the shock wave pattern in the cascade.

Future works and developments

Many other different aspects of the supersonic cascade treated in this thesis can be investigated in order to have a fuller and more developed analysis. As stated before, the present thesis has been mainly focused on the investigation of the main flow and geometric quantities, such as inlet Mach number, static pressure ratio, and solidity, on the overall cascade performance and on the shock wave pattern throughout the blade passage, whose knowledge is essential for the preliminary design of a supersonic compressor rotor. Even if the abovementioned quantities are the ones which deeper influence the behaviour and the performance of a supersonic cascade, additional variables can be considered for carrying out a parametric study as comprehensive as possible. For that reason, the Reynolds number Re, the maximum thickness t of the blade section, the leading-edge radius r_{LE}, and the stagger angle β_s can be investigated in a parametric study, highlighting their influence on the cascade performance, on the cascade mean exit flow variables, and on the cascade inlet flow variables. For example, varying the Reynolds number can slightly affect the value of the unique incidence inlet flow angle, while a modification of the leading edge radius can affect the precompression shocks. 3D simulations can be carried out in order to investigate the influence of the AVDR on the cascade. Moreover, a single-objective or a multi-objective design optimisation can be carried out on the S-shape airfoil of the cascade,

with a following parametric study aimed at finding the more efficient blade shape. Lastly, since the airfoils for supersonic turbomachines are very thin structures introduced into a high speed flow, they can be characterized by the dangerous aeroelastic phenomenon of flutter, which can seriously affect the integrity of the blade. For that reason, an aeroelastic analysis can be carried out, testing different sections and material properties.

Bibliography

[1] J. D. Anderson: *Fundamentals of Aerodynamics.* McGraw-Hill, New York, 5th edition, 2011.

[2] E. Benini: *Propulsione aerea.* CLEUP, Padua, 1st edition, 2005.

[3] W. J. Calvert and R. B. Ginder: *Transonic Fan and Compressor Design.* Proceedings of The Institution of Mechanical Engineers Part C - Journal of Mechanical Engineering Science, 213:419–436, 1999.

[4] A. Cavallini, M. Sovrano, S. Mancin, and L. Rossetto: *Elementi di gasdinamica.* Edizioni Progetto, Padua, 2012.

[5] N. A. Cumpsty: *Compressor Aerodynamics.* Longman Group, New York, 1984.

[6] S. Fleeter, R. L. Holtmann, R. B. McClure, and G. T. Sinnet: *Experimental Investigation of a Supersonic Compressor Cascade.* ARL TR 75-0208, 1975.

[7] ANSYS Fluent: *Fluent 15.0 Theory Guide.* ANSYS Inc., 2013.

[8] ANSYS Fluent: *Fluent 15.0 User's Guide.* ANSYS Inc., 2013.

[9] A. Fourmaux, R. Gaillard, G. Losfeld, and G. Meauzè: *Test Results on the ARL 19 Supersonic Blade Cascade.* ASME Journal of Turbomachinery, 110:450–455, 1988.

[10] G. R. Frost, R. M. Hearsey, and A. J. Wennerstrom: *A Computer Program for the Specification of Axial Compressor Airfoils.* 1972.

[11] G. Graziani: *Aerodinamica.* Università La Sapienza, Rome, 4th edition, 2016.

[12] W. M. Konig, D. K. Henneke, and L. Fottner: *Improved Blade Profile Loss and Deviation Angle Models for Advanced Transonic Compressor Bladings: Part II - A Model for Supersonic Flow.* ASME Journal of Turbomachinery, 117:81–87, 1996.

[13] B. Küsters and H. A. Schreiber: *Compressor Cascade Flow with Strong Shock-Wave/Boundary-Layer Interaction.* AIAA Journal, 36:2072–2078, 1998.

[14] B. Lakshminarayana: *Fluid Dynamics and Heat Transfer of Turbomachinery.* Wiley, New York, 1995.

[15] P. Levine: *The Two Dimensional Inflow Conditions for a Supersonic Compressor with Curved Blades.* ASNE Journal of Applied Mechanics, 24:165–169, 1957.

[16] H. J. Lichtfuss and H. Starken: *Supersonic Cascade Performance.* AGARD-LS-39, 1970.

[17] H. J. Lichtfuss and H. Starken: *Supersonic Cascade Flow.* Progress in Aerospace Sciences, 15:37–149, 1974.

[18] B. Liu, H. Shi, and X. Yu: *A New Method for Rapid Shock Loss Evaluation and Reduction for the Optimization Design of a Supersonic Compressor Cascade.* Journal of Aerospace Engineering, 2017.

[19] C. Osnaghi: *Teoria delle turbomacchine.* Società Editrice Esculapio, Bologna, 2nd edition, 2013.

[20] S. B. Pope: *Turbulent Flows.* Cambridge University Press, Cambridge, 2000.

[21] L. Quartapelle and F. Auteri: *Fluidodinamica incomprimibile.* Casa Editrice Ambrosiana, Milan, 2013.

[22] Biollo R. and E. Benini: *Recent Advances in Transonic Axial Compressor Aerodynamics.* Progress in Aerospace Sciences, 56:1–18, 2013.

[23] H. Schlichting and K. Gerstern: *Boundary-Layer Theory.* Springer, Berlin, 9th edition, 2017.

[24] H. A. Schreiber and H. Starken: *Experimental Cascade Analysis of a Transonic Compressor Rotor Blade Section.* Journal of Engineering for Gas Turbines and Power, 106:288–294, 1984.

[25] G. K. Serovy and T. H. Okiishi: *Performance of a Compressor Cascade Configuration with Supersonic Entrance Flow - A Review and Comparison of Experiments in Three Installations.* ASME Journal of Turbomachinery, 110:441–449, 1988.

[26] P. R. Spalart and S. R. Allmaras: *A One-equation Turbulence Model for Aerodynamic Flows.* AIAA, 439, 1992.

[27] H. Starken: *Untersuchung der Stromung in ebenen Uberschall-verzogerungs gittern (Investigation of the Flow in a Supersonic Plane Decelerated Cascade).* DLR FB,71–99, 1971.

[28] D. L. Tweedt, H. A. Schreiber, and H. Starken: *Experimental Investigation of the Performance of a Supersonic Compressor Cascade.* ASME Journal of Turbomachinery, 110:456–466, 1988.

[29] G. Venturelli: *Development of Numerical Procedures for Turbomachinery Optimization.* PhD dissertation, Università degli Studi di Padova, 2013.

[30] A. J. Wennerstrom: *The Design and Evaluation of a High-Through-Flow Transonic Axial Compressor.* 6th International Symposium on Air Breathing Engines, Paris.

[31] A. J. Wennerstrom and G. R. Frost: *Design of a 1500ft/sec Transonic High-Through-Flow Single-Stage Axial Compressor with Low Hub-Tip Ratio.* AFAPL-TR-76-59, 1976.

[32] F. M. White: *Fluid Mechanics.* McGraw-Hill, New York, 5th edition, 2002.

[33] R. E. York and H. S. Woodard: *Supersonic Compressor Cascades - An Analysis of the Entrance Region Flow Field Containing Detached Shock Waves.* ASME Journal of Engineering for Power, 98:247–257, 1976.